

## Wind-AE: A Fast, Open-source 1D Photoevaporation Code with Metal and Multi-frequency X-ray Capabilities

2 MADELYN I. BROOME ,<sup>1</sup> RUTH MURRAY-CLAY ,<sup>1</sup> JOHN H. McCANN,<sup>1</sup> AND JAMES E. OWEN ,<sup>2,3</sup>

3 <sup>1</sup>*University of California Santa Cruz, 1156 High Street, Santa Cruz, CA 95060, USA*

4 <sup>2</sup>*Imperial Astrophysics, Imperial College London, South Kensington Campus, London SW7 2AZ, UK*

5 <sup>3</sup>*Department of Earth, Planetary, and Space Sciences, University of California, Los Angeles, CA 90095, USA*

6 Submitted to APJ

### ABSTRACT

Throughout their lives, short period exoplanets (<100 days) experience X-ray and extreme-UV (XUV) stellar irradiation that can heat and photoionize planets' upper atmospheres, driving transonic outflows. This photoevaporative mass loss plays a role in both evolution and observed demographics; however, mass loss rates are not currently directly observable and can only be inferred from models. To that end, we present an open-source fast 1D, XUV multi-frequency, multispecies, steady-state, hydrodynamic Parker Wind photoevaporation relaxation model based on Murray-Clay et al. (2009). The model can move smoothly between high and low flux regimes and accepts custom multi-frequency stellar spectra. While the inclusion of high-energy X-rays increases mass loss rates ( $\dot{M}$ ), metals decrease  $\dot{M}$ , and the net result for a typical hot Jupiter is a similar  $\dot{M}$ , but a hotter, faster, and more gradually ionized wind. We find that multifrequency photons (e.g., 13.6-2000 eV) are absorbed over a broader range of heights in the atmosphere resulting in a wind-launch radius,  $R_{\text{XUV}}$ , that is of order 10 nanobars for all but the highest surface gravity planets. Grids of H/He solar metallicity atmospheres reveal that, for typical hot Jupiters like HD 209458b,  $R_{\text{XUV}} \approx 1.1 - 1.8 R_P$  for low-fluxes, meaning that the energy-limited mass loss rate,  $\dot{M}_{\text{Elim}}(R)$ , computed at  $R = R_P$  is a good approximation. However, for planets with low escape velocities, like many sub-Neptunes and super-Earths,  $R_{\text{XUV}} \approx 2 - 8 R_P$ , making it necessary to use  $\dot{M}_{\text{Elim}}(R = R_{\text{XUV}})$  to avoid significantly underestimating mass loss rates. For both high escape velocities and large incident fluxes, radiative cooling is significant and energy-limited mass loss overestimates  $\dot{M}$ .

Keywords: Planets and Satellites: Atmospheres — Planets and Satellites: Physical evolution — Planet-star interactions — X-rays: ISM

### 1. INTRODUCTION

Close-in planets are highly irradiated by X-ray (> 100 eV) and extreme UV (EUV, in this paper 13.6-100 eV) photons from their host stars. These high energy photons can ionize atoms in a planet's upper atmosphere (above the planet's optical transit radius) and heat the layer in the atmosphere where they are absorbed. This heating creates a pressure gradient which drives an outflow known as a Parker wind.

mabroome@ucsc.edu

These outflows are observable in transit (for a review, see Dos Santos et al. 2023), but observational limitations make it difficult to directly map observations to mass loss rates (Schreyer et al. 2024). It is, therefore, necessary to model atmospheric escape in order to predict mass loss rates. Constraining mass loss rates not only allows for the prediction of observables, but is important in tracing the mass loss histories of exoplanets and understanding their present-day demographics (e.g., Lee & Connors 2021; Rogers et al. 2021; Kubyshkina & Fossati 2022; Poppenhaeger et al. 2021; Rogers et al. 2024).

49 However, most currently available models are time-  
 50 dependent hydrodynamic codes, which are run for many  
 51 sound-crossing times to reach a steady-state solution, at  
 52 which point the mass-loss rates can be measured. This  
 53 approach requires pre-computing large grids of mass-loss  
 54 rates, which can then be interpolated onto evolutionary  
 55 models (e.g., Owen & Jackson 2012; Kubyshkina & Fos-  
 56 sati 2021; Rogers et al. 2021). As model sophistication  
 57 grows, so does the number of parameters required for  
 58 any grid, meaning that it is not computationally fea-  
 59 sible to use these time-dependent approaches to fully  
 60 map out the parameter space before they are coupled  
 61 to any evolutionary calculation. Alternatively, relax-  
 62 ation methods which directly solve for the steady state  
 63 are much more computationally efficient (Murray-Clay  
 64 et al. 2009), so much so that they can be directly cou-  
 65 pled to an evolutionary calculation dynamically allowing  
 66 more parameters to be included and, in principle, more  
 67 complete physics in the mass loss model. In this paper,  
 68 we present a relaxation code with a more complete de-  
 69 scription of the physics of atmospheric escape than was  
 70 included in Murray-Clay et al. (2009).

71 We take particular care to model the X-ray physics  
 72 and metal-X-ray interactions as many exoplanets likely  
 73 have super-solar atmospheric metallicities (Thorngren  
 74 et al. 2016; Kempton et al. 2023; Kirk et al. 2025) and  
 75 the presence of metals in the upper atmosphere can al-  
 76 low X-rays to contribute significantly to the heating and  
 77 ionizing of the wind (García Muñoz 2007). This is the  
 78 result of two properties of X-rays: (1) X-ray photons  
 79 are energetic enough that they can induce collisional  
 80 secondary ionizations via the high-energy photoelectron  
 81 released when the X-ray photon ionizes a species and  
 82 (2) X-ray photons are energetic enough to ionize the K-  
 83 shell (innermost) electron of certain metals common to  
 84 exoplanet atmospheres (e.g., C, N, O, Ne, Mg, Si, and  
 85 S), giving these metals a larger photoionization cross-  
 86 sections at high energies relative to those of the more  
 87 abundant H and He and allowing X-rays to be absorbed  
 88 higher in the atmosphere where they can contribute to  
 89 driving the wind.

90 Treating these X-ray properties allows us to model  
 91 smoothly across the high and low stellar XUV flux  
 92 regimes without changing any of the assumptions in our  
 93 model. The outflow is energy-limited and is predom-  
 94 inantly driven by EUV photons in the low XUV flux  
 95 limit (e.g., García Muñoz 2007; Lammer et al. 2014;  
 96 Erkaev et al. 2016; Owen & Alvarez 2016). In the high  
 97 XUV flux limit, the contribution of the X-rays is more  
 98 significant, and the outflow and ionization is balanced  
 99 by recombination at the base, leading this regime to be  
 100 referred to as recombination-limited (Owen & Jackson

101 2012; Cecchi-Pestellini et al. 2006; Caldrioli et al. 2022).  
 102 Since the ratio of the XUV to bolometric luminosity  
 103 decreases more than three orders of magnitude over a  
 104 star’s lifetime (e.g., Jackson et al. 2012; King & Wheat-  
 105 ley 2021a; Affolter et al. 2023) and the ratio of EUV to  
 106 X-ray luminosity also varies (e.g., Chadney et al. 2015;  
 107 King & Wheatley 2021b), being able to model smoothly  
 108 between the high and low flux regimes will allow our  
 109 model to be used to model the evolution of mass loss  
 110 rates over Gigayear timescales.

111 While mass loss has been observed around both low  
 112 (e.g., Vidal-Madjar et al. 2003; Ehrenreich et al. 2015;  
 113 Zhang et al. 2023) and high (e.g., Fossati et al. 2013a;  
 114 Lecavelier Des Etangs et al. 2010; Edwards et al. 2023)  
 115 XUV flux stars, observations do not provide model-  
 116 independent mass loss rates. For example, for typi-  
 117 cal systems, Lyman- $\alpha$  (e.g., Vidal-Madjar et al. 2003;  
 118 Ehrenreich et al. 2015) Doppler broadening cannot be  
 119 used to directly infer mass loss rates because ISM ab-  
 120 sorption and geocoronal emission obfuscate the Lyman-  
 121  $\alpha$  line-center, making it impossible to extract the out-  
 122 flow velocity below the sonic point (Owen 2019). Helium  
 123 10830Å transits (e.g., Spake et al. 2018; Nortmann et al.  
 124 2018) are similarly limited by the need for full non-LTE  
 125 models of metastable helium to back mass loss rates out  
 126 of the He 10830Å transits (Spake et al. 2018; Allan &  
 127 Vidotto 2019; Linssen & Oklopčić 2023; Biassoni et al.  
 128 2024). Metal absorption lines may be more direct prox-  
 129 ies of the mass loss rate (e.g., Fossati et al. 2013b; Yan  
 130 et al. 2022; Huang et al. 2023; Linssen et al. 2024), but  
 131 inferring the observability of these lines still requires a  
 132 model that predicts the velocity and ionization fraction  
 133 of metals in an outflow (e.g., Linssen et al. 2024).

134 For these reasons, a photoionization-driven atmo-  
 135 spheric escape model that includes X-ray physics and  
 136 metals is a necessary tool for predicting mass loss rates.  
 137 A variety of valuable 1D models for photoionization-  
 138 driven escape exist and are explored in more detail  
 139 in Appendix A (e.g., Yelle 2004; Tian et al. 2005;  
 140 García Muñoz 2007; Owen & Wu 2017; Dos Santos et al.  
 141 2022; Caldrioli et al. 2022; Malsky & Rogers 2020; Kosk-  
 142 inen et al. 2022; Spinelli et al. 2023; Huang et al. 2023;  
 143 Schulik & Booth 2023; Kubyshkina et al. 2024). Nev-  
 144 ertheless, the ability to quickly forward-model the mass  
 145 loss rates and outflow structures of multispecies plane-  
 146 tary atmospheres irradiated by both high and low flux  
 147 multi-frequency XUV stellar spectra is valuable for pa-  
 148 rameter studies (this paper, Loyd et al. 2025), predict-  
 149 ing observables (Pai Asnodkar et al. 2024), and modeling  
 150 evolution.

To that end, we present `Wind-AE`<sup>1</sup>. `Wind-AE` is a fast 1D, steady-state, forward model for a photoionization-driven transonic Parker Wind based on the relaxation model from Murray-Clay et al. (2009), with XUV multi-frequency and multispecies capabilities and self-consistent modeling of the upper atmosphere below the wind.

This open-source code is based in C with a Python wrapper that ramps smoothly between solutions that span the range of planetary parameter space (mass, radius, semi-major axis), stellar spectral parameter space (stellar mass and radius, XUV flux, bolometric luminosity, spectrum) and metallicity space (metals, ionization states, and metallicity). The relaxation method reliably finds a solution to two-point boundary value problems, but is very sensitive to the proximity of the initial guess to the goal solution in parameter space. The parameter space ramping algorithm allows us to negotiate this sensitivity by stepping strategically through parameter space in order to reach the goal solution. We have the ability to specify metals present, as well as metallicities, but do not include diffusion or drag—an appropriate assumption for metals whose masses are below the crossover mass, which holds for all models in this paper (see Schulik & Booth 2023, for a model with full diffusion capabilities). Nevertheless, `Wind-AE` fills a niche not only with its speed, but with the inclusion of metals and full X-ray ionization physics, as well as the ability to customize stellar spectra and model both the high- and low-flux limit.

In Section 2 we give an overview of the methods we use to model multispecies and multi-frequency outflows. We then explore the impact of these additions on the outflow structure and mass loss rate of HD 209458b, a Neptune-like planet, and a mini-Neptune in Section 3. Finally, in Section 4 we produce high and low flux mass loss grids and discuss the parameter-space limitations of our model in Section 5.

Additionally, in Appendix A we benchmark `Wind-AE` against existing 1D models for HD 209458b and GJ 1214b in the low EUV/XUV flux limit (García Muñoz 2007; Salz et al. 2016; Dos Santos et al. 2022; Caldirola et al. 2022; Kubyshkina et al. 2024) and for a  $1M_J$ ,  $1.7R_J$  planet and WASP 121b in the high XUV flux limit (Owen & Jackson 2012; Huang et al. 2023).

## 2. METHODS

We have built upon the 1D relaxation code presented in Murray-Clay et al. (2009) by adding multi-frequency and multispecies capabilities and updating the lower

boundary approach. In §2.2 we introduce our model assumptions when solving the mass, momentum, and energy conservation and ionization balance equations which are given in their generic species- and frequency-independent forms in §2.1. Heating and cooling terms are described in §2.3. The physical and numerical impact of adding multi-frequency and multispecies capabilities are explored in §2.4 with a more detailed discussion of our spectrum smoothing algorithm (§2.4.1) and the X-ray physics (§2.4.2) which motivate the multi-frequency and multispecies versions of the ionization equation and the photoionization heating rate in the energy equation (§2.4.3).

### 2.1. Species- and Frequency-independent Hydrodynamic Steady-state Parker Wind Equations

We use finite difference equations and *Numerical Recipes*'s relaxation method solver `solvde` (Press et al. 1992) to solve the substellar 1D spherically-symmetric steady-state mass, momentum, energy, and ionization balance equations between upper and lower boundary points (Fig. 1). Given the critical point, the “sonic point” ( $R_{\text{sp}}$ ), in the Parker wind transonic solution, the outflow structure becomes a two-point boundary problem, with the upper boundary being  $R_{\text{sp}}$  and the lower boundary ( $R_{\text{min}}$ , typically  $\sim$ microbar; see Figure 1) being a point lower in the atmosphere than the wind launch radius.

Relaxation is an efficient method for solving two-point boundary value problems (Murray-Clay et al. 2009) and it is sufficient to model just the relaxation region,  $R_{\text{XUV}} < r < R_{\text{sp}}$ , in order to calculate mass loss rates. This is because the wind becomes much more optically thin past the sonic point and goes supersonic—losing causal contact with the gas below it—therefore, the photons absorbed past the sonic point do not contribute to the heating and mass loss rate of the planet. We define “wind launch radius” ( $R_{\text{XUV}}$ , a.k.a., photoionization base or ionization front) to be the lowest radial extent of substantial photoionization energy deposition (see Appendix B for more details). It is, therefore, also the radius where the monoatomic gas starts to accelerate, driven by the pressure gradient generated by ionization heating. Since our model is 1D and flow lines are assumed to be radial, the flow structure is only valid out to the Coriolis turning radius,  $R_{\text{cori}}$ . We estimate  $R_{\text{cori}}$  as the radius where the outflow velocity, integrated starting at the sonic point and ignoring pressure acceleration, is deflected by one radian due to the Coriolis force. Past  $R_{\text{cori}}$ , the velocity of the wind is predominantly set by the gravity of the star and secondarily by

<sup>1</sup> Pronounced, “windy”. Stands for Wind Atmospheric Escape.

interactions with the stellar wind (Schreyer et al. 2024), and our method will underestimate the density of the outflow. See Appendix B for more detail on boundary conditions.

Our 1D slice of a planet's atmosphere is the substellar point where tidal gravity and stellar flux are strongest, so, extrapolating the mass loss rate at that location to the rest of the planet's surface would overestimate the total mass loss. Thus, for the results in the main body of this paper, we multiply  $\dot{M}$  by a generic reduction factor of 0.3 that encodes adjustments for spherical geometry and horizontal heat redistribution (Murray-Clay et al. 2009). The equation for surface-averaged mass loss rate then becomes  $\dot{M} = 0.3 \cdot 4\pi R_{\text{sp}}^2 \rho(R_{\text{sp}}) v(R_{\text{sp}})$ , in agreement with 3D model results and similar to approaches where the incident flux is divided by 4.

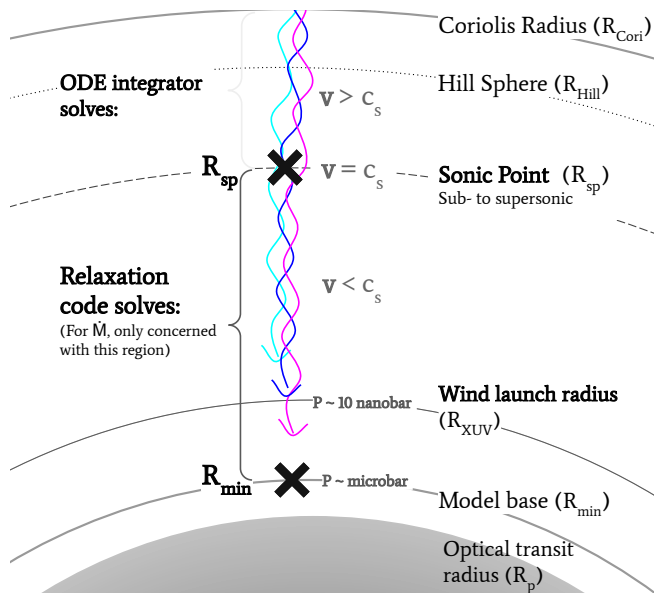


**Figure 1. Diagram of wind structure** - A thermally-driven, Parker-wind-like outflow is driven by photoionization heating, primarily deposited near the wind launch radius ( $R(\tau_{\text{XUV}}) = 1$ ). Our relaxation code solves for the structure of this outflow by integrating between two boundary conditions, the minimum radius of the simulation ( $R_{\text{min}}$ ) and the sonic point ( $R_{\text{sp}}$ ), identified by large black 'x's. Shorter wavelengths of incident stellar irradiation, like x-rays, are represented by the magenta wave and penetrate deeper into the atmosphere than the longer wavelength dark purple (higher-energy EUV) and cyan (lower-energy EUV). Magnitude of the local velocity,  $v$ , relative to the local sound speed,  $c_s$ , is given in the middle column. Important planetary radii in the wind's structure are identified in text in the righthand column (grey semicircle,  $R_p$ ; heavy solid,  $R_{\text{min}}$ ; light solid,  $R_{\text{XUV}}$ ; dashed,  $R_{\text{sp}}$ ; dotted,  $R_{\text{Hill}}$ ; heavy solid,  $R_{\text{Cori}}$ ).

Mass continuity is given by

$$\frac{\partial}{\partial r}(r^2 \rho v) = 0, \quad (1)$$

where the gas density is  $\rho$ , gas velocity is  $v$ , and distance from the planet's center is  $r$ . This equation takes on no species or frequency dependence because we do not model drag, but rather assume a constant mass fraction for each species throughout the wind. Here, species refers to each unique element, including all of the ionization states of that element. We, therefore, assume that the species are co-moving in the outflow, so share the same velocity. Momentum conservation in a frame rotating with the planet's orbital frequency is

$$\rho v \frac{\partial v}{\partial r} = -\frac{\partial P}{\partial r} - \rho \nabla \phi. \quad (2)$$

For the gravitational potential including stellar tides,  $\phi$ , we use the full form of

$$\phi = -\frac{GM_p}{r} - \frac{GM_*}{r_*} - \frac{1}{2}\Omega^2 r_\perp^2, \quad (3)$$

where, for the substellar point,  $r_* = a - r$  and  $r_\perp = a(\frac{M_*}{M_* + M_p})^{1/2} - r$ , where  $a$  is the semimajor axis and  $r$  radius from the planet's center. Here,  $G$  is the gravitational constant,  $P$  is the gas pressure,  $\Omega$  is the rotation rate of a frame centered on the center of mass of the star-planet system (i.e., the planet's orbital frequency), and  $M_p$  and  $M_*$  are the planet and stellar mass, respectively. Our tidal gravity term incorporates the transition to Roche lobe overflow, but our code is not designed to model Roche lobe overflow.

In its generic form, energy conservation is,

$$\rho v \frac{\partial}{\partial r} \left[ \frac{kT}{\mu(\gamma - 1)} \right] = \frac{kTv}{\mu} \frac{\partial \rho}{\partial r} + \Gamma + \Lambda. \quad (4)$$

The left-hand side represents the change in the internal thermal energy of the fluid, where  $k$  is the Boltzmann constant,  $\gamma = 5/3$  for a monatomic ideal gas, and  $\mu$  is the mean molecular/atomic weight which changes self-consistently as a function of radius as the ionization fraction changes. On the right-hand side, the first term tracks  $PdV$  cooling (work due to adiabatic expansion of the gas). The heating rate per volume,  $\Gamma$ , is due to radiative heating by bolometric stellar photons absorbed below the wind and to photoionization heating by XUV photons absorbed within the wind. Photoionization calculations now include primary and secondary ionizations and thus gain a dependence on species and frequency (§2.4.3). The cooling rate per volume,  $\Lambda$ , now contains not only Lyman- $\alpha$  cooling as in Murray-Clay et al. (2009), but also atomic metal line cooling (Appendix F) inside of the wind and radiative bolometric

cooling below the wind. The multispecies and multi-frequency versions of these equations and the relevant assumptions are discussed in §2.3.

Since much of the energy budget of the wind is set by photoionization, it is also necessary to solve for the ionization balance in the wind which is, generically,

$$318 \quad \mathcal{I} = \mathcal{R} - \mathcal{A}. \quad (5)$$

The photoionization rate,  $\mathcal{I}$  is balanced by the two right-hand terms, which are the radiative recombination rate  $\mathcal{R}$  (for which we adopt the uncoupled on-the-spot approximation, meaning that we do not consider the possibility that the resulting photons ionize other species (Friedrich et al. 2012)) and the rate at which ions are advected away,  $\mathcal{A}$ . Murray-Clay et al. (2009) showed that collisional ionization is negligible for a pure-H hot Jupiter atmosphere and we find the same for all planets modeled in this paper. This generic form is expanded into the species and frequency dependent form in §2.4.3.

Using the finite difference species-dependent forms of these four equations (Appendix Eq. D12—D14), we are able to use the relaxation method to solve for the structure of a hydrodynamic steady-state Parker wind up to the sonic point:

- 355 1. total mass density,  $\rho(r)$  (see Eq. (D11))
- 356 2. temperature,  $T(r)$  (see Eq. D13)
- 357 3. velocity,  $v(r)$  (see Eq. D12)
- 358 4. per-species neutral fraction,  $\Psi_s(r)$  (see Eq. D14)
- 359 5. per-species column density,  $N_{\text{col},s}(r)$  (see Eq. D15)

We track  $N_{\text{col}}$  since the neutral fraction is calculated separately for each species. Thus, we need to track the column density of individual species in order to compute the optical depth to photoionizing radiation,  $\tau$  (Friedrich et al. 2012).

To navigate the sensitivity of the relaxation method, we have created ramping algorithms that take a series of smaller, adaptive steps in parameter space and converge boundary conditions as needed. This allows us to smoothly ramp between solutions that may be too far apart in parameter space to converge to in a single jump.

Our boundary conditions are the temperature, mass density, and per-species neutral fraction at  $R_{\min}$  and the per-species column density at  $R_{\text{sp}}$ . While we have the ability to set these BCs explicitly, unless otherwise indicated, in this paper, we post-facto compute per-species column density self consistently from the density between the sonic point and Coriolis radius and

pre-compute the lower boundary conditions by assuming that the energy budget between the optical transit radius,  $R_P$ , and the wind-launch radius,  $R_{\text{XUV}}$ , (where  $R_P < R_{\min} < R_{\text{XUV}}$ ) is dominated by a balance of bolometric heating and cooling and that the temperature structure is isothermal. For detailed derivations of the mass density, temperature, and radius of the base of the simulation, see Appendix B. Note that if the sonic point is outside of the exobase of the planet, the transonic Parker wind solution is not valid and a flag is raised in our model. These planets would not be undergoing mass-loss hydrodynamically and would switch to thermal mass-loss via Jeans escape.

The ionization fraction, velocity and temperature information at  $r > R_{\text{sp}}$  can be of interest when inferring the observability or coupling to other atmospheric escape models, so we also included the ability to integrate the solution outward beyond the sonic point to the Coriolis radius, using Numerical Recipes' `odeint` and the Bulirsch-Stoer (`bsstep`) adaptive stepsize ODE integrator (Press et al. 1992) with tolerance  $10^{-13}$ .

Integrating outward to the self-consistently computed Coriolis radius, self-consistently converging the column density at the sonic point, and computing the lower boundary density, radius, and temperature, as well as adjusting the molecular-to-atomic-wind transition radius (§2.3) constitute the process we call “polishing”.

## 386 2.2. Model Assumptions

When computing the ionization balance we include photoionization (including secondary ionization from collisions with photoelectrons), advection, and recombination. Since we are primarily concerned with the wind’s launch, we do not model charge exchange as it has a secondary effect on the net ionization where the wind is launching and requires a more expensive photochemical model (e.g., García Muñoz 2007; Huang et al. 2023). We also do not model drag or diffusion as these require expensive time-dependent multifluid models (Schulik & Booth 2023). Diffusion of atomic species within the wind should be negligible for species below the cross-over mass (Hunten et al. 1987) as postfacto calculations have confirmed all atomic species in this paper are. If the mass of a species is greater than the crossover mass, its upwards diffusion rate is slower than those of the lighter species and it will diffuse throughout the wind and experience drag. Species with masses less than the crossover mass, on the other hand, can be considered entrained in the outflowing gas. This is assumed for all species (neutral and ionized) in the models presented here. Thus, those elements present at the lower boundary of our model (typically 1  $\mu\text{bar}$ ) will maintain the

same relative abundance throughout the whole upper atmosphere, though their ionization states will change.

We do not model the lower atmosphere in detail, so do not treat diffusion or lofting of species into the upper atmosphere. However, `Wind-AE` users can approximate this behavior by choosing to include only species in the simulations that they expect will be lofted to the lower boundary pressure. To provide an appropriate estimate for the pressure as a function of radius, we approximate the region below the wind as isothermal and molecular. However, because the lower boundary conditions of our model include temperature, species abundance, and species ionization fraction, as well as the ability to specify the presence and radial extent of the molecular-isothermal layer, this model can be easily coupled to more sophisticated photochemical lower atmosphere models.

When computing heating and cooling we include photoionization heating, PdV, Lyman- $\alpha$ , OI, OII, OIII, CII, CIII, and recombination cooling. These terms represent the first-order heating and cooling sources for the planets in the parameter space we present here. Our model is fully customizable and other metals and ionization states can be added by users to explore the role of different coolants in the future. We do not model conductive, free-free/bremsstrahlung, or collisional cooling, but compute them post-facto to confirm their irrelevance to the cases we present here. For the puffy planets with low escape velocities and for planets in the high stellar XUV flux limit, conduction and free-free cooling can be a significant energy term; so, we reserve the implementation of free-free and conductive heating and cooling for future updates of `Wind-AE` and present in this paper only planets for which conduction is not significant ( $< 1\%$  of the energy budget).

### 2.3. Heating & Cooling Terms

Below the photoionization base, the atmosphere is molecular and the temperature structure can be approximated by an isotherm at the skin temperature (Guillot 2010). Often, this region is treated as having a constant isothermal base temperature inferred from equilibrium temperature models (which is an oversimplification; Parmentier & Guillot 2014; Parmentier et al. 2015) or estimates for similar planets and this temperature is used as a lower boundary condition at some radius higher than  $R_P$ . More sophisticated and expensive models (e.g., Huang et al. 2023) perform full lower atmosphere photochemistry calculations to obtain more physical and accurate temperature and density structure and we compare to such models in Appendix A.

We elect for an approximation somewhere between the

two approaches. We directly compute the skin temperature (Appendix Eq. B1) as the balance between bolometric heating and cooling and use the assumption of an isotherm and a constant mean molecular weight to compute the microbar radius as our simulation base given a measured optical transit radius (see Appendix B). Because we do not treat molecules or photochemistry in our model, we set a constant mean molecular weight,<sup>2</sup>  $\mu_{\text{mol}}(r)$ , for all points below the wind and force  $\mu$  to transition to the numerically-solved mean atomic weight,  $\mu(r)$ . We do so smoothly, by multiplying  $\mu_{\text{mol}}$  by a complementary error function (Eq. B6) that drops off as the wind becomes optically thin (Appendix Fig. 19), the molecules photodissociate, and ionization heating begins to dominate, launching the wind. As a result, we can write  $\mu(r)$  for all  $r$  in the simulation as

$$\mu(r) = \mu_{\text{mol}}(r)\text{erfc}(r) + \mu_{\text{atom}}(r)[1 - \text{erfc}(r)] \quad (6)$$

$$= 2.3m_H\text{erfc}(r) + \frac{m_H \cdot [1 - \text{erfc}(r)]}{\sum_s Z_s \frac{m_H}{m_s} (2 - \Psi_s(r))}, \quad (7)$$

where the mean molecular weight of the species explicitly modeled in our outflow,  $\mu_{\text{atom}}(r)$ , includes electrons, ions, and neutral atoms and hence changes as a function of radius as the gas ionization state evolves. As we currently do not model multiple ionization states per atom, we can simplify the traditional definition of  $\mu_{\text{atom}}(r)$  to be in terms of  $\Psi_s$ , the “neutral” fraction (fraction of the species in the lowest ionization state). Here,  $m_H$  is the atomic mass of hydrogen,  $m_s$  is the atomic mass of species  $s$  in the wind, and  $Z_s$  is the mass fraction of that species. The complementary error function is discussed in more detail in Appendix B.

We use the same error function to force the optical ( $\kappa_{\text{opt}} = 0.004$ ) and IR opacities ( $\kappa_{\text{IR}} = 0.01$ ) (Guillot 2010) in the bolometric heating (Eq. 11) and cooling equations (Eq. 10) to drop off at the same transition point as the molecular-to-atomic transition (Appendix B). The result is that the bolometric heating and cooling that dominated below the wind give way to photoionization heating and atomic line cooling within the wind. This simplification does not affect hot Jupiters, but will likely be important for puffy sub-Neptunes (§5.1). Future work explicitly modeling the physics in this region is merited (for more on the impacts of lower atmosphere modeling, see, Appendix Figures 15 & 18)

Above the photoionization base ( $\sim 10$  nanobars), the wind is generally atomic and the energy budget (Eq. 4) is set by a balance of photoionization heating, ad-

<sup>2</sup> For the results shown in this work  $\mu_{\text{mol}} = 2.3m_H$  which is the mean molecular weight of H<sub>2</sub> and He in solar abundances.

507 vective heating, cooling due to  $PdV$  work (gas ex-  
 508 pansion), recombination cooling, Lyman- $\alpha$  cooling, and  
 509 metal line cooling. For the planets in this paper, as mod-  
 510 eled in other approaches (e.g., Kubyshkina et al. 2018a;  
 511 Caldiroli et al. 2022; Koskinen et al. 2022; Linssen et al.  
 512 2024; Huang et al. 2023), it is reasonable to assume that  
 513 this is optically-thin line cooling, but other regions of pa-  
 514 rameter space where this may not be an appropriate as-  
 515 sumption merit further investigation. Also, most likely,  
 516  $H_{3+}$  cooling (Yelle 2004; García Muñoz 2007) and other  
 517 molecules (Yoshida et al. 2022, 2024) also play a signif-  
 518 icant role in cooling in the molecular region below the  
 519 wind, absorbing and radiating away the highest energy  
 520 photons of the XUV irradiation.

521 The cooling term, however, is now  $\Lambda(r) = \Lambda_{Ly\alpha}(r) +$   
 522  $\Lambda_{\text{metal}}(r) + \Lambda_{\text{bolo}}(r)$ , where

$$\Lambda_{Ly\alpha}(r) = -7.5 \times 10^{-19} n_e n_{\text{HI}} e^{-11834K/T} \quad (8)$$

523 and  $n_e$  is the number density of total electrons,  $n_{\text{HI}}$  is  
 524 the number density of neutral H,  $T$  is temperature in  
 525 Kelvin, and all vary as a function of radius.  $\Lambda_{Ly\alpha}$  is  
 526 radiative cooling from the Lyman- $\alpha$  line of atomic hy-  
 527 drogen,  $\Lambda_{\text{metal}}$  is radiative cooling from metal lines, and  
 528  $\Lambda_{\text{bolo}}$  is bolometric cooling from thermal emission in the  
 529 molecular layer of the atmosphere, where we assume  
 530 that radiative cooling can be treated with an average  
 531 infrared opacity (Guillot 2010) rather than needing to  
 532 be modeled line by line. In Appendix C we verify that  
 533 a majority of the Ly $\alpha$  photons escape the wind.

534 In the atomic outflow, we have found OII, OIII, CII,  
 535 and CIII metal line cooling to be non-negligible at high  
 536 fluxes and Linssen et al. (2024) find Fe II and Ca II  
 537 line cooling significant in high metallicity cases (which  
 538 are not treated in this paper and thus these lines are  
 539 neglected for the time being). There is some debate  
 540 as to whether Mg is a net heater or coolant (Huang  
 541 et al. 2017; Fossati et al. 2013b), so here we choose to  
 542 initially work with O and C, and our model can handle  
 543 further line coolants to explore their role in the future.  
 544 Line cooling is generally most impactful at high fluxes.  
 545 However, even at low fluxes, some Lyman- $\alpha$  photons are  
 546 able to escape the outflow and cool the wind, making it  
 547 the second most significant contribution to the cooling  
 548 of the wind after  $PdV$  cooling.

549 We model metal line cooling using a two-level atom  
 550 model,

$$\Lambda_{\text{metal}}(r) = - \sum_s n_e n_{\text{ion},s} \left[ A_s \frac{\exp\left(-\frac{T_{\text{line},s}}{k_b T}\right)}{n_e \left(1 + \frac{n_{c,s}}{n_e}\right)} \right], \quad (9)$$

551 where  $n_{\text{ion},s}$  is the number density of OII, OIII, CII,  
 552 and/or CIII, and the constants are derived from Fer-  
 553 land et al. (2017) and CHIANTI (Dere et al. 1997; Del

554 Zanna et al. 2015). These constants are derived by fit-  
 555 ting this two-level atom model to the full cooling rates  
 556 calculated by CHIANTI in the temperature range 500-  
 557 20,000 K. We find this approach accurately models the  
 558 true cooling function to within an accuracy of a few per-  
 559 cent. The values of the species-dependent constants  $A_s$ ,  
 560  $T_{\text{line},s}$ , and  $n_{c,s}$  are listed in Appendix F.

561 The final cooling term is the bolometric cooling, which  
 562 is discussed in more detail in Appendix B:

$$\Lambda_{\text{bolo}}(r) = 2\sigma_{SB} T_{\text{skin}}^4 \rho(r) \kappa_{\text{IR}} \text{erfc}(r). \quad (10)$$

563 Here  $\sigma_{SB}$  is the Stefan-Boltzmann constant,  $T_{\text{skin}}$  is the  
 564 skin temperature which we take to be  $T(R_{\min})$ , and  $\kappa_{\text{IR}}$   
 565 is the IR opacity. In the atomic/ionized wind, line cool-  
 566 ing dominates; however, in the molecular region between  
 567  $R_{\min}$  and  $R_{\text{XUV}}$ , where it is optically thick to most XUV  
 568 photons and, in the low flux limit, the highest energy  
 569 X-ray photons are radiated away by molecular line cool-  
 570 ing, our assumption that bolometric cooling dominates  
 571 provides a reasonable approximation. If the photodisso-  
 572 ciation front extends beyond the wind launch radius and  
 573 molecules survive into the wind, transitioning at  $R_{\text{XUV}}$   
 574 as we do in this paper would no longer be appropri-  
 575 ate. We explore the limits of these assumptions in the  
 576 low escape velocity limit in §5.2, but for the majority of  
 577 planets in this investigation we can safely assume that  
 578 the molecules have photodissociated and/or thermally  
 579 dissociated below  $R_{\text{XUV}}$ . To approximate this behavior,  
 580 we multiply  $\kappa_{\text{IR}}$  and  $\kappa_{\text{opt}}$  (the optical opacity) by the  
 581 same complementary error function (Eq.B6) as is used  
 582 in Equation 6, which lowers these opacities to zero so  
 583 that the bolometric cooling does not unphysically dom-  
 584 inate in the atomic wind. This transition is visible at  
 585  $\sim 1.1 R_P$  in Figure 5.

586 The same is done for the bolometric heating term,

$$\Gamma_{\text{bolo}}(r) = F_* \rho(r) \left( \kappa_{\text{opt}} \text{erfc}(r) + \frac{1}{4} \kappa_{\text{IR}} \text{erfc}(r) \right), \quad (11)$$

587 where  $F_*$  is the single-band bolometric flux which is an  
 588 independent variable that is not dependent on the cho-  
 589 sen SED shape or integrated XUV flux ( $F_{\text{tot}}$ ). In this  
 590 double-grey approximation, the total heating then be-  
 591 comes  $\Gamma(r) = \Gamma_{\text{ion}}(r) + \Gamma_{\text{bolo}}(r)$ <sup>3</sup>. The photoionization  
 592 heating term that dominates in the wind,  $\Gamma_{\text{ion}}$ , is also  
 593 now species-dependent and also incorporates the con-  
 594 tribution to heating by highly energetic primary photo-  
 595 electrons released during the ionization of each initial  
 596 species by a high energy X-ray photon (Eq. 18). The  
 597 species and frequency dependent  $\Gamma_{\text{ion}}$  equation is dis-  
 598 cussed in detail in §2.4.

599 <sup>3</sup> Full derivation in Appendix B.

#### 2.4. Multi-frequency & Multispecies

The photoionization heating rate per unit volume,  $\Gamma_{\text{ion}}(r)$ , and ionization rate per unit volume,  $\mathcal{I}(r)$ , both contain a dependence on frequency  $\nu$  and species  $s$  in the form of the photoionization cross-section  $\sigma_s(\nu)$  and number of secondary ionization,  $\eta_s(\nu)$ . Broadly speaking, the photoionization cross-sections,  $\sigma_s(\nu)$ , for most species,  $s$ , are maximal at the species's ionization edge and decrease with increasing energy. Thus, the optimal depth  $\tau_s(\nu) = N_{\text{col},s}\sigma_s(\nu) = 1$  surfaces for a species like HI will occur deeper in the atmosphere for higher-frequency photons.

However, the picture is not always so simple. X-rays not only have the ability to ionize more than one species per photon (see §2.4.2 for a discussion of secondary ionizations), certain species, such as C, N, O, Ne, Mg, Si, and S experience a spike in  $\sigma_s$  at high energies (e.g., 120 eV for C). For these species, X-rays above that energy threshold can ionize the innermost, K-shell electron in the atom. The first five of these seven species are predicted to be among the most abundant species in exoplanet atmospheres (e.g., Kempton & Knutson 2024). Add to this the findings of Thorngren et al. (2016), which suggest that most exoplanets should have super-solar metallicities, and the interactions between X-rays and metals become essential to accurately modeling where photoionization heating begins to dominate and the wind launches. We reserve a full discussion of metals and high metallicity physics for a forthcoming paper.

The density and pressure at which the wind launches has a significant impact on mass loss rates and on the temperature and velocity of the wind, so accurate modeling of the photoionization base is one of the benefits of multi-frequency, multispecies modeling.

##### 2.4.1. Multi-frequency Spectrum

In order to capture the most important features of a multi-frequency spectrum, while simultaneously lowering computational cost, we implement multi-frequency EUV photons by modeling a smoothed solar spectrum with smoothing bin edges located at the ionization energies of species present in the wind. We employ a custom Savitzky-Golay binning and smoothing algorithm that requires that the smoothed spectrum's normalized flux to be accurate to the flux of the high resolution spectrum at ionization energies and the relevant K-shell ionization energies of each species included in a simulation (Fig. 2). A Savitzky-Golay method is of particular use for fitting polynomials to a spectrum because it locally conserves ionizing energy since the peaks of the

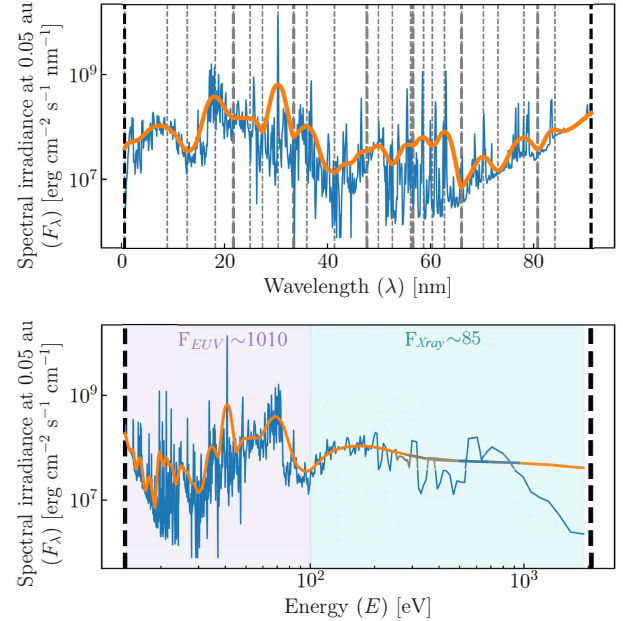


**Figure 2.** Savitzky-Golay smoothed and binned FISM2 solar spectrum scaled to 0.05 au - Flux at 0.05 au vs. wavelength in nm (top) and vs. energy in eV (bottom). The solid purple and cyan highlights correspond to the EUV (13.6-100eV) and X-ray ( $>100$ eV) portions of the spectrum, respectively, and the approximate fluxes of each portion are labeled at the top of the bottom plot in  $\text{ergs s}^{-1} \text{cm}^{-2}$ . Bin edges (heavy vertical dashed lines) are automatically set at ionization edges for species present in a given simulation for maximum accuracy in calculating ionization rates (here pure-H). Thin vertical dashed lines are the critical points in the smoothing (Appendix E). We crop our spectra in this investigation at 2000 eV because contributions from higher energies are negligible and most photons that high energy have  $\tau_\nu = 1$  surfaces below the base of the wind and do not contribute to driving the wind. The XUV smoothed spectrum for a pure-H planetary atmosphere (above) results in 59 wavelength bins and the EUV in 66.

spectrum are smoothed and distributed locally. See Appendix E for a complete discussion of this algorithm.

Since XUV stellar spectra are not available for many stars and instrumental observational limitations mean that many “full” stellar spectra are reconstructions, our default spectrum is a flux-scaled version of the FISM2 (Chamberlin et al. 2020) solar spectrum, though it is possible to implement unique stellar spectra in our model.

For all of the results presented in this paper we use a scaled solar spectrum. Many atmospheric escape models employ scaled solar spectra to simulate the spectra of stars of a similar type (e.g., García Muñoz 2007; Salz et al. 2015; Koskinen et al. 2022; Huang et al. 2023; Kubyshkina et al. 2024) and it has been shown that

the SED shape affects the upper atmosphere ionization structure and therefore the outflow structure (Guo & Ben-Jaffel 2016; Biassoni et al. 2024; Kubyshkina et al. 2024). We find the same when we benchmark against existing 1D models (Appendix A) and the difference can be especially significant for an M-dwarf (Loyd et al. 2025) vs. solar spectrum, as M-dwarfs have higher relative X-ray flux than FGK stars. We reserve an exploration of the impacts of a highly-XUV-active star for a forthcoming investigation of HD 189733b, but do explore the high XUV-flux recombination limit modeled by Owen & Jackson (2012) in Appendix A.

For the remainder of this paper, when we refer to flux, we will use the following designations:  $F_*$  is the total bolometric flux,  $F_{\text{tot}}$  is a generic total flux over any high-energy spectral range,  $F_{\text{XUV}}$  is the total flux over 13.6–2000 eV, and  $F_{\text{EUV}}$  is always the flux in the range 13.6–100 eV, all at the semi-major axis of the planet. These flux values may occasionally be normalized to different energy ranges and we will identify when we do so. For example, HD 209458’s EUV flux is typically quoted in the literature as 450 ergs s<sup>-1</sup> cm<sup>-2</sup>, which is the total flux over 13.6–40 eV (e.g., García Muñoz 2007; Murray-Clay et al. 2009; Koskinen et al. 2013; Salz et al. 2015). We use this value to normalize our scaled solar spectrum, which makes  $F_{\text{EUV}}=1010$  ergs s<sup>-1</sup> cm<sup>-2</sup> and  $F_{\text{XUV}}=1095$  ergs s<sup>-1</sup> cm<sup>-2</sup>.

#### 2.4.2. X-rays and Secondary Ionizations

In the case of a star with low XUV flux (typical of an older star), X-rays penetrate deeply into the atmosphere and are absorbed at  $\tau(\text{X-ray}) = 1$ . The  $\tau(\text{X-ray}) = 1$  surface is typically at pressures  $> 10^{-9}$  bar, a region which Yelle (2004), García Muñoz (2007), and Huang et al. (2023) indicate is dominated by molecules. When low-flux X-rays fall in this region, the majority of the energy the X-rays deposit is radiated away by molecular line cooling (Yelle 2004; García Muñoz 2007, e.g.). In that case, the wind is instead launched at  $\tau(\text{EUV}) = 1$ , which is higher in the potential well and at a lower density. These “low flux” winds, therefore, tend to be predominantly EUV driven.

In the case of a star with high XUV flux, the heat deposited by X-rays at  $\tau(\text{X-ray}) = 1$  is significant enough to contribute to the dissociation of those molecules into atoms. These atoms cannot cool as efficiently as molecules and, as a result, the heat deposited by X-rays is no longer radiated away. Thus, the  $\tau(\text{X-ray}) = 1$  layer—which is deeper in the potential well than the  $\tau(\text{EUV}) = 1$  surface and also denser—is able to reach the temperatures necessary to launch a wind. The result is a denser wind and a higher mass loss rate. Thus,

because young stars (<100 Myr old) are expected to have such high relative flux of ionizing XUV photons (e.g., Chadney et al. 2015; King & Wheatley 2020), X-rays are expected to be major contributors to the period of most photoevaporative significant mass loss for planets (e.g., Owen & Jackson 2012; Cecchi-Pestellini et al. 2006; Kubyshkina & Fossati 2022).

Properly modeling X-ray physics requires addressing the unique ionization properties of X-rays. First, in the low flux limit for typical planets, the ionization cross sections,  $\sigma(\nu)$ , for hydrogen and helium peak at their ionization energies (13.6 and 24.59 eV, respectively) and drop off with frequency. Thus, for an H-He atmosphere, the  $\tau(\nu) = 1$  surface where the X-rays are absorbed is too deep in the atmosphere to contribute to heating and driving the wind. This follows from the definition of  $\tau$ , where  $\tau(\nu) = \int_{\infty}^{\nu} (\sum_s n_{0,s} \sigma_s(\nu)) dl$  and  $n_{s,0}$  is the number density of the lowest ionization state of species,  $s$ , where  $s$  need not be a neutral atom in the case of our simulation. However, the decrease in  $\sigma(\nu)$  with frequency is nonmonotonic for some metals (C, N, O, Mg, Si, and S), giving them an outsized impact on the optical depth of at high frequencies despite their much lower relatively abundance (Appendix Fig. 20).

These species’ innermost K-shell electron can be ionized by X-ray photons with energies as low as 124 eV (Band et al. 1990) (Appendix Fig. 20), resulting in these metals having comparable EUV cross sections to H and He, but a much larger X-ray ionization cross sections. Several of those six species are among the most abundant species predicted in exoplanet atmospheres and even in the relatively small abundances of a 1×solar metallicity atmosphere (Asplund et al. 2009; Penzlin et al. 2024), the K-shell ionization cross section of metals weighted by abundance can be an order of magnitude higher than the abundance-weighted hydrogen ionization cross section. It is possible, then, that we may be missing the heating/ionizing contribution of X-rays to planetary outflows—even in the low flux limit—if we do not take into account metal opacities (e.g., Cecchi-Pestellini et al. 2006; Caldrioli et al. 2022).

Further complicating the X-rays picture, as seen in Gillet et al. (2023), highly energetic X-rays have the ability to ionize more than one atom/ion, which changes the energy and ionization budget throughout the wind depending on the local fraction of the gas that is already ionized (e.g., Habing & Goldsmith 1971; Shull & van Steenberg 1985; Dalgarno et al. 1999). On the whole, when X-rays are absorbed in the atomic upper atmosphere they are a significant source of flux which may be able to contribute to higher mass loss rates.

At the same time, metals contribute to a higher mean atomic weights, which, when coupled with metal line cooling, may result in lower mass loss rates than a pure-H model. This effect has been seen in disk photoevaporation models (Ercolano & Clarke 2010) and some atmospheric escape models (Huang et al. 2023; Linssen et al. 2024). Since X-rays and metals are predicted to have opposite effects, it becomes necessary to model the two together to understand the net effect of including both metals and X-rays on mass loss rate.

Carefully tracing the distribution of the energy of incident photons is important for capturing the contributions of X-rays and metals. First, we must determine what fraction,  $\epsilon_{s,\nu}$ , of the incident photons at each frequency,  $\nu$ , is absorbed directly by each species,  $s$ . We refer to the photon energy minus the energy of the initial ionization as  $E_{0,s}$ . Then, for X-ray and high energy EUV photons, we must determine what fraction of the energy,  $E_{0,s}$ , carried by the photoelectron released during the initial ionization of species  $s$  will contribute to heating the gas ( $f_{\text{heat}}$ ), what fraction ( $f_{\text{ion,tot}}$ ) will contribute to collisionally ionizing other species in the wind, and what fraction will collisionally excite H and be released as Ly $\alpha$  radiation ( $f_{\text{excite}}$ ) (Shull & van Steenberg 1985).

Starting with the fraction of the incident stellar XUV flux at frequency,  $\nu$ , that is initially absorbed by a species  $s$ , then,  $\epsilon_{s,\nu} = n_{0,s}\sigma_{s,\nu}/\sum_s n_{0,s}\sigma_{s,\nu}$ , where the  $\nu$  subscript indicates a dependence on frequency,  $n_{\text{col},s}$  is the volumetric number density of a given species, and  $\sigma_{s,\nu}$  is the species' photoionization cross section (Osterbrock & Ferland 2006). This relation is valid in both optically thin and optically thick regimes (Osterbrock & Ferland 2006). Note that the X-ray photoionization cross sections for certain species (C, N, O, Mg, Si, S) are an order of magnitude larger than the species' EUV ionization cross sections because, for those species, even soft X-rays are able ionize the K-shell electron. In those cases, the electron is removed from the innermost shell rather than the outermost and the ionizing energy required to do so is on order of hundreds of eV. K-shell X-ray photoionization cross sections are accounted for using the analytic approximations from Band et al. (1990). Other photoionization cross sections are computed from the Verner & Ferland (1996) database's coefficients and analytic fits.

X-rays further complicate ionization physics by allowing for secondary ionizations by energetic photoelectrons. While it is sufficient to assume that EUV photons are able to ionize only one species, more energetic X-ray photons can carry keVs of energy. For example, in the case of a 200 eV X-ray photon ionizing HI, the primary

photoelectron released during that initial ionization of HI will have energy  $E_{0,\text{HI}} = 200 - 13.6 \text{ eV} = 186.4 \text{ eV}$ . Hence, the primary photoelectron has enough energy to ionize several more species in the atmosphere. Thus, each X-ray photon can yield one primary and multiple secondary ionizations.

The number of secondary ionizations,  $\eta$ , that a species  $s$  experiences is parameterized using the prescription for a H-dominated atmosphere from Shull & van Steenberg (1985), with updated coefficients from Dalgarno et al. (1999). We opt for this parameterization rather than a constant  $\eta$  and heating efficiency, because where the photoelectron energy is distributed—whether into secondary ionizations or into heat—is a function the local ionization fraction,  $\chi$  (Shull & van Steenberg 1985; Gillet et al. 2023) and, therefore, will have significant impact on the wind structure. We take  $\chi$  to be the total ionization fraction instead of the hydrogen ionization fraction quoted in Shull & van Steenberg (1985) and find the difference to be negligible even in high metallicity cases (though cases where H is no longer the dominant species will require further investigation). This approach is also taken by Guo & Ben-Jaffel (2016). While more sophisticated prescriptions for the distribution of primary photoelectron energy exist (e.g., Salz et al. 2015; Cecchi-Pestellini et al. 2006), these require radiative transfer calculations or call on CLOUDY (Ferland et al. 2017) adding computational expense. We compare our wind structure using the Shull & van Steenberg (1985) and Dalgarno et al. (1999) prescription with the results of radiative-transfer based escape models in Appendix A.

If the local background ionization fraction,  $\chi(r)$ , is high—meaning the most abundant species is largely ionized—a larger fraction,  $f_{\text{heat}}(r)$ , of  $E_0$  will go into heating the gas and a smaller fraction,  $f_{\text{ion}}$ , will go into ionizing the gas. This distribution of energy is the result of elastic collisions between the photoelectrons and the high number of thermal electrons. These collisions transfer most of  $E_0$  to the thermal electrons, resulting in the heating of the gas. The opposite relation holds true if  $\chi$  is low: the energetic photoelectron is more likely to encounter a neutral atom,  $f_{\text{ion}}$  is higher, and  $f_{\text{heat}}$  is lower.

Shull & van Steenberg (1985)'s empirical equations for  $f_{\text{ion}}$  and  $f_{\text{heat}}$  as a function of  $\chi_H$  (the ionization fraction of hydrogen) are good approximations for X-ray stellar photons with energies  $> 100 \text{ eV}$ . The effect on the wind structure of lowering that energy floor to, e.g., 40 eV, is minimal. Above 40 eV, we model secondary ionizations. Below 40 eV, we do not model secondary ionizations and instead assume  $E_0$  goes entirely into heating.

### 2.4.3. Species-dependent Versions of Ionization and Heating Equations

Given the effect of secondary ionizations and heating when multiple species are present, we use a species-dependent version of Equation 5 for each species  $s$ :

$$879 \quad \mathcal{I}_s(r) = \mathcal{R}_s(r) - \mathcal{A}_s(r) \quad (12)$$

$$= n_{\text{ion},s}(r)n_e(r)\alpha_{\text{rec},s}(r) + \frac{1}{r^2}\frac{\partial}{\partial r}(r^2n_{\text{ion},s}v) \quad (13)$$

where  $n_{\text{ion},s}$  and  $n_e$  are the number densities of the higher ionization state of species  $s$  and *total* electron number densities, respectively. We take  $n_e = \sum_s (n_{\text{ion},s} \zeta_s + n_{0,s} (\zeta_s - 1))$ , where  $\zeta_s$  is the ionization number or the number of electrons removed from species  $s$ . The total number density is  $n_{\text{tot},s} = n_{0,s} + n_{\text{ion},s}$ , where  $n_{0,s}$  is the number density of the lowest state of species  $s$ .

The advection term,  $r^{-2}\partial(r^2n_{\text{ion},s}v)/\partial r$ , in Equation 13 for convenience can be written  $-n_{\text{tot},s}v\frac{\partial\Psi_s}{\partial r}$  by continuity, where  $\Psi_s = n_{0,s}/n_{\text{tot},s}$  is the number fraction of species  $s$  in the lowest state (a.k.a, the “neutral” fraction). This is the form we adopt in Wind-AE. The recombination coefficient,  $\alpha_{\text{rec},s}$  is temperature dependent and calculated using the recombination coefficient algorithm from CLOUDY (Ferland et al. 2017).

We define  $s$  as the species that is ionized either directly by a stellar photon or secondarily when a stellar photon of energy  $E_\nu$  first ionizes species  $j$  and that ionization releases a primary photoelectron carrying energy  $E_{0,j} = E_\nu - I_j$ , a portion of which goes into collisionally ionizing species  $s$ . Our updated local ionization rate per unit volume equation for species  $s$  irradiated by an SED with the frequency range  $[\nu_{\min}, \nu_{\max}]$  becomes,

$$905 \quad \mathcal{I}_s(r) \equiv \sum_{\nu=\nu_{\min}}^{\nu_{\max}} (\mathcal{I}_{1,s,\nu}(r) + \mathcal{I}_{2,s,\nu}(r)) \quad (14)$$

where  $\mathcal{I}_{1,s,\nu}$  is the primary ionization rate per unit volume as a function of radius and  $\mathcal{I}_{2,s,\nu}$  is the secondary, with

$$\mathcal{I}_{1,s,\nu}(r) = \epsilon_{s,\nu}(r) \Phi_\nu e^{-\tau_\nu(r)} \sigma_{s,\nu} n_{0,s}(r) \quad (15)$$

$$_{910} \quad \quad \quad \mathcal{I}_{2,s,\nu}(r) = \sum_{j=1}^{N_{\text{species}}} \mathcal{I}_{1,j,\nu}(r) \eta_{s,j,\nu}(r) \quad (16)$$

The photon flux per spectrum frequency bin is  $\Phi_\nu$ , (in units of  $cm^{-2} s^{-1}$ ),  $\tau_\nu$  is the total optical depth for all species, and  $\sigma_{s,\nu}$  is the ionization cross section as a function of frequency and species.

The number of secondary ionizations that species  $s$  experiences when impacted by a photoelectron emitted from species  $j$  is

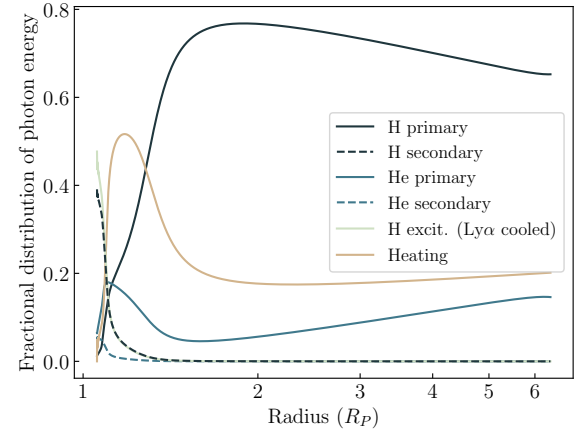


**Figure 3. Energy Deposition Fraction for HD 209458b** - Fraction of total incident stellar energy into ionizing hydrogen (black), helium (navy), heating (tan), and hydrogen excitation (light green) of which, in our model, 100% is assumed to escape as Ly $\alpha$  radiation. Total XUV flux over 13.6-2000 eV is 1095 ergs s $^{-1}$  cm $^{-2}$ .

$$\eta_{s,j,\nu} = \frac{E_{0,j} f_{ion,s}(r, E_{0,j})}{I_s}, \quad (17)$$

where  $I_s$  is the ionization energy of species  $s$ . The fractional distribution of photoelectron energy,  $E_{0,j} = E_\nu - I_j$ , when  $E_{0,j} > 40\text{eV}$  into heat, hydrogen excitations, and secondary ionizations is given by

$$f_{\text{heat}}(r) = 0.9971 \left[ 1 - (1 - \mathcal{X}(r)^{0.2663})^{1.3163} \right]$$

$$f_{\text{excite,H}}(r) = 0.4766 \left(1 - \chi(r)^{0.2735}\right)^{1.5221}$$

$$f_{\text{ion,s}}(r, E_{0,j}) = (1 - f_{\text{heat}} - f_{\text{excite,H}}) \frac{n_{0,s} \sigma_{\text{col,s}}(E_{0,j})}{\sum_m [n_{0,m} \sigma_{\text{col,m}}(E_{0,j})]}$$

where  $\sigma_{\text{col}}$  is the collisional ionization cross section (Dere 2007). This is equivalent to  $f_{\text{ion,s}} = n_{0,s} R_s(E_{0,j}) / \sum_m [n_{0,m} R_m(E_{0,j})]$ , so, for numerical speed, we use the spline tables for  $R_s$ , the secondary ionization rate coefficients, from Dere (2007). Recall that when  $E_{0,j} < 40\text{eV}$ ,  $f_{\text{heat}} = 1$  and  $f_{\text{ion,s}}$  and  $f_{\text{excite,H}}$  are 0.

The photoionization heating term for the energy conservation equation (Eq. 4) then becomes,

$$935 \quad \Gamma_{\text{ion}}(r) = \sum_s \sum_{\nu=\nu_{\min}}^{\nu_{\max}} \mathcal{F}_{s,\nu}(r) e^{-\tau_\nu(r)} \sigma_{s,\nu} n_{0,s}(r), \quad (18)$$

where,  $\mathcal{F}_{s,\nu}(r)$  is the energy flux of photoelectrons that goes into heating the gas and

$$_{938} \quad \mathcal{F}_{s,\nu}(r) = (E_\nu - I_s) [\epsilon_{s,\nu}(r) \Phi_\nu] f_{\text{heat}}(r). \quad (19)$$

939     Excited H releases a Lyman- $\alpha$  photon which we assume escapes, resulting in radiative cooling. We find  
 940

that, for HD 209458b for an H, He atmosphere that these excitations account for a total of 14% of the total incident energy (Fig. 3). Monte-Carlo radiative transfer calculations confirm that at least 51% of Lyman- $\alpha$  photons generated by H excitations should escape (see Appendix C). Thus, our net heating is off by less than 7%. To test the impact of including collisionally-excited Lyman- $\alpha$  photon heating on our model, we model HD 209458b with 0% of the Lyman- $\alpha$  photons escaping and 100% radiatively heating. We find that effect on the mass loss rate and structure of the planet is negligible.

The Shull & van Steenberg (1985) approximation for the secondary ionization rate of metals is not expected to be appropriate for high metallicities ( $> 50Z$ ) and future iterations of this model will include appropriate high metallicity physics. However, for low metallicities, we are able to model any species for which photoionization cross sections and collisional ionization rate coefficients as a function of frequency are available.

### 3. RESULTS OF INTRODUCING MULTI-FREQUENCY AND MULTISPECIES ASSUMPTIONS

#### 3.1. *Multispecies & Multi-frequency*

Though metals are required to understand the true impact of X-rays on an outflow, for clarity we first consider the difference between a wind launched by a multi-frequency spectrum and a mono-frequency spectrum in a low flux pure-H atmosphere, illustrated in Fig. 4. In the following section, we build up incrementally from the results presented in Murray-Clay et al. (2009) to elucidate the individual contributions of multi-frequency X-rays, metals, and boundary conditions. There has, naturally, been more detailed work since Murray-Clay et al. (2009) and we compare to those models in Appendix A and Section 5.4.

If we first implement multi-frequency X-rays without metals, as expected, the effect of adding X-ray photons (cyan), compared to a spectrum that extends only to the EUV (purple), is negligible since metals are not present in the atmosphere (Fig. 4). In addition to exploring the impact of mono- vs. multi-frequency stellar spectra, Figure 4 also highlights the impact of our lower boundary condition assumptions.

The differences in density, temperature, and ionization fraction structure between the two monofrequency models stem from differences in the structure of the bolometrically-heated region below the wind, which sets the radius at which the ionizing photons that drive the wind are deposited. Our updated boundary conditions yield a somewhat puffier atmosphere below the wind. We refer to this as increased “bolometric puffing”, a

process that is also modeled analytically and discussed in Owen & Schlichting (2023). Absorption of the 20 eV photons occurs at approximately the same pressure and density in both models; however, increased bolometric puffing increases the radius at which that density and pressure occur. This launches a wind from higher in the planet’s potential well, where less work needs to be done to reach the planet’s escape velocity. As a result, the velocity of the outflow is higher (Figure 4, gray versus black dash-dotted lines).

The wind launch radius,  $R_{\text{XUV}}$ , is often cited as 1 nanobar pressure (e.g., Murray-Clay et al. 2009). With the inclusion of multi-frequency XUV irradiation and a solar-like spectrum, however, we find that the winds for most planets launch closer to 10 nanobars, irrespective of planet mass. This is a result of the higher energy photons in a multi-frequency spectrum being deposited at a lower radius where the density is  $\sim 10\times$  higher than the radius at which monofrequency 20eV photons are absorbed.

Murray-Clay et al. (2009) found that the wind structure and mass loss rate are relatively insensitive to changes in the temperature at the base of the simulation ( $T(R_{\min})$ ); this remains true. Lifting the wind from shallower within the potential well results in a faster, hotter outflow with a higher  $\dot{M}$ , though the difference is modest (Fig. 4).

In other words, solutions for hot Jupiters with moderate escape velocities and ionizing fluxes like the one in Fig. 4 are not very sensitive to including a pseudo-molecular region below the wind with a higher mean molecular weight and bolometric heating and cooling (§2). However, inclusion of this layer can change the lower boundary dramatically for planets with lower escape velocities at the planet’s radius,  $R_P$ , including many sub-Neptunes (Owen & Schlichting 2023). This agrees with the findings of e.g., Allan & Vidotto (2019), who found that mass loss rates were sensitive to surface gravitational potential and thus  $\dot{M}$  changes with the wind launch radius.

While hot Jupiters typically have wind launch radii  $R_{\text{XUV}} \sim 1.1 - 1.3R_P$ , planets with lower escape velocities may have  $R_{\text{XUV}} \gtrsim 2 - 8R_P$ . Many works model mass loss using the energy-limited mass loss rate  $\dot{M}_{\text{Elim}} = \varepsilon F_{\text{XUV}} \pi R^3 / GM_P$  where  $\varepsilon$  is the efficiency,  $M_P$  is the planet’s mass, and  $R$  is chosen to be  $R_P$ , the IR photosphere radius (e.g., Erkaev et al. 2007; Kubyshkina et al. 2018b). Therefore, for low escape velocity planets, the energy-limited mass loss rate evaluated with  $R_P$  equal to the planet’s optical transit radius can dramatically underestimate the mass loss rate (Fig. 10). This finding is consistent with the literature (e.g., Erkaev

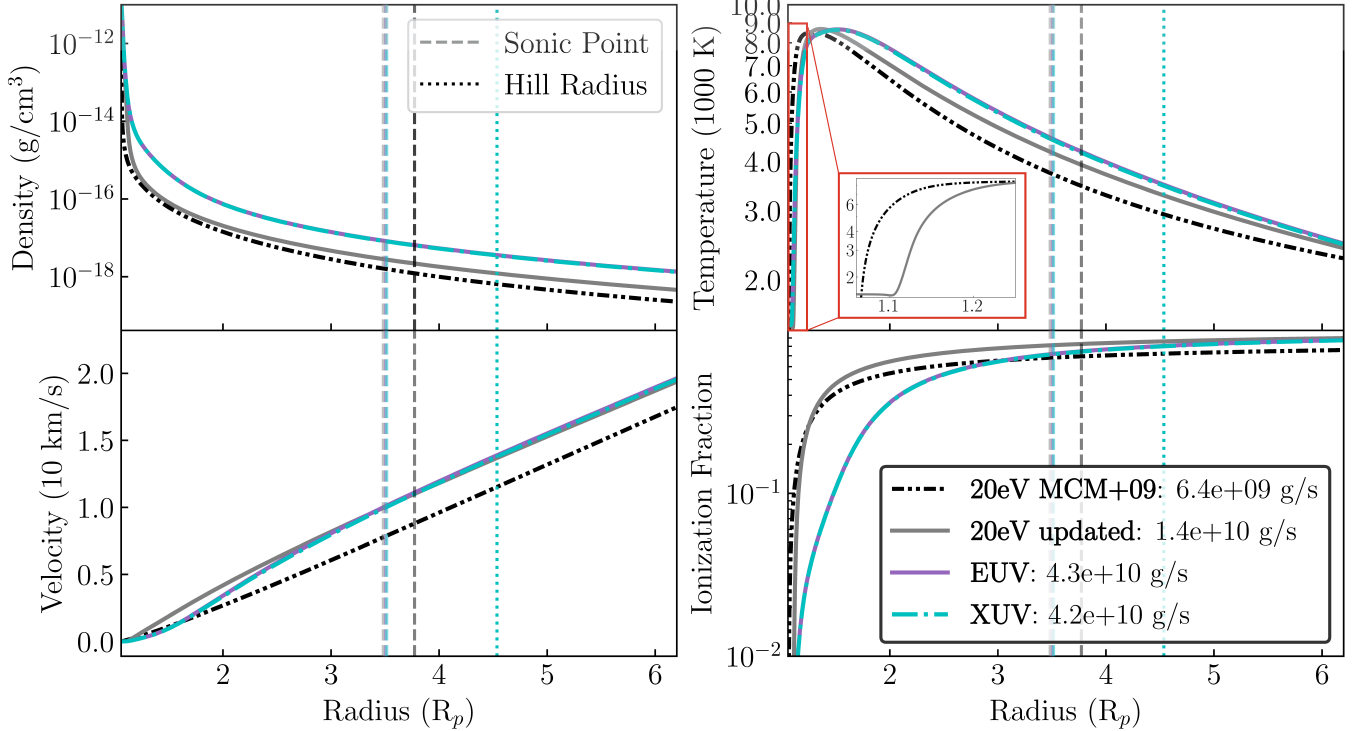


**Figure 4. Multi-frequency Profiles for a pure-H HD 209458 b** - Black dash-dotted is the original 20eV monofrequency and pure-H Murray-Clay et al. (2009) model ( $R_{\min} = 1.037 R_P$ ,  $\rho(R_{\min}) = 2.7 \times 10^{-11} \text{ g cm}^{-3}$ ,  $T(R_{\min}) = 1000 \text{ K}$ ). Gray solid is also monofrequency 20eV, but with our updated physical lower BC and bolometric heating and cooling at the base ( $R_{\min} = 1.057 R_P$ ,  $\rho(R_{\min}) = 1.8 \times 10^{-11} \text{ g cm}^{-3}$ ,  $T(R_{\min}) = 1534 \text{ K}$ ). The remaining plots all use the updated BCs. Purple is the EUV multi-frequency (13.6-100 eV) version. Because no metals are present, X-rays (cyan, dash-dotted, XUV 13.6-2000 eV) contribute relatively little to the profiles or mass loss rates of a pure-H atmosphere so the solutions overlap the EUV. Stellar spectra in all simulations are normalized to  $450 \text{ ergs s}^{-1} \text{ cm}^{-2}$  between 13.6 and 40 eV (in keeping with Murray-Clay et al. (2009)). Our model is not valid past the Coriolis radius (upper limit of x-axis). The sonic point and Hill sphere are given by dashed and dotted lines respectively.

et al. 2016; Kubyshkina & Fossati 2022; Huang et al. 2023); we discuss the outflow behavior in the high and low escape velocity limits in more detail in §5.

The remainder of the solutions in Fig. 4 all use the physical lower BCs detailed in Appendix B. The frequency-dependent forms of equations 14 and 18 allow us to trace the distribution of the photon energy throughout the wind. Here we choose to scale a FISM2 (daily average from 01-01-2009, Chamberlin et al. 2020) solar XUV SED to  $F_{\text{XUV}} = 1095 \text{ ergs s}^{-1} \text{ cm}^{-2}$  (normalized such that the integrated flux between 13.6-40 eV is  $450 \text{ ergs s}^{-1} \text{ cm}^{-2}$ ) which is the flux of HD 209458, a late F or early G type star experienced by planet b.

Changing the energy distribution of incident photons from a single frequency to multiple has the most significant impacts on the density and ionization structure of the wind (Fig. 4). To see why this is the case, consider the energy between 13.6 and 20 eV in the scaled solar spectrum. The 13.6-20 eV photons represent 40% of the total flux in the spectrum. Placing these photons all at

20eV overestimates the resulting heating and underestimates the ionization fraction. Notice that, relative to the monofrequency solution, the EUV solution in Figure 4 has a higher mass loss rate by a factor of 3 and an equal wind velocity.

The total flux,  $F_{\text{tot}}$ , of stellar photons is normalized in both the EUV and XUV cases such that the flux of photons with energies in the EUV range 13.6-40 eV is equivalent to the flux at 20 eV in the monofrequency case. This means that simulations quoted as XUV (spanning 13.6-2000eV) have a higher  $F_{\text{tot}}$  than those quoted as EUV (spanning 13.6-100eV, unless otherwise noted). The changes in temperature profile can be attributed in equal part to the presence of multi-frequency photons and higher  $F_{\text{tot}}$ .

Figure 5 shows the source of these multi-frequency-induced structural changes in the wind. When compared to a monofrequency 20eV solution with the same lower boundary physics and conditions, the energy of a 20 eV photon is absorbed much higher in the atmosphere.

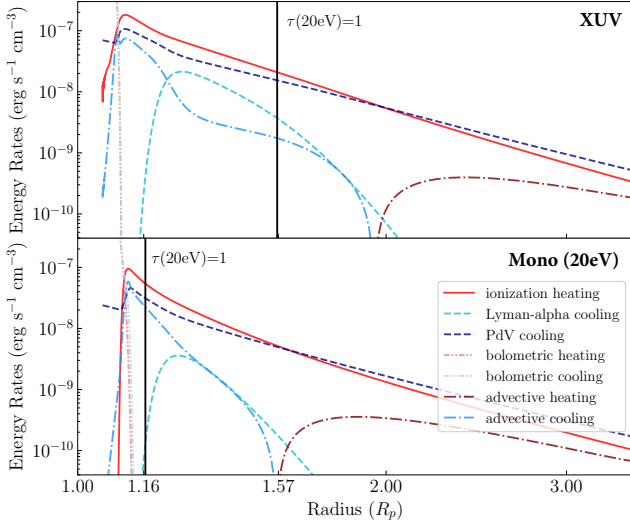


**Figure 5. Energy Plot for pure-H XUV vs. Monofrequency HD 209458 b** - Energy structure of multi-frequency XUV solution (top panel, cyan solution in Fig. 4) and 20eV monofrequency solution (bottom panel, gray solution in Fig. 4). The  $\tau(20\text{eV}) = 1$  surface for the XUV multispecies is at a higher radius because the deeper penetration of high energy XUV photons puffs up the atmosphere, resulting in higher densities and optical depths at higher radii than in the monofrequency solution.

This phenomenon is the result of the higher energy photons penetrating deeper into the atmosphere, puffing it up, raising the scale height of the atmosphere and causing lower energy photons to be absorbed higher in the atmosphere. Thus, the flux of a multi-frequency spectrum is deposited over a much broader physical range of  $\tau(\nu) = 1$  surfaces. This can explain the broadened peak in both the energy deposition (Fig. 5) and the temperature (Fig. 4) with radius.

The addition of metals somewhat tightens this radius range of XUV energy deposition (Fig. 6) and shifts it deeper into the potential well. When we add both X-rays and metals in solar abundance ( $Z_{\odot}$ ) to the planet HD 209458b (Fig. 6), we see that the higher ionization cross sections of metals mean that some of the X-rays are absorbed in the atomic layer and contribute to the wind, rather than being deposited deep below it. Our spectral range is lowered to 11.26-2000eV to capture the first ionization energy of CI and we do not lower to the ionization energy of MgI (7.65 eV) as MgI is immediately ionized to MgII, whose ionization energy is 15.04 eV. Thus, the integrated flux is  $1185 \text{ ergs s}^{-1} \text{ cm}^{-2}$ . Although we reserve a full exploration of the effect of metallicity for a future investigation, even in solar abundances, the metals have a significant role to play in the structure of the wind (if less so in the mass loss rate).

The mass loss rate is similar for both the single species and multispecies planets because the metals and X-rays have opposite effects on  $\dot{M}$ .

The metals increase the mean atomic weight, lowering the scale height, increasing the density and opacity of the outflow (Fig. 6), but, more importantly, lowering the sound speed,  $c_s$  which raises the sonic point of the outflow (an isothermal Parker wind has its sonic point at  $R_{\text{sp}} = GM_p/(2c_s^2)$ ). Multiple species therefore serve to lower the mass loss rate because of their effect on  $\mu$ . Conversely, X-rays penetrate deeper into the atmosphere where the density is higher and can drive an outflow that is more massive, slower, and more ionized thanks to secondary ionizations.

### 3.2. Tidal Gravity and Comparison to Energy Limit

Returning to the canonical example of HD 209458b—this time with an H-He atmosphere—we also plot  $\dot{M}$  as a function of semi-major axes spanning from 0.03 to 0.7 au. A changing semi-major axis,  $a$ , not only influences the amount of flux at the planet's location, but also affects the stellar tidal gravity (Eq. 3). We plot a high ( $1.095 \times 10^5 \text{ ergs s}^{-1} \text{ cm}^{-2}$ ) and low flux ( $1095 \text{ ergs s}^{-1} \text{ cm}^{-2}$ ) series to approximate the behavior of young and old stars, respectively (§3.3). It is intentional that we do not include lower fluxes for the “old star” low flux case, because while those stellar fluxes corresponding to  $a > 0.4$  au can launch winds, conductive cooling becomes significant at those extremely low fluxes. We do not model conductive cooling, so we exclude all simulations for which postfacto calculations of the conductive cooling rate per unit volume as a function of radius show it to be  $\geq 5\%$  of the total heating rate per unit volume. Since  $F_{\text{tot}} \propto a^{-2}$  and the tidal gravity term is  $\propto a^{-3}$ , the tidal gravity is significant for close-in planets, but negligible at larger semi-major axes. The transition is illustrated by the low flux old star in Figure 7. Along with our model’s  $\dot{M}$ , we plot the energy limited  $\dot{M}_{\text{Elim}}(\varepsilon) = \varepsilon F_{\text{tot}} \pi R_P^3 / GM_P$ , where  $\varepsilon$  is the efficiency with which stellar photon energy is converted to heat, and the tidally-corrected energy limited

$$\dot{M}_{\text{tidal}}(R, \varepsilon) = \frac{\varepsilon F_{\text{tot}} \pi R^3}{GM_P} \left( 1 - \frac{3}{2\xi} - \frac{1}{2\xi^3} \right)^{-1} \quad (20)$$

where  $\xi = R_{\text{Hill}}/R_P$ , the ratio of the planet’s Hill sphere and  $R$ , where  $R$  is traditionally taken to be  $R_P$  (Erkaev et al. 2007).

The energy limited mass loss approximation is an upper limit on a planet’s mass loss rate that assumes that the incident stellar flux is converted with efficiency,  $\varepsilon$ , into heating the wind and driving an outflow. Planets with lower incident stellar flux are generally said to be

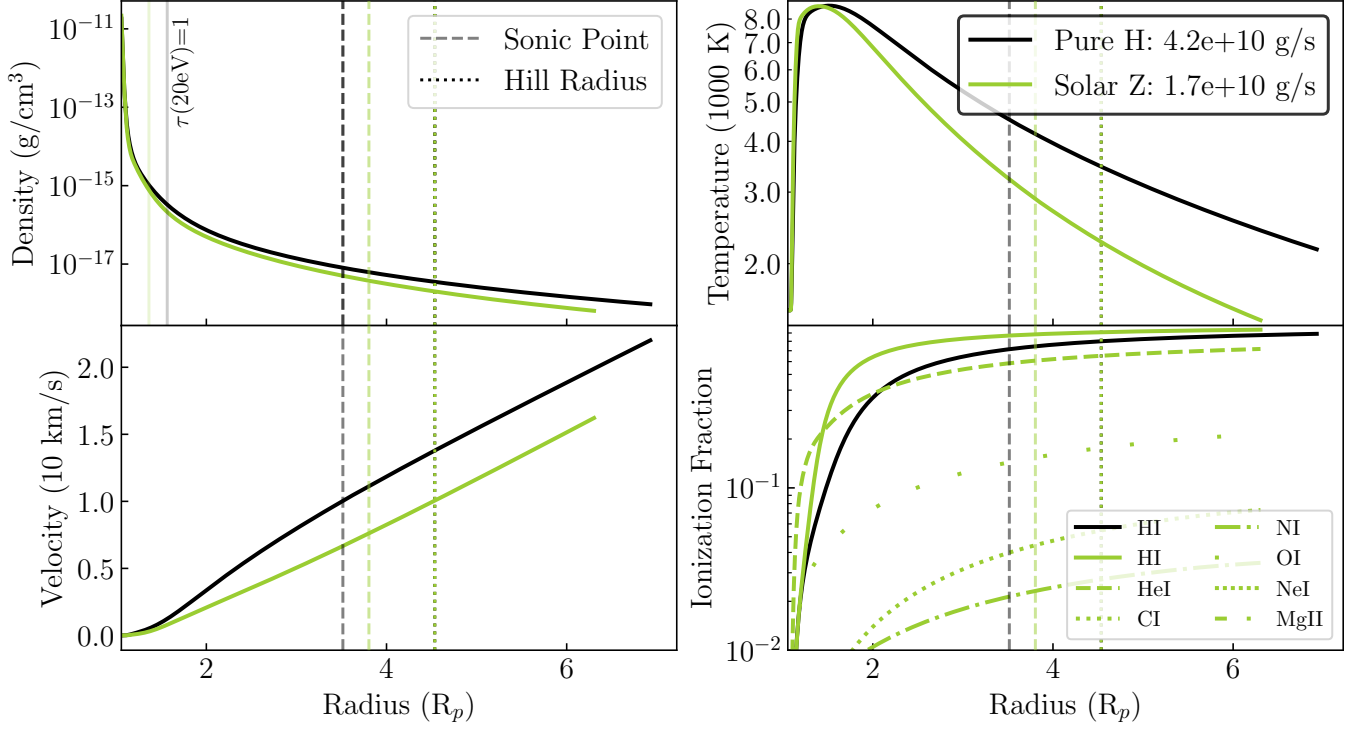


**Figure 6. HD 209458b Multispecies** - Pure hydrogen (black) and solar abundances of HI, HeI, CI, NI, OI, NeI, MgII (green) XUV (11.26-2000eV) solutions. Vertical lines: Sonic points (dashed), Hill radius (dotted),  $\tau(20\text{eV})=1$  surfaces (light solid), and solutions end at the Coriolis radius for each simulation.

in the “energy-limited” regime, meaning that the mass loss rate is directly proportional to flux and adding additional flux will result in a higher  $\dot{M}$  - to a point. Once a planet has sufficiently high flux, the limiting factor on  $\dot{M}$  is the rate at which species can recombine and the planet is said to have entered the “recombination-limited” mass loss regime. We directly compute  $\varepsilon$  for each point in this plot by computing the frequency-averaged efficiency of energy deposition into heat (as opposed to ionizations), taking into account secondary ionizations. Radiative cooling is not included in our efficiency. We find that our values range between  $\varepsilon \sim 0.3 - 0.4$ .

For the “old” star which has the current day  $L_{\text{XUV}}$  of HD 209458,  $\dot{M}$  approaches the tidally-corrected energy limit for very close-in planets, but diverges for planets at larger separations (Fig. 7a) (Schulik & Owen 2024). Despite being two orders of magnitude higher flux, the “young” star does not approach the energy limit, because the Lyman- $\alpha$  cooling is more significant for higher flux stars because the planets’ upper atmospheres are able to reach temperatures closer to the  $\sim 10,000$  K at which Ly- $\alpha$  cooling efficiency peaks.

The dependence of  $\dot{M}$  on tidal gravity also results in an update to Figure 7 of Murray-Clay et al. (2009), which plotted  $\dot{M}$  as only a function of changing  $F_{20\text{eV}}$  (which was the total flux concentrated at 20 eV). With

the inclusion of XUV multi-frequency radiation and an H-He atmosphere with  $F_{\text{tot}}$  normalized such that the flux in the EUV range of 13.6 - 40 eV the same as the  $F_{20\text{eV}}$  in Murray-Clay et al. (2009), if the planet’s distance is held constant at 0.05 au, we reproduce a similar result (Fig. 7b). The characteristic relationship found by Murray-Clay et al. (2009), where  $\dot{M} \propto F_{20\text{eV}}^{0.9}$  in the energy-limited regime (low fluxes) and  $\dot{M} \propto F_{20\text{eV}}^{0.6}$  in the recombination-limited regime (high fluxes), holds when distance is held constant. Tidal gravity is present in both models, but its impact is not noticeable without changing the semi-major axis. When the semi-major axis is also changed, the magnitude and slope of the flux- $\dot{M}$  relationship changes dramatically as a result of the tidal gravity. Our derived lower boundary temperature,  $T(R_{\min})$ , also has a semi-major axis dependence (Appendix B), but tidal gravity is the dominant contributor to the mass loss rate.

The aiding effect of tidal gravity is evident where the orange and cyan lines intersect with the gray in Figure 7b. At 0.05 au the tidal gravity is equivalent to the case in which distance is held constant. At 0.03 au, the tidal gravity contribution elevates the mass loss rate above that of the equivalent flux at 0.05 au. We can turn off tidal gravity in our simulations, but elect to keep it on, as it has a significant effect on mass loss rates

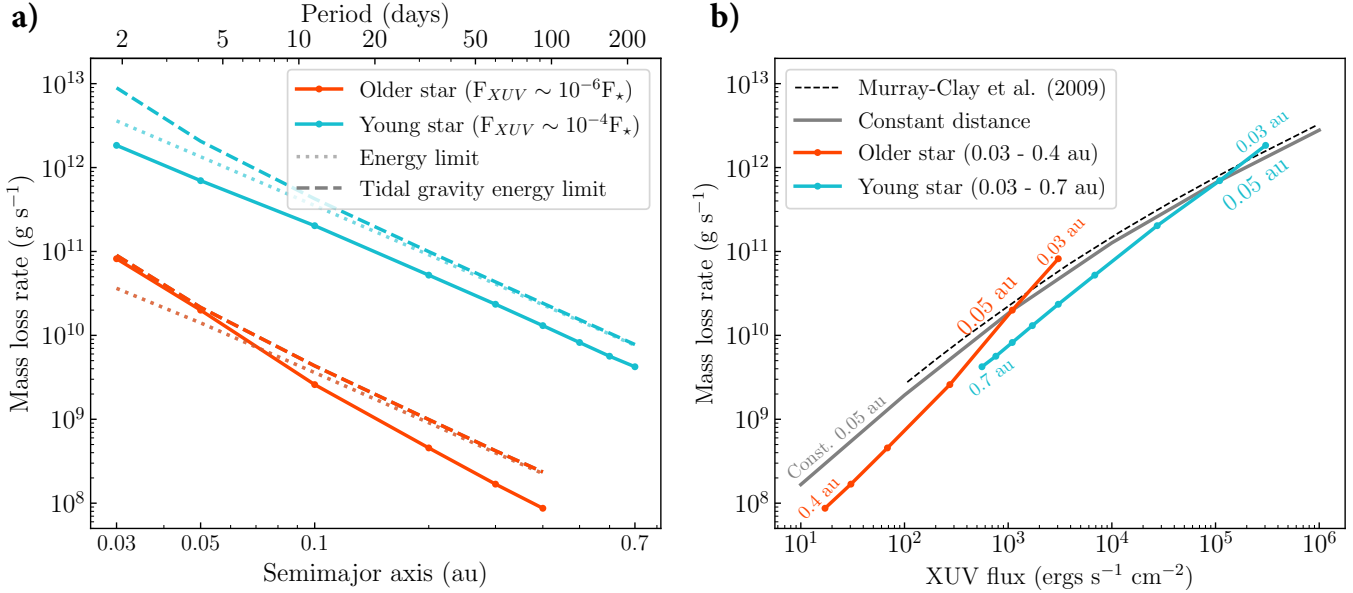


**Figure 7.  $\dot{M}$  and tidal gravity -** (a)  $\dot{M}$  for a planet with parameters of HD 209458b and a multi-frequency XUV, H-He atmosphere is plotted as a function of semi-major axis,  $a$ , in au (solid lines) for a high XUV activity “young” HD 209458 ( $F_{\text{XUV}} \sim 10^{-4} F_*$ , cyan) and lower XUV flux older HD 209458 ( $F_{\text{XUV}} \sim 10^{-6} F_*$ , orange). Low flux is  $F_{\text{XUV}} = 1095 \text{ ergs s}^{-1} \text{cm}^{-2}$  and high  $F_{\text{XUV}} = 1.095 \times 10^5 \text{ ergs s}^{-1} \text{cm}^{-2}$  at 0.05 au and the stellar spectral shape does not change. Flux scales with  $a^{-2}$ . Traditional energy-limited  $\dot{M}$  (dotted) and Erkaev et al. (2007)’s tidal-gravity-corrected energy limit  $\dot{M}$  (dashed) with our modeled efficiencies (average 0.37, computed point by point as described in Section 3.2) are plotted for both flux regimes. (b) Mass loss is plotted as a function of XUV flux. We reproduce Murray-Clay et al. (2009)’s Fig. 7 (black dashed) for a pure H, 20 eV monofrequency simulation, in which semi-major axis is held constant while flux at 0.05 au is varied. The  $\dot{M}$  values are multiplied by the geometric reduction factor of 0.33 for consistency with our current results. The gray line is an update of the previous constant distance line, now with an XUV multi-frequency spectrum and an H-He atmosphere. The computed  $\dot{M}$ s for young and older stars from the left are overplotted. The difference in slope is the result of tidal gravity. We assume all planets are tidally-locked, meaning that we use a constant geometric reduction factor.

for planets whose potential well would otherwise be too deep to launch a wind.

### 3.3. As a Function of Planet Type

The additions of multi-frequency photons and multiple species highlighted the importance of where in the potential well the wind launches. Planet mass and radius, then, are unsurprisingly important since the planet’s escape velocity sets the amount of energy required to lift the wind out of the potential well.

For an approximately 5-Gyr-old solar mass and luminosity star, we model three generic planets of varying sizes located at 0.05 au. The first is a hot Jupiter of  $0.7 M_J$  and  $1.4 R_J$ , the second is a Neptune-mass and -radius planet, and the third is a super-Earth with  $5 M_\oplus$  and  $2 R_\oplus$  (Figure 8).

We compute the total XUV flux (13.6 - 2000 eV) from the stellar age-XUV flux relation in (King & Wheatley 2021a). For a 4.5-Gigayear-old star like our Sun, the ratio of XUV to total bolometric luminosity has been estimated to be  $L_{\text{XUV}}/L_{\text{bol}} \sim 10^{-6}$ . We take it to be  $F_{\text{tot}} = 1095 \text{ ergs s}^{-1} \text{cm}^{-2}$ , appropriate for the low-activity Sun. These models, and all others henceforth,

model a hydrogen-helium atmosphere where the mass fraction in H is 0.8 and in He is 0.2. The escape velocity at  $R_P$  of the hot Jupiter is the highest of the three planets ( $v_{\text{esc}} = 4.6 \times 10^6 \text{ cm s}^{-1}$ ). The Neptune-like planet has  $v_{\text{esc}} = 2.4 \times 10^6 \text{ cm s}^{-1}$  and the super-Earth has  $v_{\text{esc}} = 1.8 \times 10^6 \text{ cm s}^{-1}$ .

For the hot Jupiter, the scale height is smaller and photons are absorbed closer to the planet’s surface<sup>4</sup> than on smaller planets, resulting in a wind that launches from a relatively lower  $R_{\text{XUV}}$  (Fig. 8). This radius is deeper in the potential well, so the wind requires more heating in order to escape the planet’s gravitational pull, so the outflow has a much higher maximum temperature of 8800 K than the Neptune-like planet (3600 K) and the super-Earth (2900 K). One consequence of this much higher temperature is that the Lyman- $\alpha$  cooling is more significant for the hot Jupiter, which, along with the rapid drop in density with radius results in the steep drop off in temperature. The small scale height means

<sup>4</sup> as measured by the planet’s optical transit radius

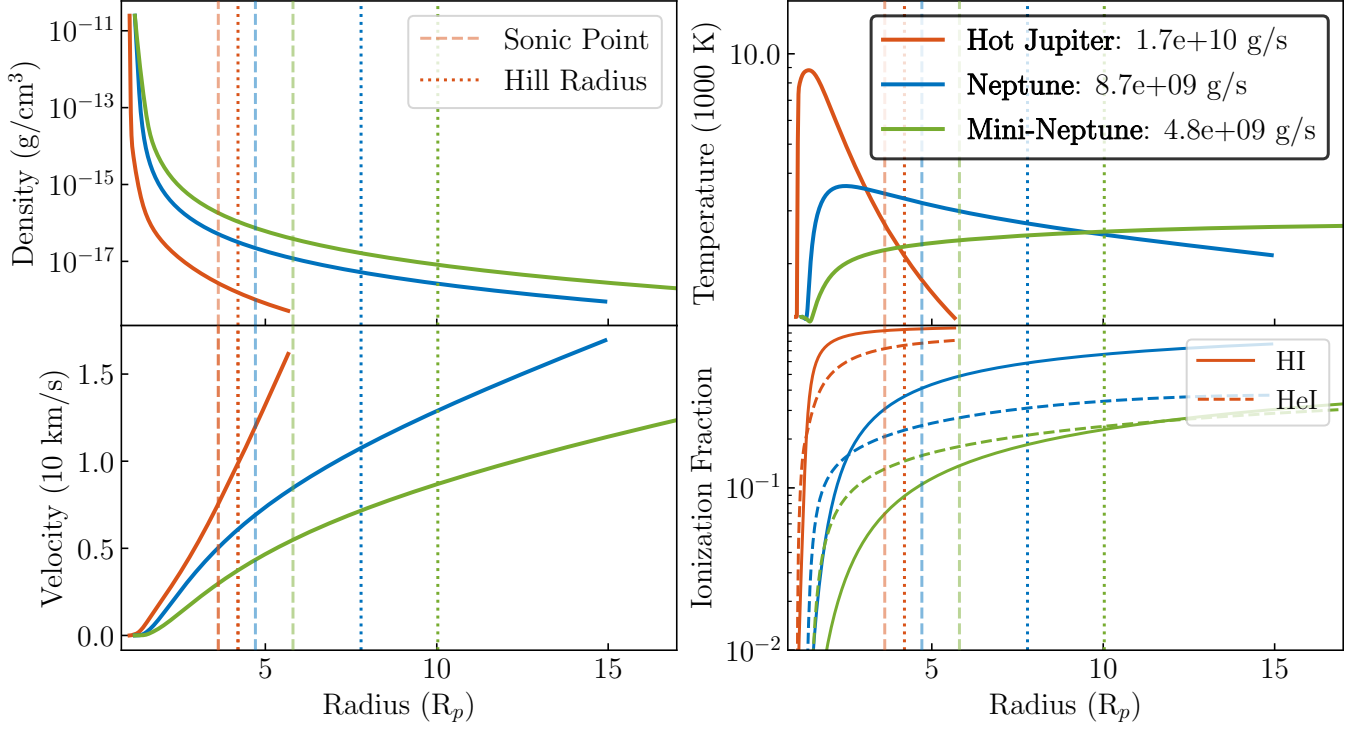


**Figure 8. Hot Jupiter, Neptune, and Mini-Neptune Outflows** - Wind structure of H-He (0.8:0.2 mass fraction) atmospheres for a  $0.7 M_J$ ,  $1.4 R_J$  ( $222.6 M_\oplus$ ,  $15.7 R_\oplus$ ) planet (orange) with escape velocity of at  $R_P$  of  $v_{\text{esc}} = 4.6 \times 10^6 \text{ cm s}^{-1}$ , a Neptune-sized  $17 M_\oplus$ ,  $3.9 R_\oplus$  planet (blue) with  $v_{\text{esc}} = 2.4 \times 10^6 \text{ cm s}^{-1}$ , and a mini-Neptune with  $5 M_\oplus$ ,  $2 R_\oplus$  (green) with  $v_{\text{esc}} = 1.77 \times 10^6 \text{ cm s}^{-2}$ . All three are located at 0.05 au around a  $1 M_\odot$  and  $1 L_\odot$  star, with total flux at 0.05 au of  $F_{\text{tot}} = 1095 \text{ ergs s}^{-1} \text{ cm}^{-2}$  (13.6-2000eV). All are plotted in terms of their  $R_P$ , but all have different  $R_P$  values. The super-Earth's small thermal inversion below the wind (where larger planets have an isotherm) is the result of bolometric heating/cooling naturally falling off before photoionization heating becomes significant and the wind launches.

that the hot Jupiter also absorbs the incident multi-frequency photons over a smaller range of heights in the atmosphere, which gives the much narrower temperature peak and the faster ionization with radius. The rapid ionization with radius is also a result of the distribution of stellar photon and photoelectron energy between heating and ionization.

A hotter wind is almost always a faster wind and the three planets are consistent with this relationship. Because the smaller planets absorb photons over a broader range of radii, require less heating to launch a wind, and thus have a slower decrease in density with radius, they also ionize more slowly as a function of planetary radius. For all planets, at the lowest radii in the wind, He ionizes in greater fraction than H does. This is particularly pronounced for the super-Earth.

Since the relaxation method is relatively fast, we are able to run a grid of 663 points inexpensively<sup>5</sup>. The majority of the time per point is the “polishing” process in which we enforce self consistency in the upper and lower boundary conditions. This speed was aided by our choice to create a non-linear grid that spans the total mass range of  $0.009 - 1.66 M_J$  ( $3 - 528 M_\oplus$ ) and a radius range of  $0.165 - 2.02 R_J$  ( $1.85 - 22.65 R_\oplus$ ). The 53 steps in radius space are linear, but the masses are chosen such that the grid lines constitute lines of constant escape velocity,  $M_{\text{P,init}}/1.85 R_\oplus$ , where  $M_{\text{P,init}}$  is the linear array of 12 initial masses that span from  $3 M_\oplus$  to  $43 M_\oplus$ . These mass and radius ranges are chosen to cover the range of observed masses and radii of super-Earths, sub-Neptunes, and hot Jupiters with semi-major axes of 0.05 au. The results are presented in Figure 9 for an “old” star flux (left) and a “young” star flux (right).

1268

#### 4. MASS LOSS GRIDS

##### 4.1. $\dot{M}$ as a Function of Planetary Parameters

1269

<sup>5</sup> About 1 hour run in pseudo-parallel (simultaneous sequential runs) on an 8-core laptop with an M1 chip. Relative computation time comparisons are made in Appendix A.

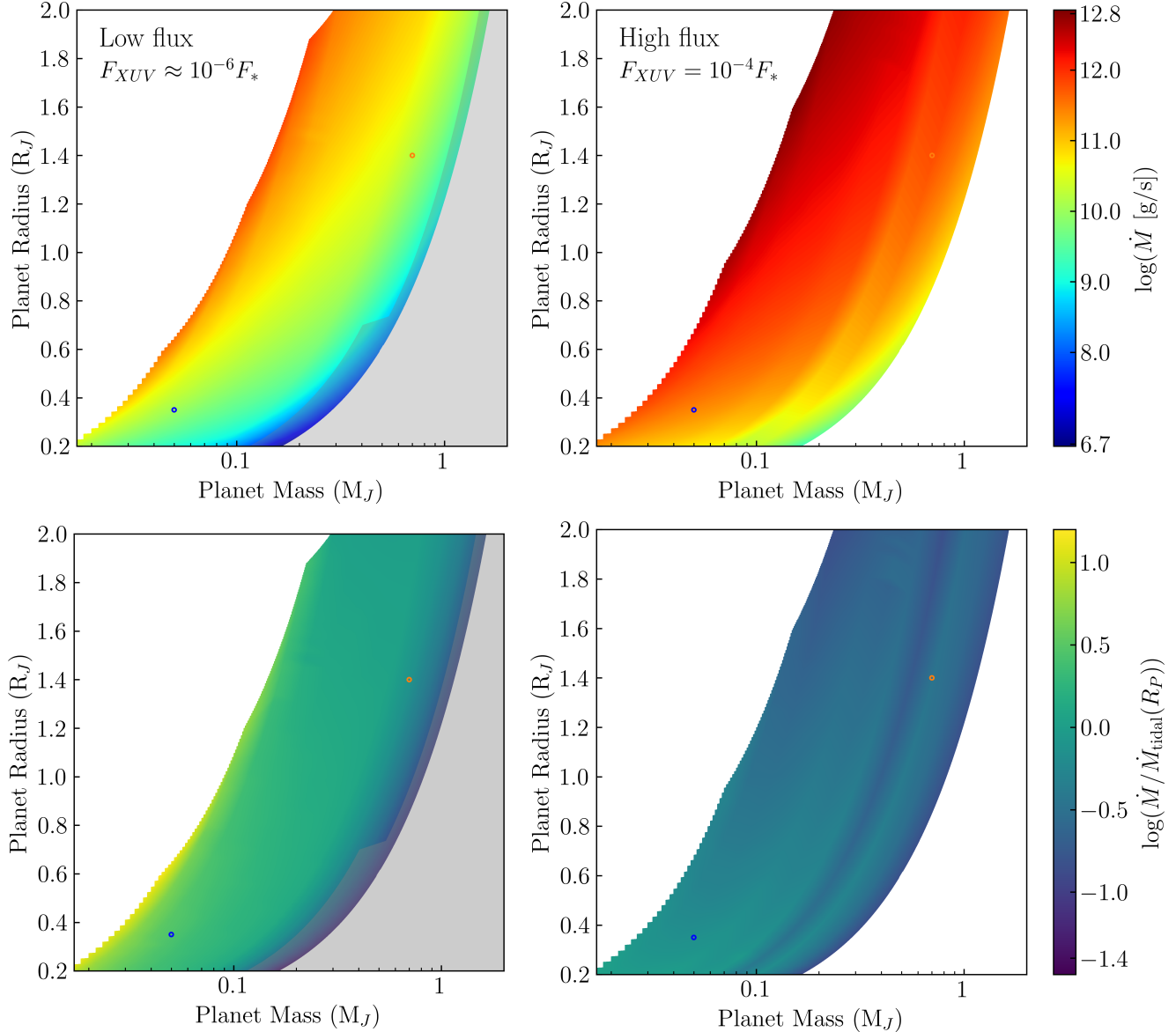


**Figure 9.  $\dot{M}$  grids for Low and High Fluxes** - 2D-linearly-interpolated grid of 663 H-He planets located at 0.05 au around a solar mass, solar luminosity star. Fluxes correspond to an old star ( $F_{\text{XUV}} \approx 10^{-6} F_*$ ) of  $1095 \text{ ergs s}^{-1} \text{ cm}^{-2}$  (left column) and a younger star ( $F_{\text{XUV}} \approx 10^{-4} F_*$ ) of  $109500 \text{ ergs s}^{-1} \text{ cm}^{-2}$  (right column). Locations of a Neptune- and HD 209458b-analog are plotted as blue and orange points, respectively. The greyed out region represents where conductive cooling—which we do not model—would be significant. The top row is colormapped to the log of the mass loss rate in g/s and the bottom to the log of the ratio of  $\dot{M}$  with the tidally-corrected energy limited  $\dot{M}(R_P)$  (Equation 20) with efficiencies calculated on a point-by-point basis in the grid (low-flux  $\langle \varepsilon \rangle = 0.37$ , high-flux  $\langle \varepsilon \rangle = 0.33$ ). See §5.1 for a discussion of the bifurcation near  $0.1 M_J$  in the high flux grids.

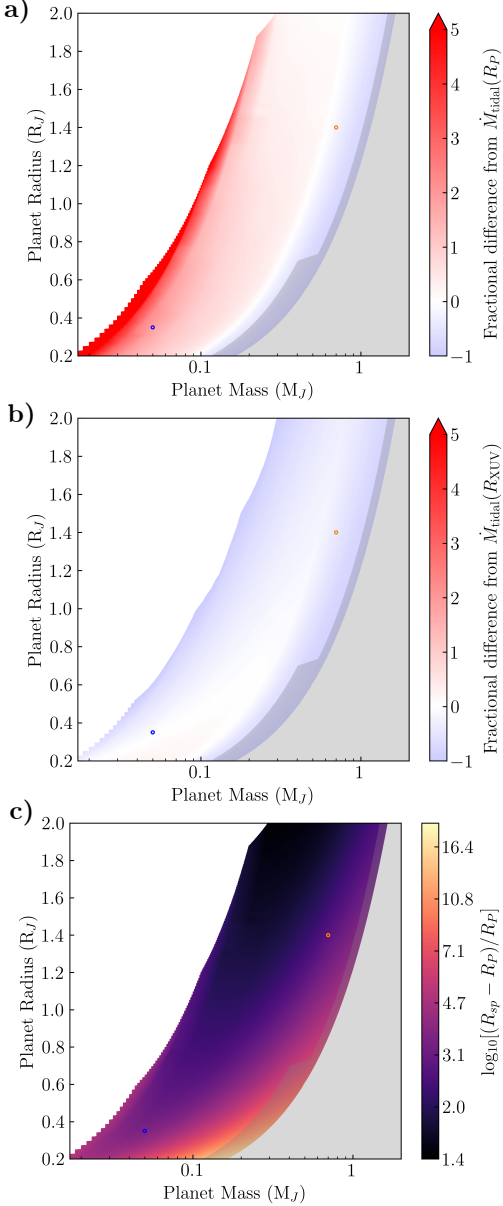


**Figure 10.**  $\dot{M}$  relative to energy limited mass loss rates - (a) Low flux ( $1095 \text{ ergs s}^{-1} \text{ cm}^{-2}$ ) fractional difference  $(\dot{M} - \dot{M}_{\text{tidal}}(R_P)) / \dot{M}_{\text{tidal}}(R_P)$ , from tidally-corrected energy limited mass loss rate computed at  $R_P$ . We use the same grid as Fig. 9. Orange and blue dots correspond to an HD 209458b and Neptune-analog, respectively. Red indicates that  $\dot{M}_{\text{tidal}}$  underestimates the mass loss rate computed by our model and blue indicates that  $\dot{M}$  is less than the energy limit, as is expected. (b) Same colorbar scaling as (a), here we plot  $(\dot{M} - \dot{M}_{\text{tidal}}(R_{\text{XUV}})) / \dot{M}_{\text{tidal}}(R_{\text{XUV}})$ . (c) Height of the sonic point above  $R_P$  in units of  $R_P$ . All  $R_{\text{sp}}$  are below the Hill radii, except at the lowest escape velocity edge (off the left edge of the plot), where the outflow transitions to boil-off or core-powered mass loss—evaluation of our code’s performance in this regime is beyond the scope of this work.

The grid is limited by a number of numerical and physical limitations. The lower end of the mass range of super-Earths ( $M_P \leq 3.5 M_{\oplus}$ ) is limited by the numerical failure to converge to a wind solution. This failure is not purely numerical in nature, though, because these planets are so low escape velocity and optically thick that  $R_{\text{XUV}}$  can be as large as  $8R_P$ . In these extreme cases, when we compute the sonic point for a wind driven purely by bolometric radiation,  $R_{\text{sp,bolo}} \approx GM_P/(2c_s^2)$  for the sound speed,  $c_s$ , at the  $R_{\min}$ , we find that  $R_{\text{sp,bolo}}$  is of order  $R_{\text{XUV}}$ . This means that the bolometric heating is sufficient to launch a transonic wind and the XUV photons are being absorbed near or within the super-sonic region of the wind. The XUV photons cannot contribute to heating and driving a wind, hence, these flows are likely not photoionization-driven winds, but rather are still undergoing boil-off or core-powered mass loss (as in Rogers et al. 2021; Tang et al. 2024).

We make a similar cut at the upper end of masses. Our maximum initial mass for  $R_P = 1.85 R_{\oplus}$  is  $43 M_{\oplus}$  to avoid unphysically dense planets. Wind-AE is capable of modeling these extremely dense planets, though at high enough escape velocities, it eventually suffers from numerical and physical difficulties discussed in §5.1. However, we cut off our grid at the high escape velocity end because, for low  $F_{\text{XUV}}$ , conductive heating and cooling are significant and we do not model conduction. Furthermore, when we plot the ratio between the tidally-corrected energy limited mass loss rate,  $\dot{M}_{\text{tidal}}(R_P, a, \varepsilon)$  and the  $\dot{M}$  found by our model (Figure 9, bottom panels), we see that for these high escape velocity planets,  $\dot{M}$  is more than an order of magnitude below the energy limit.

We plot the fractional difference of our computed values of  $\dot{M}$  from the energy-limited estimate,  $(\dot{M} - \dot{M}_{\text{tidal}}) / \dot{M}_{\text{tidal}}$  in Figure 10 with the heating efficiencies computed point by point as before (for the low flux case  $\langle \varepsilon \rangle = 0.37$ , high flux  $\langle \varepsilon \rangle = 0.33$ ). Given that  $\dot{M}_{\text{tidal}}(R, a, \varepsilon)$  is the theoretical upper limit on mass loss rates, it should not be possible for our mass loss rates to be higher for the same efficiency value,  $\varepsilon$ , as the amount of red in Figure 10a seems to suggest. However,  $\dot{M}_{\text{tidal}}$  is derived assuming that all of the photon energy is deposited near  $R_{\text{XUV}} \approx R_P$  and the optical transit radius,  $R_P$ , is frequently used in the energy-limited mass loss equation. This assumption is a good one for hot Jupiters. However, as we have seen, for planets with lower escape velocity, multi-frequency photons and bolometric heating/cooling below the wind drive  $R_{\text{XUV}} \gg R_P$ . Thus,  $\dot{M}_{\text{tidal}}(R_P)$  will always underestimate the energy-limited mass loss rate for lower gravity planets. Instead, it is necessary to use  $\dot{M}_{\text{tidal}}(R_{\text{XUV}})$ .

Indeed, when we compute  $\dot{M}_{\text{tidal}}(R = R_{\text{XUV}}, 0.05\text{au}, \varepsilon)$ , for the low flux grid, we see that our mass loss rates are below this photoionization-radius-corrected mass loss rate (Fig. 10b) and thus do not violate the maximum energy available. Note that the valley feature in Figure 10b can also be seen in Figure 13 of Owen & Jackson (2012), though we disagree with some of the aspects of the model therein and compare in more detail to it in Appendix A.

The findings in Figure 10 differ slightly from the results of Kubyshkina et al. (2018b), who found that the tidally-corrected energy limited mass loss rate computed at  $R_{\text{XUV}}$  for a heating efficiency of 0.15 underestimates mass loss rates for the lowest density planets. The Kubyshkina et al. (2018b) grids span lower planetary radii and masses ( $1\text{-}10 R_{\oplus}$ ,  $1\text{-}39 M_{\oplus}$  vs. our  $1.85\text{-}22.65 R_{\oplus}$ ,  $3.8\text{-}528 M_{\oplus}$ ) than our model can currently do without conductive cooling, but the lower left quadrant of, e.g., Figure 10 corresponds to a similar range of masses and radii.

The primary source of the discrepancy is the efficiency in Equation 20. When we compare our mass loss rates to  $\dot{M}_{\text{tidal}}(R_{\text{XUV}}, \varepsilon = 0.15)$  as in (Kubyshkina et al. 2018b) instead of the escape-velocity-dependent  $\varepsilon = 0.26\text{-}0.38$  in Figure 10b, we likewise find that  $\dot{M}_{\text{tidal}}$  overestimates the mass loss rates for low density planets. It is also likely that we find slightly higher  $R_{\text{XUV}}$  on average than the  $R_{\text{eff}}$  computed by Kubyshkina et al. (2018b). Both methods take the absorption radius to be the point of maximum ionization, but the input stellar spectrum in Kubyshkina et al. (2018b) is parameterized as two monofrequency EUV (20 eV) and X-ray (247 eV) bins. This is an appropriate parameterization for computational efficiency, but, as Figure 5 shows for monofrequency EUV vs. multi-frequency XUV, will result in a slightly lower estimate for  $R_{\text{XUV}}$ .

These discrepancies further validate the ultimate conclusion of Kubyshkina et al. (2018b): regardless of the relative accuracy of the energy limited approximation for lower flux planets, it still requires accurately estimating both  $R_{\text{XUV}}$  and the heating efficiency a priori.

For planets in the high flux limit, however, it is not necessary to find  $R_{\text{XUV}}$  to compute a reasonable estimate for the tidally-corrected energy limited mass loss rate. In Figure 10 we do not show the fractional difference for the high flux case, because the planets are in the radiation/recombination-limited mass loss regime, meaning that radiative cooling is energetically important. As such,  $\dot{M} < \dot{M}_{\text{tidal}}(R_P)$  for the extent of the high flux grid.

Slices of an even higher flux grid are included in Appendix A, Figure 17 where we compare to the high-

XUV-flux-limit mass loss rate grids of Owen & Jackson (2012). In short, we find that the lack of PdV and Ly $\alpha$  cooling in the Owen & Jackson (2012) model results in very different mass loss rates across the grid, highlighting the importance of those two cooling sources even in recombination-limited outflows.

## 5. DISCUSSION

### 5.1. High Escape Velocity Limit

Atmospheric escape in the high escape velocity limit ( $\gtrsim 5 \times 10^6 \text{ cm s}^{-1}$ ) will be explored in more detail in future works, but we make note of a couple of interesting features here. The first few numerical and physical complications result from the small scale height that results from high escape velocity at large planet masses.

A small scale height not only yields an atmosphere that is more compressed, it means that most of the ionizing photons are absorbed very deep in the potential well. This means that it can be difficult physically for these planets to launch winds, since they require a large flux to achieve sufficient energy to launch. For the same reason, these outflows can reach  $> 4000 \text{ K}$  before launching (e.g., the temperature difference between planets of varying surface gravity in Figure 8). Inspection of these planets' energy distributions reveals that they experience significant Lyman- $\alpha$  cooling, even when they experience relatively low fluxes. Ly- $\alpha$  cooling is significant for these planets because the planets' deep potential wells necessitate high temperatures to escape, so these atmospheres heat to high temperatures where Ly- $\alpha$  is efficient before the atmospheres outflows, which agrees with the analytic predictions of Owen & Wu (2016).

Even when Wind-AE can find a solution, for high escape velocity and low flux planets, the default base boundary condition radius of the  $1\text{-}\mu\text{bar}$  radius may not capture all of the  $\tau(\nu) = 1$  surfaces for the highest energy photons. Instead, the wind launches immediately at the base of the simulation and  $R_{\text{XUV}} = R_{\min}$ . In these cases, when computing our grids, we raise  $T(R_{\min})$  several thousand Kelvin from the expected temperature in the bolometrically-heated region,  $T_{\text{skin}}$  to account for the fact that we are essentially beginning our model mid-wind launch (see Appendix B for more details). Because we do not capture all of the photoionizing photons in our simulation, we lose up to 10% of the flux out of the bottom of the simulation. We have validated that this procedure provides a good match for solutions that set the simulation base at higher densities and take substantially longer to converge, but do not lose flux out the bottom. Making the adjustment to  $T(R_{\min})$  brings  $\dot{M}$  to within a factor of, on average, 1.5 of the  $\dot{M}$  for the simulation whose base is set deeper in the wind, capturing

ing all relevant photoionization heating, and also results in a similar wind structure.

Despite this, the transition from  $R_{\text{XUV}} > R_{\min}$  to  $R_{\text{XUV}} < R_{\min}$  is likely the source of the sharp transition near  $0.1M_J$  visible in the high flux grids (Fig. 9) and the energy limited mass loss rate comparison plots (Fig. 10a,b). This indicates that while this approximation brings  $\dot{M}$  close to the expected value, it still systematically underestimates it slightly along the line of constant escape velocity that starts at  $0.1M_J$ , though the general trend across the grid still holds. The other consequence of not being able to trace the deposition of the highest few energies of photons is that we compute a lower average heating efficiency than expected if all photons were captured. Thus, we include a warning in model results where  $R_{\text{XUV}} < R_{\min}$ .

The reasons we opt for this simplification rather than raising the pressure of the base boundary for every high escape velocity simulation are twofold. Besides winds being more compressed and launching deeper in their potential wells, another consequence of a small scale height is that a small change in  $R_{\min}$  results in a large change in pressure. This means that, following our prescription for the calculation of lower boundary conditions (Appendix B), raising the pressure of  $R_{\min}$  by, say a factor of 10, results in a very small change in radius (e.g., lowering from  $R_{\min} = 1.04R_P$  to just  $1.03R_P$ ) and an order of magnitude change in  $\rho(R_{\min})$ . Large changes in  $\rho(R_{\min})$  are numerically costly and likely to fail. Too, the resultant change in radius may still not be sufficient to capture the actual photoionization base,  $R_{\text{XUV}}$ . Thus, modeling the lower portion of the upper atmosphere in high escape velocity limit remains an area of ongoing exploration.

## 5.2. Low Escape Velocity Limit

The low escape velocity limit presents its own set of challenges related to the lower boundary of the simulation. For low escape velocity planets, the large scale height means that Wind-AE finds  $R_{\text{XUV}}$  to be extremely high in the atmosphere (up to  $8R_P$  for super-Earths modeled). This elevated  $R_{\text{XUV}}$  occurs regardless of whether the bolometric heating/cooling and molecular layer prescription are turned on. When they are turned on, however, the magnitudes of bolometric heating / cooling terms often naturally decline with radius (i.e., not as a result of the enforced decline of the complementary error function that enforces the molecular to atomic transition) before reaching  $R_{\text{XUV}}$ . This means that there is no longer an isotherm in the molecular region below the wind and the resulting thermal inversion can dip several hundred kelvin below  $T_{\text{skin}}$  (e.g., from

1200 K to 1000 K) (e.g., Fig. 18). While this thermal inversion is neither unphysical nor unexpected, it may require the inclusion of additional physics, making the ability of our model to be easily coupled to more sophisticated lower atmosphere models especially valuable in these cases.

Additionally, in some of the most extreme cases, the sonic point for bolometrically-driven mass loss (i.e., core-powered mass loss or boil off) is of order  $R_{\text{XUV}}$ . This means that XUV photons may not be the predominant driver of the wind and, indeed, they may be absorbed in the supersonic portion of an outflow and be unable to contribute to the heating of the wind because a supersonic flow is not causally connected. This regime is usually referred to as core-powered mass loss or boil off, depending on the point in a planet's evolution that this phenomenon is occurring. Owen & Schlichting (2023) mapped out this parameter space analytically showing that both occur for expected planet properties; however, detailed numerical simulations like ours are required before the combined mass-loss rates are used in evolutionary models. These underdense planets may also be in the regime where Roche-lobe overflow is a significant contributor to mass loss rates (e.g., Erkaev et al. 2007; Jackson et al. 2017).

We find that the outflow structure in low-escape-velocity cases is very sensitive to how the upper atmosphere below the wind is modeled, necessitating more accurate modeling below the wind. This may include more carefully treating the infrared and optical opacities used in the bolometric heating and cooling calculations. It may also include adding molecular line cooling terms, since the low, non-isothermal temperature in region below the wind (Schulik & Booth 2023; Misener et al. 2025), may mean that molecules do not thermally-or photodissociate and are present throughout the region and into the wind.

## 5.3. Additional Physics

Within the molecular layer below the wind, there may be a thin region toward the top of the layer which is still optically thin to heating by the highest energy X-ray photons, but is likely cooled by  $\text{H}_3^+$  molecular line emission (Yelle 2004; García Muñoz 2007). This means that heat deposited by high energy photons in the molecular region below the wind will be largely removed by radiative and/or bolometric cooling, meaning that the contributions of the highest energies X-rays to the outflows may be negligible.

Explicitly modeling the  $\text{H}_3^+$  cooling requires more nuanced and expensive photochemical calculations than are sensible in a relaxation model, but we can approxi-

mate the effects of  $H_{3+}$  cooling by cutting off the high energy end of stellar spectrum at 165 eV and reducing the flux above 70 eV by 70% as found by Frelikh et al. (submitted). The differences in outflow structure and  $\dot{M}$  are negligible for a  $2.02 M_\oplus$ ,  $5.3 R_\oplus$  H-He planet when compared to the same planet irradiated by a full XUV spectrum (13.6-2000 eV) when both planets have fluxes normalized to 13.6-40 eV. Since the highest energy X-rays are already being absorbed below the wind in an H-He atmosphere, they already contribute minimally to the direct heating of the outflow and contribute negligibly to puffing the atmosphere below the wind when compared to the contributions of bolometric heating. So, the absence of the highest energy photons ( $>165$  eV) when “removed” by our pseudo  $H_{3+}$  cooling has minimal impact. For winds containing metals, this choice will be more important.

At the top of the hypothetical X-ray-heated and  $H_{3+}$ -cooled layer, molecules are ultimately thermally dissociated and the outflow is atomic, so we elect to treat the molecular layer holistically as a region with constant mean molecular weight, whose energy budget is predominantly set by bolometric heating and cooling. As we noted in the previous section, though, these assumptions break down for small planets which may have a different thermal or molecular-atomic fraction structure.

#### 5.4. Summary of Comparison to Other Work

To first order, the results of our benchmarking can be broken down as follows. In the high flux limit, differences in the outflow energetics prove important and in the low flux limit, differences in SED shape and lower boundary modeling have the largest impact. The primary source of differences between our model and the high X-ray flux model Owen & Jackson (2012) is our inclusion of Lyman- $\alpha$  and  $PdV$  cooling where the aforementioned model does not. As a result, we find higher mass loss rates for planets with higher escape velocities and lower for lower escape velocities than the high X-ray flux grids in Owen & Jackson (2012).

An advantage of our model is the ability to model both the high (as above) and low incident stellar flux limit with the same physics. In the low flux limit, we explore several case studies. In keeping with previous findings that emphasize the impact of stellar spectra shape, profile differences between our model and García Muñoz (2007) (HD 209458b, H-He), Kubyshkina et al. (2024) (GJ 1214b, H-He), and Caldironi et al. (2022) (HD 209458b, H-He) can be attributed primarily to the differences in the input stellar spectra. Likewise

the good agreement with Salz et al. (2016) (HD 209458b, H) we attribute to the similarities in the spectra.

The other major source of differences is the lower boundary conditions. Our approximation of the region below the wind as molecular and dominated by bolo-metric heating / cooling represents an improvement over models that scale directly from the planetary transit radius and this approximation results in a much higher altitude  $R_{XUV}$  and significantly different outflow profile (Gillet et al. 2023, ,  $0.05 M_J$ ,  $0.55 R_J$ , H-He). However, in comparison to a model with more sophisticated lower atmosphere modeling (Huang et al. 2023, , WASP 121b, metals), we find a much lower  $R_{XUV}$ . Notably, when we match the spectrum and lower boundary conditions to the incredibly comprehensive and more expensive Huang et al. (2023), we are able to closely reproduce their profile and mass loss rates in less than 1/100th of the time.

## 6. SUMMARY

We built upon the 1D photoionization-driven steady-state hydrodynamic transonic Parker wind relaxation code developed by Murray-Clay et al. (2009) by adding metal and X-ray physics, as well as a python wrapper that aids in ramping through the relaxation code solution space, in performing post-facto calculations, in smoothing input stellar spectra, and in visualizing solutions. A fast forward model allows us to perform broad parameter space studies smoothly across such parameters as stellar flux (Figs. 9, 3), planet size (Fig. 8), semi-major axis (Fig. 7), spectral ranges (Figs. 5, 4), presence of metals (Fig. 6), and, in the future, metallicity.

The speed and versatility of Wind-AE allows it to be applied to explore a number of open problems. Wind-AE’s python interface and open-source nature allows it to be easily coupled with chemical network codes that model atmosphere behavior below the optically-thin upper atmosphere and with interior models and XUV spectrum evolution codes in order to model planetary evolution due to atmospheric escape.

<sup>1632</sup> This paper makes use of the following Python libraries:  
<sup>1633</sup> `numpy` (Harris et al. 2020), `matplotlib` (Hunter 2007),  
<sup>1634</sup> and `scipy` (Virtanen et al. 2020).

<sup>1635</sup> MIB, RMC, and JHM acknowledge funding support  
<sup>1636</sup> from NSF CAREER grant 1663706. MIB and RMC  
<sup>1637</sup> acknowledge support from NASA'S Interdisciplinary  
<sup>1638</sup> Consortia for Astrobiology Research (NNH19ZDA001N-  
<sup>1639</sup> ICAR) under grant number 80NSSC21K0597. JEO is  
<sup>1640</sup> supported by a Royal Society University Research Fel-  
<sup>1641</sup> lowship. This project has received funding from the  
<sup>1642</sup> European Research Council (ERC) under the Euro-  
<sup>1643</sup> pean Union's Horizon 2020 research and innovation pro-  
<sup>1644</sup> gramme (Grant agreement No. 853022). We acknowl-  
<sup>1645</sup> edge use of the lux supercomputer at UC Santa Cruz,  
<sup>1646</sup> funded by NSF MRI grant AST 1828315. MIB ac-  
<sup>1647</sup> knowledges the support of the ARCS Foundation and  
<sup>1648</sup> the Cota-Robles Fellowship. We would like to thank  
<sup>1649</sup> Chenliang Huang for sharing data and Jorge Fernandez-  
<sup>1650</sup> Fernandez and Emerson Tao for beta testing `Wind-AE`.

<sup>1651</sup> *Software:* `Wind-AE` available on Github  
<sup>1652</sup> ([github.com/mibroome/wind-ae](https://github.com/mibroome/wind-ae))

## REFERENCES

- <sup>1653</sup> Affolter, L., Mordasini, C., Oza, A. V., Kubyshkina, D., &  
<sup>1654</sup> Fossati, L. 2023, *Astronomy and Astrophysics*, 676,  
<sup>1655</sup> A119, doi: [10.1051/0004-6361/202142205](https://doi.org/10.1051/0004-6361/202142205)
- <sup>1656</sup> Allan, A., & Vidotto, A. A. 2019, *MNRAS*, 490, 3760,  
<sup>1657</sup> doi: [10.1093/mnras/stz2842](https://doi.org/10.1093/mnras/stz2842)
- <sup>1658</sup> Asplund, M., Grevesse, N., Sauval, A. J., & Scott, P. 2009,  
<sup>1659</sup> *ARA&A*, 47, 481,  
<sup>1660</sup> doi: [10.1146/annurev.astro.46.060407.145222](https://doi.org/10.1146/annurev.astro.46.060407.145222)
- <sup>1661</sup> Band, I. M., Trzhaskovskaya, M. B., Verner, D. A., &  
<sup>1662</sup> Iakovlev, D. G. 1990, *A&A*, 237, 267
- <sup>1663</sup> Biassoni, F., Caldiroli, A., Gallo, E., et al. 2024, *A&A*, 682,  
<sup>1664</sup> A115, doi: [10.1051/0004-6361/202347517](https://doi.org/10.1051/0004-6361/202347517)
- <sup>1665</sup> Brackmann, R. T., Fite, W. L., & Neynaber, R. H. 1958,  
<sup>1666</sup> *Physical Review*, 112, 1157,  
<sup>1667</sup> doi: [10.1103/PhysRev.112.1157](https://doi.org/10.1103/PhysRev.112.1157)
- <sup>1668</sup> Caldiroli, A., Haardt, F., Gallo, E., et al. 2022, *A&A*, 663,  
<sup>1669</sup> A122, doi: [10.1051/0004-6361/202142763](https://doi.org/10.1051/0004-6361/202142763)
- <sup>1670</sup> Cecchi-Pestellini, C., Ciaravella, A., & Micela, G. 2006,  
<sup>1671</sup> *A&A*, 458, L13, doi: [10.1051/0004-6361:20066093](https://doi.org/10.1051/0004-6361:20066093)
- <sup>1672</sup> Cecchi-Pestellini, C., Ciaravella, A., & Micela, G. 2006,  
<sup>1673</sup> *Astronomy & Astrophysics*, 458, L13,  
<sup>1674</sup> doi: [10.1051/0004-6361:20066093](https://doi.org/10.1051/0004-6361:20066093)
- <sup>1675</sup> Chadney, J. M., Galand, M., Unruh, Y. C., Koskinen,  
<sup>1676</sup> T. T., & Sanz-Forcada, J. 2015, *Icarus*, 250, 357,  
<sup>1677</sup> doi: [10.1016/j.icarus.2014.12.012](https://doi.org/10.1016/j.icarus.2014.12.012)
- <sup>1678</sup> Chamberlin, P. C., Eparvier, F. G., Knoer, V., et al. 2020,  
<sup>1679</sup> *Space Weather*, 18, e02588,  
<sup>1680</sup> doi: [10.1029/2020SW00258810.1002/essoar.10503732.2](https://doi.org/10.1029/2020SW00258810.1002/essoar.10503732.2)
- <sup>1681</sup> Dalgarno, A., Yan, M., & Liu, W. 1999, *The Astrophysical  
<sup>1682</sup> Journal Supplement Series*, 125, 237, doi: [10.1086/313267](https://doi.org/10.1086/313267)
- <sup>1683</sup> Del Zanna, G., Dere, K. P., Young, P. R., Landi, E., &  
<sup>1684</sup> Mason, H. E. 2015, *A&A*, 582, A56,  
<sup>1685</sup> doi: [10.1051/0004-6361/201526827](https://doi.org/10.1051/0004-6361/201526827)
- <sup>1686</sup> Dere, K. P. 2007, *Astronomy & Astrophysics*, 466, 771,  
<sup>1687</sup> doi: [10.1051/0004-6361:20066728](https://doi.org/10.1051/0004-6361:20066728)
- <sup>1688</sup> Dere, K. P., Landi, E., Mason, H. E., Monsignori Fossi,  
<sup>1689</sup> B. C., & Young, P. R. 1997, *A&AS*, 125, 149,  
<sup>1690</sup> doi: [10.1051/aas:1997368](https://doi.org/10.1051/aas:1997368)
- <sup>1691</sup> Dos Santos, L. A., Alam, M. K., Espinoza, N., &  
<sup>1692</sup> Vissapragada, S. 2023, *AJ*, 165, 244,  
<sup>1693</sup> doi: [10.3847/1538-3881/accf10](https://doi.org/10.3847/1538-3881/accf10)
- <sup>1694</sup> Dos Santos, L. A., Vidotto, A. A., Vissapragada, S., et al.  
<sup>1695</sup> 2022, *A&A*, 659, A62, doi: [10.1051/0004-6361/202142038](https://doi.org/10.1051/0004-6361/202142038)
- <sup>1696</sup> Edwards, B., Changeat, Q., Tsiaras, A., et al. 2023, *AJ*,  
<sup>1697</sup> 166, 158, doi: [10.3847/1538-3881/acea77](https://doi.org/10.3847/1538-3881/acea77)
- <sup>1698</sup> Ehrenreich, D., Bourrier, V., Wheatley, P. J., et al. 2015,  
<sup>1699</sup> *Nature*, 522, 459, doi: [10.1038/nature14501](https://doi.org/10.1038/nature14501)
- <sup>1700</sup> Ercolano, B., & Clarke, C. J. 2010, *MNRAS*, 402, 2735,  
<sup>1701</sup> doi: [10.1111/j.1365-2966.2009.16094.x](https://doi.org/10.1111/j.1365-2966.2009.16094.x)

- 1702 Erkaev, N. V., Kulikov, Y. N., Lammer, H., et al. 2007,  
 1703 A&A, 472, 329, doi: [10.1051/0004-6361:20066929](https://doi.org/10.1051/0004-6361:20066929)
- 1704 Erkaev, N. V., Lammer, H., Odert, P., et al. 2016, Monthly  
 1705 Notices of the Royal Astronomical Society, 460, 1300,  
 1706 doi: [10.1093/mnras/stw935](https://doi.org/10.1093/mnras/stw935)
- 1707 Ferland, G. J., Chatzikos, M., Guzmán, F., et al. 2017,  
 1708 RMxAA, 53, 385, doi: [10.48550/arXiv.1705.10877](https://doi.org/10.48550/arXiv.1705.10877)
- 1709 Fossati, L., Ayres, T. R., Haswell, C. A., et al. 2013a,  
 1710 ApJL, 766, L20, doi: [10.1088/2041-8205/766/2/L20](https://doi.org/10.1088/2041-8205/766/2/L20)
- 1711 —. 2013b, ApJL, 766, L20,  
 1712 doi: [10.1088/2041-8205/766/2/L20](https://doi.org/10.1088/2041-8205/766/2/L20)
- 1713 Friedrich, M. M., Mellema, G., Iliev, I. T., & Shapiro, P. R.  
 1714 2012, MNRAS, 421, 2232,  
 1715 doi: [10.1111/j.1365-2966.2012.20449.x](https://doi.org/10.1111/j.1365-2966.2012.20449.x)
- 1716 García Muñoz, A. 2007, Planetary and Space Science, 55,  
 1717 1426, doi: [10.1016/j.pss.2007.03.007](https://doi.org/10.1016/j.pss.2007.03.007)
- 1718 Gillet, A., Munoz, A. G., & Strugarek, A. 2023,  
 1719 Self-consistent simulation of photoelectrons in exoplanet  
 1720 winds: Faster ionisation and weaker mass loss rates,  
 1721 arXiv. <http://arxiv.org/abs/2309.08390>
- 1722 Guillot, T. 2010, A&A, 520, A27,  
 1723 doi: [10.1051/0004-6361/200913396](https://doi.org/10.1051/0004-6361/200913396)
- 1724 Guo, J. H., & Ben-Jaffel, L. 2016, The Astrophysical  
 1725 Journal, 818, 107, doi: [10.3847/0004-637X/818/2/107](https://doi.org/10.3847/0004-637X/818/2/107)
- 1726 Habing, H. J., & Goldsmith, D. W. 1971, ApJ, 166, 525,  
 1727 doi: [10.1086/150979](https://doi.org/10.1086/150979)
- 1728 Harris, C. R., Millman, K. J., van der Walt, S. J., et al.  
 1729 2020, Nature, 585, 357, doi: [10.1038/s41586-020-2649-2](https://doi.org/10.1038/s41586-020-2649-2)
- 1730 Huang, C., Arras, P., Christie, D., & Li, Z.-Y. 2017, ApJ,  
 1731 851, 150, doi: [10.3847/1538-4357/aa9b32](https://doi.org/10.3847/1538-4357/aa9b32)
- 1732 Huang, C., Koskinen, T., Lavvas, P., & Fossati, L. 2023,  
 1733 The Astrophysical Journal, 951, 123,  
 1734 doi: [10.3847/1538-4357/accd5e](https://doi.org/10.3847/1538-4357/accd5e)
- 1735 Hunten, D. M., Pepin, R. O., & Walker, J. C. G. 1987,  
 1736 Icarus, 69, 532, doi: [10.1016/0019-1035\(87\)90022-4](https://doi.org/10.1016/0019-1035(87)90022-4)
- 1737 Hunter, G., & Kuriyan, M. 1977, Proceedings of the Royal  
 1738 Society of London Series A, 353, 575,  
 1739 doi: [10.1098/rspa.1977.0051](https://doi.org/10.1098/rspa.1977.0051)
- 1740 Hunter, J. D. 2007, Computing in Science & Engineering, 9,  
 1741 90, doi: [10.1109/MCSE.2007.55](https://doi.org/10.1109/MCSE.2007.55)
- 1742 Jackson, A. P., Davis, T. A., & Wheatley, P. J. 2012,  
 1743 Monthly Notices of the Royal Astronomical Society, 422,  
 1744 2024, doi: [10.1111/j.1365-2966.2012.20657.x](https://doi.org/10.1111/j.1365-2966.2012.20657.x)
- 1745 Jackson, B., Arras, P., Penev, K., Peacock, S., & Marchant,  
 1746 P. 2017, ApJ, 835, 145,  
 1747 doi: [10.3847/1538-4357/835/2/145](https://doi.org/10.3847/1538-4357/835/2/145)
- 1748 Kempton, E. M. R., & Knutson, H. A. 2024, Reviews in  
 1749 Mineralogy and Geochemistry, 90, 411,  
 1750 doi: [10.2138/rmg.2024.90.12](https://doi.org/10.2138/rmg.2024.90.12)
- 1751 Kempton, E. M. R., Zhang, M., Bean, J. L., et al. 2023,  
 1752 Nature, 620, 67, doi: [10.1038/s41586-023-06159-5](https://doi.org/10.1038/s41586-023-06159-5)
- 1753 King, G. W., & Wheatley, P. J. 2020, Monthly Notices of  
 1754 the Royal Astronomical Society: Letters, 501, L28,  
 1755 doi: [10.1093/mnrasl/slaa186](https://doi.org/10.1093/mnrasl/slaa186)
- 1756 King, G. W., & Wheatley, P. J. 2021a, MNRAS, 501, L28,  
 1757 doi: [10.1093/mnrasl/slaa186](https://doi.org/10.1093/mnrasl/slaa186)
- 1758 —. 2021b, MNRAS, 501, L28, doi: [10.1093/mnrasl/slaa186](https://doi.org/10.1093/mnrasl/slaa186)
- 1759 Kirk, J., Ahrer, E.-M., Claringbold, A. B., et al. 2025,  
 1760 MNRAS, 537, 3027, doi: [10.1093/mnras/staf208](https://doi.org/10.1093/mnras/staf208)
- 1761 Koskinen, T. T., Harris, M. J., Yelle, R. V., & Lavvas, P.  
 1762 2013, Icarus, 226, 1678, doi: [10.1016/j.icarus.2012.09.027](https://doi.org/10.1016/j.icarus.2012.09.027)
- 1763 Koskinen, T. T., Lavvas, P., Huang, C., et al. 2022, The  
 1764 Astrophysical Journal, 929, 52,  
 1765 doi: [10.3847/1538-4357/ac4f45](https://doi.org/10.3847/1538-4357/ac4f45)
- 1766 Kubyshkina, D., & Fossati, L. 2022, A&A, 668, A178,  
 1767 doi: [10.1051/0004-6361/202244916](https://doi.org/10.1051/0004-6361/202244916)
- 1768 Kubyshkina, D., Fossati, L., & Erkaev, N. V. 2024,  
 1769 Astronomy & Astrophysics, 684, A26,  
 1770 doi: [10.1051/0004-6361/202347837](https://doi.org/10.1051/0004-6361/202347837)
- 1771 Kubyshkina, D., Lendl, M., Fossati, L., et al. 2018a,  
 1772 Astronomy and Astrophysics, 612, A25,  
 1773 doi: [10.1051/0004-6361/201731816](https://doi.org/10.1051/0004-6361/201731816)
- 1774 Kubyshkina, D., Fossati, L., Erkaev, N. V., et al. 2018b,  
 1775 The Astrophysical Journal, 866, L18,  
 1776 doi: [10.3847/2041-8213/aae586](https://doi.org/10.3847/2041-8213/aae586)
- 1777 Kubyshkina, D. I., & Fossati, L. 2021, Research Notes of  
 1778 the American Astronomical Society, 5, 74,  
 1779 doi: [10.3847/2515-5172/abf498](https://doi.org/10.3847/2515-5172/abf498)
- 1780 Lammer, H., Stökl, A., Erkaev, N. V., et al. 2014, Monthly  
 1781 Notices of the Royal Astronomical Society, 439, 3225,  
 1782 doi: [10.1093/mnras/stu085](https://doi.org/10.1093/mnras/stu085)
- 1783 Lecavelier Des Etangs, A., Ehrenreich, D., Vidal-Madjar,  
 1784 A., et al. 2010, A&A, 514, A72,  
 1785 doi: [10.1051/0004-6361/200913347](https://doi.org/10.1051/0004-6361/200913347)
- 1786 Lee, E. J., & Connors, N. J. 2021, ApJ, 908, 32,  
 1787 doi: [10.3847/1538-4357/abd6c7](https://doi.org/10.3847/1538-4357/abd6c7)
- 1788 Linssen, D., Shih, J., MacLeod, M., & Oklopčić, A. 2024,  
 1789 arXiv e-prints, arXiv:2404.12775,  
 1790 doi: [10.48550/arXiv.2404.12775](https://doi.org/10.48550/arXiv.2404.12775)
- 1791 Linssen, D. C., & Oklopčić, A. 2023, A&A, 675, A193,  
 1792 doi: [10.1051/0004-6361/202346583](https://doi.org/10.1051/0004-6361/202346583)
- 1793 Loyd, R. O. P., Schreyer, E., Owen, J. E., et al. 2025,  
 1794 Nature, 638, 636, doi: [10.1038/s41586-024-08490-x](https://doi.org/10.1038/s41586-024-08490-x)
- 1795 Malsky, I., & Rogers, L. A. 2020, The Astrophysical  
 1796 Journal, 896, 48, doi: [10.3847/1538-4357/ab873f](https://doi.org/10.3847/1538-4357/ab873f)
- 1797 McCann, J. 2021, PhD thesis, UC Santa Barbara
- 1798 Mignone, A., Zanni, C., Tzeferacos, P., et al. 2012, The  
 1799 Astrophysical Journal Supplement Series, 198, 7,  
 1800 doi: [10.1088/0067-0049/198/1/7](https://doi.org/10.1088/0067-0049/198/1/7)

- <sup>1801</sup> Misener, W., Schulik, M., Schlichting, H. E., & Owen, J. E.  
<sup>1802</sup> 2025, ApJ, 980, 152, doi: [10.3847/1538-4357/ada777](https://doi.org/10.3847/1538-4357/ada777)
- <sup>1803</sup> Murray-Clay, R. A., Chiang, E. I., & Murray, N. 2009,  
<sup>1804</sup> ApJ, 693, 23, doi: [10.1088/0004-637X/693/1/23](https://doi.org/10.1088/0004-637X/693/1/23)
- <sup>1805</sup> Nortmann, L., Pallé, E., Salz, M., et al. 2018, Science, 362,  
<sup>1806</sup> 1388, doi: [10.1126/science.aat5348](https://doi.org/10.1126/science.aat5348)
- <sup>1807</sup> Osterbrock, D. E., & Ferland, G. J. 2006, Astrophysics of  
<sup>1808</sup> gaseous nebulae and active galactic nuclei (University  
<sup>1809</sup> Science Books)
- <sup>1810</sup> Owen, J. E. 2019, Annual Review of Earth and Planetary  
<sup>1811</sup> Sciences, 47, 67,  
<sup>1812</sup> doi: [10.1146/annurev-earth-053018-060246](https://doi.org/10.1146/annurev-earth-053018-060246)
- <sup>1813</sup> Owen, J. E., & Alvarez, M. A. 2016, ApJ, 816, 34,  
<sup>1814</sup> doi: [10.3847/0004-637X/816/1/34](https://doi.org/10.3847/0004-637X/816/1/34)
- <sup>1815</sup> Owen, J. E., & Jackson, A. P. 2012, Monthly Notices of the  
<sup>1816</sup> Royal Astronomical Society, 425, 2931,  
<sup>1817</sup> doi: [10.1111/j.1365-2966.2012.21481.x](https://doi.org/10.1111/j.1365-2966.2012.21481.x)
- <sup>1818</sup> Owen, J. E., & Schlichting, H. E. 2023, MNRAS,  
<sup>1819</sup> doi: [10.1093/mnras/stad3972](https://doi.org/10.1093/mnras/stad3972)
- <sup>1820</sup> Owen, J. E., & Wu, Y. 2016, The Astrophysical Journal,  
<sup>1821</sup> 817, 107, doi: [10.3847/0004-637X/817/2/107](https://doi.org/10.3847/0004-637X/817/2/107)
- <sup>1822</sup> Owen, J. E., & Wu, Y. 2017, ApJ, 847, 29,  
<sup>1823</sup> doi: [10.3847/1538-4357/aa890a](https://doi.org/10.3847/1538-4357/aa890a)
- <sup>1824</sup> Pai Asnodkar, A., Wang, J., Broome, M., et al. 2024,  
<sup>1825</sup> Monthly Notices of the Royal Astronomical Society, 535,  
<sup>1826</sup> 1829, doi: [10.1093/mnras/stae2441](https://doi.org/10.1093/mnras/stae2441)
- <sup>1827</sup> Parmentier, V., & Guillot, T. 2014, A&A, 562, A133,  
<sup>1828</sup> doi: [10.1051/0004-6361/201322342](https://doi.org/10.1051/0004-6361/201322342)
- <sup>1829</sup> Parmentier, V., Guillot, T., Fortney, J. J., & Marley, M. S.  
<sup>1830</sup> 2015, A&A, 574, A35, doi: [10.1051/0004-6361/201323127](https://doi.org/10.1051/0004-6361/201323127)
- <sup>1831</sup> Penzlin, A. B. T., Booth, R. A., Kirk, J., et al. 2024,  
<sup>1832</sup> MNRAS, 535, 171, doi: [10.1093/mnras/stae2362](https://doi.org/10.1093/mnras/stae2362)
- <sup>1833</sup> Poppenhaeger, K., Ketzer, L., & Mallonn, M. 2021,  
<sup>1834</sup> MNRAS, 500, 4560, doi: [10.1093/mnras/staa1462](https://doi.org/10.1093/mnras/staa1462)
- <sup>1835</sup> Press, W. H., Teukolsky, S. A., Vetterling, W. T., &  
<sup>1836</sup> Flannery, B. P. 1992, Numerical recipes in C. The art of  
<sup>1837</sup> scientific computing
- <sup>1838</sup> Richards, P. G., Fennelly, J. A., & Torr, D. G. 1994,  
<sup>1839</sup> J. Geophys. Res., 99, 8981, doi: [10.1029/94JA00518](https://doi.org/10.1029/94JA00518)
- <sup>1840</sup> Rogers, J. G., Gupta, A., Owen, J. E., & Schlichting, H. E.  
<sup>1841</sup> 2021, MNRAS, 508, 5886, doi: [10.1093/mnras/stab2897](https://doi.org/10.1093/mnras/stab2897)
- <sup>1842</sup> Rogers, J. G., Owen, J. E., & Schlichting, H. E. 2024,  
<sup>1843</sup> MNRAS, 529, 2716, doi: [10.1093/mnras/stae563](https://doi.org/10.1093/mnras/stae563)
- <sup>1844</sup> Salz, M., Banerjee, R., Mignone, A., et al. 2015, Astronomy  
<sup>1845</sup> and Astrophysics, 576, A21,  
<sup>1846</sup> doi: [10.1051/0004-6361/201424330](https://doi.org/10.1051/0004-6361/201424330)
- <sup>1847</sup> Salz, M., Czesla, S., Schneider, P. C., & Schmitt, J. H.  
<sup>1848</sup> M. M. 2016, Astronomy and Astrophysics, 586, A75,  
<sup>1849</sup> doi: [10.1051/0004-6361/201526109](https://doi.org/10.1051/0004-6361/201526109)
- <sup>1850</sup> Schreyer, E., Owen, J. E., Loyd, R. O. P., & Murray-Clay,  
<sup>1851</sup> R. 2024, MNRAS, 533, 3296,  
<sup>1852</sup> doi: [10.1093/mnras/stae1976](https://doi.org/10.1093/mnras/stae1976)
- <sup>1853</sup> Schulik, M., & Booth, R. A. 2023, MNRAS, 523, 286,  
<sup>1854</sup> doi: [10.1093/mnras/stad1251](https://doi.org/10.1093/mnras/stad1251)
- <sup>1855</sup> Schulik, M., & Owen, J. 2024, arXiv e-prints,  
<sup>1856</sup> arXiv:2412.05258, doi: [10.48550/arXiv.2412.05258](https://doi.org/10.48550/arXiv.2412.05258)
- <sup>1857</sup> Shull, J. M., & van Steenberg, M. E. 1985, ApJ, 298, 268,  
<sup>1858</sup> doi: [10.1086/163605](https://doi.org/10.1086/163605)
- <sup>1859</sup> Spake, J. J., Sing, D. K., Evans, T. M., et al. 2018, Nature,  
<sup>1860</sup> 557, 68, doi: [10.1038/s41586-018-0067-5](https://doi.org/10.1038/s41586-018-0067-5)
- <sup>1861</sup> Spinelli, R., Gallo, E., Haardt, F., et al. 2023, AJ, 165, 200,  
<sup>1862</sup> doi: [10.3847/1538-3881/acc336](https://doi.org/10.3847/1538-3881/acc336)
- <sup>1863</sup> Tang, Y., Fortney, J. J., & Murray-Clay, R. 2024, ApJ,  
<sup>1864</sup> 976, 221, doi: [10.3847/1538-4357/ad8567](https://doi.org/10.3847/1538-4357/ad8567)
- <sup>1865</sup> Thorngren, D. P., Fortney, J. J., Murray-Clay, R. A., &  
<sup>1866</sup> Lopez, E. D. 2016, The Astrophysical Journal, 831, 64,  
<sup>1867</sup> doi: [10.3847/0004-637X/831/1/64](https://doi.org/10.3847/0004-637X/831/1/64)
- <sup>1868</sup> Tian, F., Toon, O. B., Pavlov, A. A., & De Sterck, H. 2005,  
<sup>1869</sup> ApJ, 621, 1049, doi: [10.1086/427204](https://doi.org/10.1086/427204)
- <sup>1870</sup> Verner, D. A., & Ferland, G. J. 1996, ApJS, 103, 467,  
<sup>1871</sup> doi: [10.1086/192284](https://doi.org/10.1086/192284)
- <sup>1872</sup> Vidal-Madjar, A., Lecavelier des Etangs, A., Désert, J. M.,  
<sup>1873</sup> et al. 2003, Nature, 422, 143, doi: [10.1038/nature01448](https://doi.org/10.1038/nature01448)
- <sup>1874</sup> Virtanen, P., Gommers, R., Oliphant, T. E., et al. 2020,  
<sup>1875</sup> Nature Methods, 17, 261, doi: [10.1038/s41592-019-0686-2](https://doi.org/10.1038/s41592-019-0686-2)
- <sup>1876</sup> Yan, D., Seon, K.-i., Guo, J., Chen, G., & Li, L. 2022, ApJ,  
<sup>1877</sup> 936, 177, doi: [10.3847/1538-4357/ac8793](https://doi.org/10.3847/1538-4357/ac8793)
- <sup>1878</sup> Yelle, R. V. 2004, Icarus, 170, 167,  
<sup>1879</sup> doi: [10.1016/j.icarus.2004.02.008](https://doi.org/10.1016/j.icarus.2004.02.008)
- <sup>1880</sup> Yoshida, T., Terada, N., Ikoma, M., & Kuramoto, K. 2022,  
<sup>1881</sup> ApJ, 934, 137, doi: [10.3847/1538-4357/ac7be7](https://doi.org/10.3847/1538-4357/ac7be7)
- <sup>1882</sup> Yoshida, T., Terada, N., & Kuramoto, K. 2024, Progress in  
<sup>1883</sup> Earth and Planetary Science, 11, 59,  
<sup>1884</sup> doi: [10.1186/s40645-024-00666-3](https://doi.org/10.1186/s40645-024-00666-3)
- <sup>1885</sup> Zhang, M., Knutson, H. A., Dai, F., et al. 2023, AJ, 165,  
<sup>1886</sup> 62, doi: [10.3847/1538-3881/aca75b](https://doi.org/10.3847/1538-3881/aca75b)

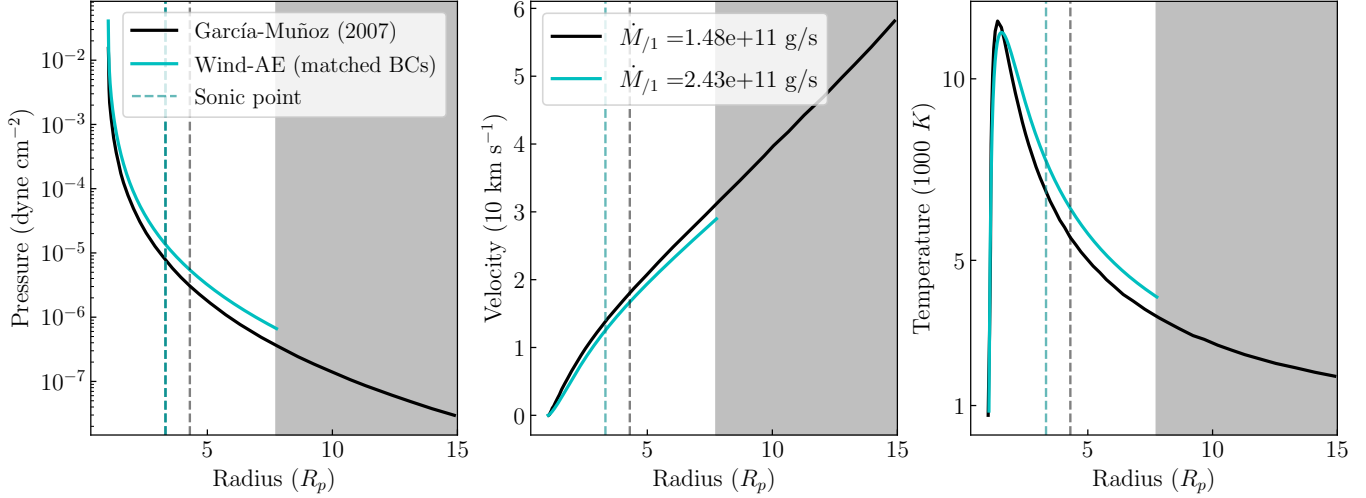


**Figure 11. HD 209458b Pure-H García Muñoz (2007)**- We reproduce the SP solution of García Muñoz (2007) Figs. 3-4 for an EUV-irradiated pure-H atmosphere (black). Wind-AE solution plotted (cyan) is for a pure-H atmosphere with no Lyman- $\alpha$  cooling, a similar if not identical high activity solar spectrum ( $F_{\text{tot}} = 2474 \text{ ergs s}^{-1} \text{ cm}^{-2}$  integrated over 13.6-165 eV, which loosely simulates H3+ cooling), and BCs matched to those of the black solution ( $R_{\min}=1.03 R_p$ ,  $T=730 \text{ K}$ ,  $\rho=5.82 \times 10^{-13} \text{ g cm}^{-3}$ ). Sonic points are dashed lines and the solid gray is the Coriolis radius past which our model is not valid.

1887

## APPENDIX

1888

### A. COMPARISONS TO EXISTING RESULTS

1889 Here we benchmark our model against a selection of the other numerical models in the literature. For all of the  
 1890 comparisons herein we continue to use a scaled solar spectrum from a low activity period of the Sun and use the  
 1891 physical boundary conditions for the outflow discussed in §2 unless otherwise specified. It is important to note that  
 1892 a number of models use different geometric surface averaging schemes for the mass loss rate, so instead of reporting  
 1893  $\dot{M} = 0.3 \cdot 4\pi R_{\text{sp}}^2 \rho(R_{\text{sp}}) v(R_{\text{sp}})$  as in main body of the text, here we report  $\dot{M}_f = \dot{M}/f = 4\pi R_{\text{sp}}^2 \rho(R_{\text{sp}}) v(R_{\text{sp}})/f$  where  
 1894  $f$  is a factor between 1 and 4. This allows us to make direct comparisons to mass loss rates found in models in the  
 1895 literature that use different geometric averaging factors. We consider the mass loss rates to be in agreement if they  
 1896 fall within 30% of each other.

1897 One of the advantages of Wind-AE's relative speed is that we are able to reproduce the results of more expensive  
 1898 models including those coupled with full photochemical lower atmosphere models. García Muñoz (2007) is one such  
 1899 well-known model. García Muñoz (2007) is a 1D multi-frequency EUV hydrodynamic model that uses a photochemical  
 1900 network to model photoionization of hydrogen down to  $r = R_p$  and includes conductive and H3+ cooling, but not  
 1901 Lyman- $\alpha$  cooling. For a pure-H HD 209458b, we find good agreement in the outflow structure and mass loss rate (Fig.  
 1902 11) when we employ the same high activity EUV solar spectrum used by García Muñoz (2007) (Richards et al. 1994),  
 1903 turn off Ly- $\alpha$  line cooling, and match lower boundary conditions (Fig. 11). We normalize the spectrum to  $F_{\text{tot}} = 2474$   
 1904  $\text{ergs s}^{-1} \text{ cm}^{-2}$  over the range of 12-165 eV, where the upper bound is chosen to simulate the effect of H3+ cooling which  
 1905 radiates away the highest energy photons.

1906 Notably, we get relatively poor agreement with the same flux, same wavelength range, but different solar spectrum  
 1907 (the lower activity FISM2 spectrum used in the main body of the text). This is consistent with the findings of, e.g.,  
 1908 Guo & Ben-Jaffel (2016); Kubyshkina et al. (2024); Schulik & Owen (2024), who report that SED shape can have a  
 1909 significant influence on the outflow physics. In particular, we find that a higher flux or different SED shape in low  
 1910 energy (<60 eV) EUV photons, results in a shallower temperature gradient and warmer outflow at high radii. This  
 1911 appears to be the result of a larger flux of low energy photons being absorbed at  $\tau(\text{EUV}) = 1$  surfaces at high fluxes.

1912 We also benchmark against other relatively fast and simple 1D substellar models such as Caldrioli et al. (2022)  
 1913 (ATES). ATES is a 1D multi-frequency XUV H-He steady-state Godunov-type hydrodynamic code. ATES models  
 1914 the similar ionization and heating/heating sources to Wind-AE, but ATES also includes free-free and collisional heat-

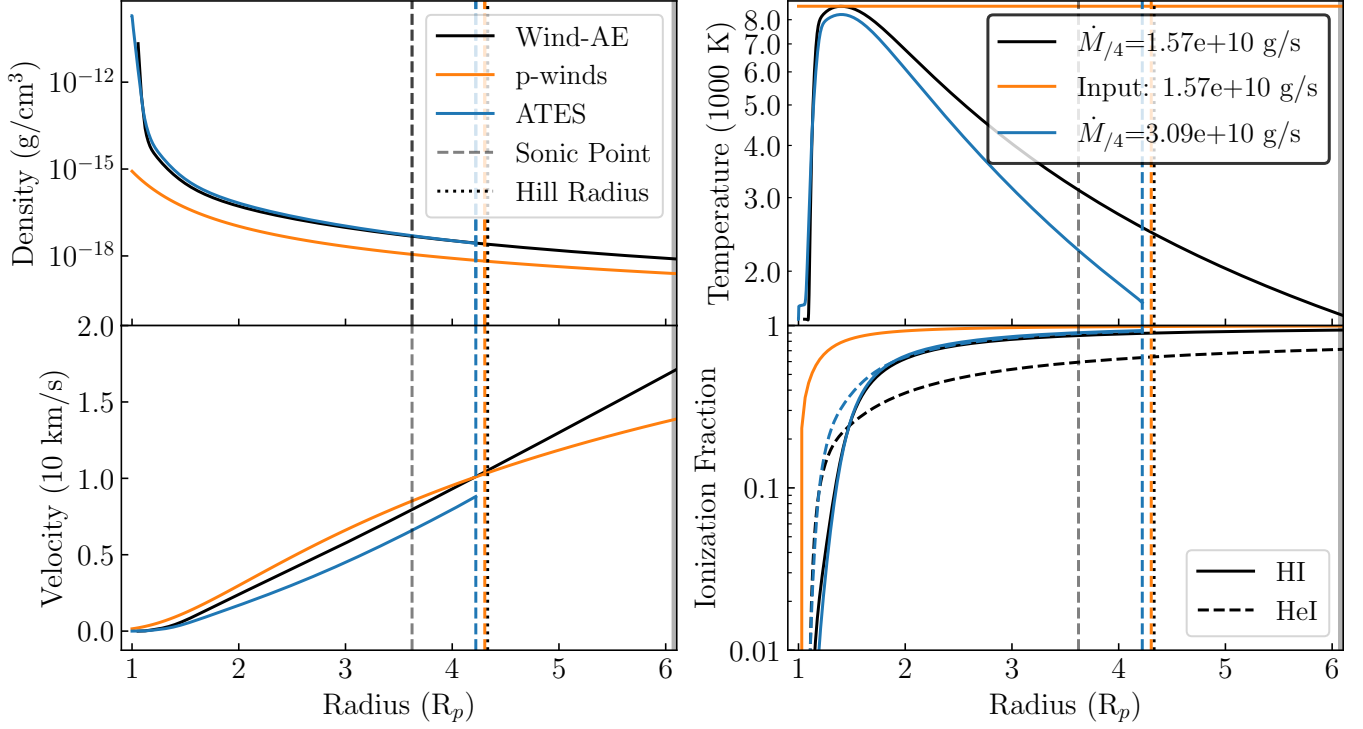


**Figure 12. HD 209458b H-He comparisons with ATES and p-winds** - Wind-AE H-He (black), ATES H-He (blue, Caldiroli et al. 2022), and p-winds pure-H (orange, Dos Santos et al. 2022) profiles for HD209458b. Inputs to p-winds are  $T = 8616$  and  $\dot{M} = 1.57 \times 10^{10} \text{ g s}^{-1}$  (the  $\dot{M}_{\text{4}}$  computed by Wind-AE). Sonic points are plotted as dashed vertical lines and the Hill radius as dotted vertical. All three employ different approximations to solar spectra.

ing/cooling and does not include secondary ionizations (all of which are negligible for HD 209458b with an H-He atmosphere (Murray-Clay et al. 2009)). ATES includes advection in post-processing, which limits the accuracy of ionization profiles for low flux planets, but still produces accurate outflow rates. The post processing step also currently requires manual intervention, resulting in a slightly longer runtime than our model.

For the comparison in Fig. 12, we run ATES for HD 209458b and set the ATES boundary conditions to match the physical BCs computed for the base of the simulation by Wind-AE:  $\log_{10}(n_0) = 13.04$ ,  $T_{\text{eq}} = 1535 \text{ K}$ , and H/He number ratio = 0.0629. ATES employs a powerlaw estimate for the stellar SED (Caldiroli et al. 2022), so to match the total flux and the ratio of X-ray to EUV flux, we set the log X-ray luminosity in ATES to 26.89 and log EUV luminosity to 27.8. This difference in SED is the source of the steeper temperature gradient at higher radii and the lower velocity in the ATES profile. The two models are otherwise in good agreement and ATES takes a similar amount of CPU time, but longer wall time, to run.

We also compare to Dos Santos et al. (2022)'s p-winds, a 1D multi-frequency steady-state XUV isothermal Parker wind backwards model with multispecies capabilities including line cooling, but not including the X-ray physics detailed in §2.4. Because p-winds is isothermal it is incredibly computationally inexpensive, but not a comparable model to the non-isothermal ones listed in this section. We set the input  $\dot{M}$  to p-winds equal to the  $\dot{M}_{\text{3}} = 2.1 \times 10^{10} \text{ g s}^{-1}$  computed by Wind-AE and the input isothermal temperature equal to the temperature at the peak of Wind-AE's temperature profile ( $T=8616 \text{ K}$ ). p-winds does not converge for isothermal temperature equal to the average temperature ( $T=3561 \text{ K}$ ) of our model. For the p-winds solution, we employ p-winds's default solar spectrum without any modifications, meaning that integrated flux over 13.6-2000 eV is  $F_{\text{tot}} = 1342 \text{ ergs s}^{-1} \text{ cm}^{-2}$  vs. the  $F_{\text{tot}} = 1095 \text{ ergs s}^{-1} \text{ cm}^{-2}$  in Wind-AE. The results for an H-He atmosphere (0.8:0.2 mass fraction, 0.94:0.6 number fraction) are shown in Figure 12. Depending on how close in parameter space Wind-AE's initial guess is and the number of metals present in the wind, p-winds either runs in similar time or is up to 1000 times faster.

ATES, p-winds, and Wind-AE all make simplifying assumptions to avoid the expense of non-LTE photochemical computation; however, several 1D models employ the 1D multispecies photoionization solver CLOUDY (Ferland et al.

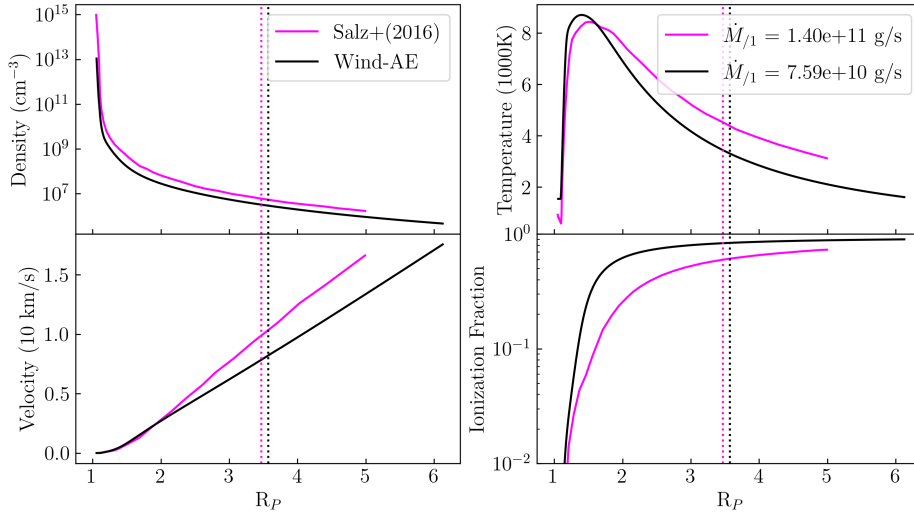


**Figure 13. Pure-H HD 209458b TPCI Model** - Salz et al. (2016) (TPCI, magenta) has lower BCs of  $T(R_{\min}) = 1000\text{K}$ ,  $R_{\min} \sim 1.05R_P$ ,  $\rho(R_{\min}) \sim 1.6 \times 10^{-9}\text{g cm}^{-3}$ . We have confirmed that these boundary conditions are not the source of the profile differences.

1939 to handle the gas microphysics and photochemistry within the outflow and/or below the wind. Linssen et al.  
 1940 (2024) (Sunbather) integrates CLOUDY and p-winds, Kubyshkina et al. (2024) (CHAIN) integrates CLOUDY and  
 1941 Kubyshkina et al. (2018a), and Salz et al. (2016) (TPCI) integrates CLOUDY and the 3D MHD model PLUTO  
 1942 (Mignone et al. 2012). We compare to the GJ 1214b outflow profiles from Kubyshkina et al. (2024) for the latter  
 1943 two here. TPCI is the PLUTO-CLOUDY interface, a steady-state 1D multi-frequency XUV, multispecies solver and  
 1944 contains the same ionization and heating/cooling terms as Wind-AE and also free-free, conductive, and collisional  
 1945 heating/cooling (which are negligible for GJ 1214b). We find very good agreement in outflow profiles for HD 209458b  
 1946 with a pure-H atmosphere (Fig. 13) with 1D structure differences likely stemming from differences in the Lisird low  
 1947 activity sun spectrum used (Salz et al. 2016). As in Wind-AE, TPCI is able to self-consistently compute the heating  
 1948 efficiency.

1949 CHAIN contains the same ionization and heating sources as TPCI, and additionally includes  $\text{H}_3^+$  cooling and sec-  
 1950 ondary ionizations through CLOUDY (Kubyshkina et al. 2024). We model GJ 1214b with the parameters listed in  
 1951 Table 1 of Kubyshkina et al. (2024) and with the scaled solar spectrum with integrated flux  $F_{\text{tot}} = 886 \text{ ergs s}^{-1} \text{ cm}^{-2}$   
 1952 for the range 13.6-2000eV (Fig. 14). Kubyshkina et al. (2024) attribute the differences from TPCI in the GJ 1214b  
 1953 outflow profiles to differences in the stellar spectra that each model used, resulting in different heating in the lower  
 1954 atmosphere. Despite significant temperature profile differences likely stemming from SED differences, we find good  
 1955 agreement with  $\dot{M}/_1 = 1.58 \times 10^{11} \text{ g/s}$ . We confirm that lower boundary condition differences are not the source of  
 1956 structure differences for both TPCI and CHAIN. This is consistent with our findings for other low flux hot Jupiters.

1957 Our lower boundary conditions do turn out to make a significant impact on the profile of WASP-121 b when compared  
 1958 with Huang et al. (2023) (Fig. 14). This model uses the Koskinen et al. (2022) atmospheric escape model (an update of  
 1959 Koskinen et al. (2013)) with a photochemical hydrostatic model 100 bar and 1  $\mu\text{bar}$ , where the escape model takes over.  
 1960 This model is extremely comprehensive and includes diffusion, drag, charge exchange, thermal ionizations, and variety  
 1961 of other nuanced physics calculations which our model does not include. When we use the bolometric heating/cooling  
 1962 and molecular layer to compute the lower boundary conditions as in the main body of this text, Wind-AE produces  
 1963 the lime green profile and  $\dot{M}/_4 = 8.45 \times 10^{11} \text{ g s}^{-1}$  in Figure 15 for an atmosphere that consists of H I, He I, C I, N I,  
 1964 O I, S I, Mg II, Si II, Ca II, and Fe II. To eliminate spectral differences as the source of any discrepancies, we use the  
 1965 same spectrum as Huang et al. (2023).

1966 Notably, when we manually set our lower boundary conditions to match Case B of Huang et al. (2023) (H I, He  
 1967 I, C I, N I, O I, S I, Mg II, Si II, Ca II, Fe II, K I, and Na I), we are able to compute a profile and mass loss rate

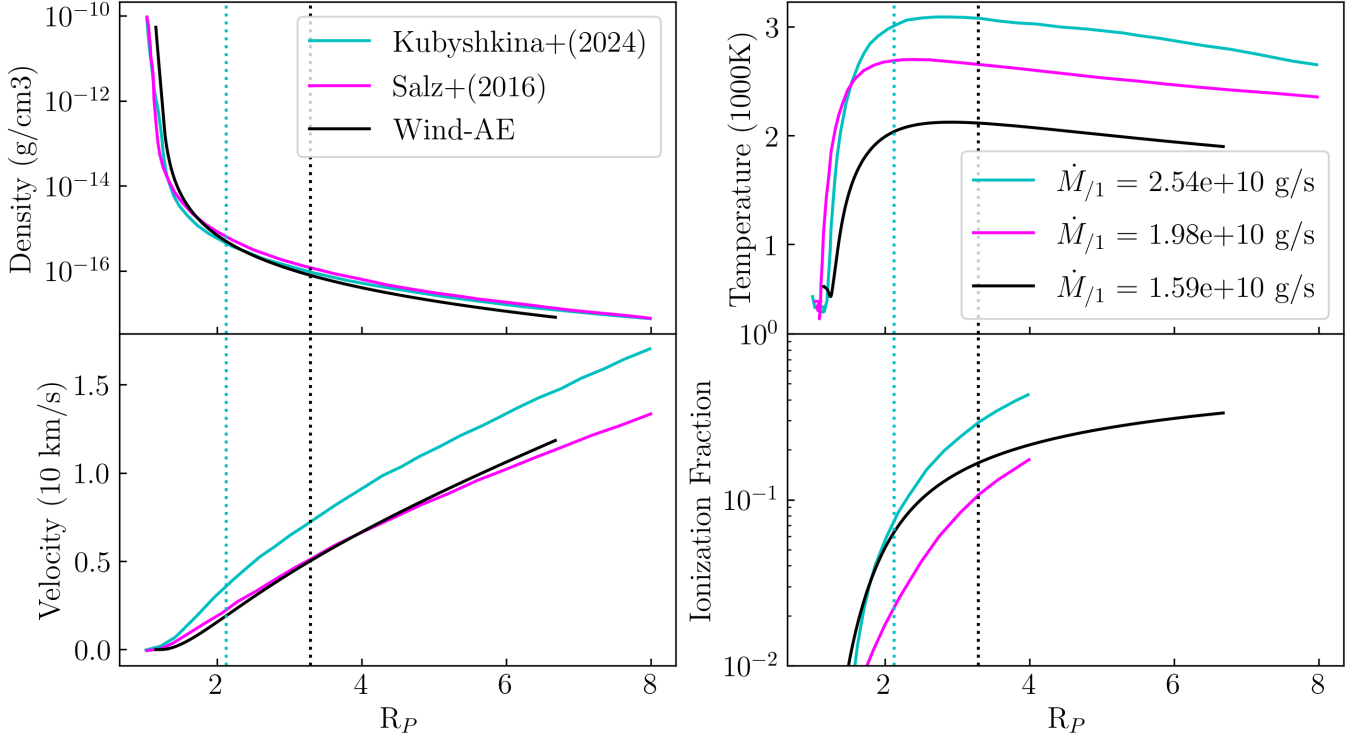


**Figure 14. H-He GJ 1214b CHAIN and TPCI Models** - GJ 1214b:  $6.36 M_\oplus$ ,  $2.69 R_\oplus$ ,  $0.014 \text{ au}$ ,  $0.18 M_\odot$ ,  $3.51 \times 10^{-3} L_\odot$ ,  $886 \text{ ergs s}^{-1} \text{ cm}^{-2}$ . Kubyshkina & Fossati (2022) CHAIN solar spectrum solution (cyan) and Salz et al. (2016) TPCI solution (magenta) are reproduced here.

( $\dot{M}_{168} = 1.3 \times 10^{12} \text{ g s}^{-1}$ ) similar to that found by Huang et al. (2023) ( $\dot{M}_{169} = 3.7 \times 10^{12} \text{ g s}^{-1}$ ) in less than 1/100th of the computational time.

HD 209458b and GJ 1214b are old, low-flux planets whose mass loss is in the energy-limited regime and dominated by EUV flux, with the presence of X-rays having relatively little effect on pure-H and H-He atmospheres. Outflows in the high flux limit, on the other hand are considered recombination limited, young stars exhibit a higher proportion of higher X-ray flux relative to the bolometric and EUV flux, and Lyman- $\alpha$  cooling becomes more significant. To test our model in the high flux limit we compare to two high XUV flux models, the first of which is Owen & Jackson (2012).

We model a H-He atmosphere for a  $1.72 R_J$ ,  $1 M_J$  and a  $5 R_J$ ,  $1 M_J$  planet at 0.1 au around solar-type star with X-ray luminosity of  $10^{30} \text{ ergs s}^{-1}$  to compare outflow profiles with those in Owen & Jackson (2012) Figure 4. We scale our solar spectrum such that the flux in the X-ray between 100 eV and 2000 eV corresponds to  $L_X = 10^{30} \text{ ergs s}^{-1}$ . The net EUV flux between 13.6-2000 eV is then  $F_{\text{tot}} = 3.57 \times 10^5 \text{ ergs s}^{-1} \text{ cm}^{-2}$ . Owen & Jackson (2012) make simplifying assumption that the outflow is in ionization equilibrium, which is valid in the high XUV flux limit where the outflow is “recombination limited”. As a result, the Owen & Jackson (2012) analytic solution is not frequency dependent, making our choice of a scaled modern-day solar spectrum adequate for the purposes of comparing—though attempts to model a planet around a young XUV active star should take into account the higher ratio of X-ray flux to EUV flux for younger stars.

With the inclusion of Lyman- $\alpha$  cooling, PdV cooling, and solving the ionization balance equation, we find that the outflow is much cooler at high altitudes and stays much denser throughout (Fig. 16). Even when we remove the bolometrically-heated/cooled molecular layer and match the lower boundary temperature and density of Owen & Jackson (2012) these features remain. As a result, we predict higher geometrically averaged mass loss rates ( $\dot{M}_{198}$ ) for planets with higher escape velocities and lower mass loss rates for lower escape velocities than predicted in the Owen & Jackson (2012) mass loss grid (Fig. 17).

Fig. 18 provides a further illustration of the importance of the lower boundary conditions in determining outflow structure. We match the outflow structure of a low escape velocity planet modeled by Gillet et al. (2023) (black) when we match their boundary conditions (yellow). However, when we take into account bolometric heating and

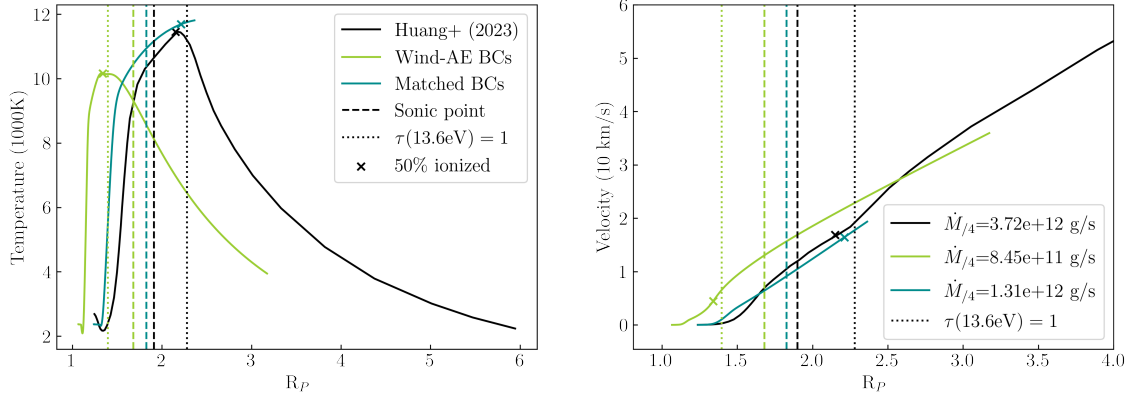


**Figure 15.** Metals WASP-121 b ([Huang et al. \(2023\)](#)) - WASP 121b:  $1.18 M_J$ ,  $1.77 R_J$ ,  $0.03 \text{ au}$ ,  $1.35 M_\odot$ ,  $2.6 L_\odot$ ,  $F_{\text{tot}} = 6.66 \times 10^4 \text{ ergs s}^{-1} \text{ cm}^{-2}$ . Case B ([Huang et al. \(2023\)](#), Fig. 20) with solar abundances of H I, He I, C I, N I, O I, S I, Mg II, Si II, Ca II, Fe II, K I, and Na I is reproduced in black. Wind-AE models for solar abundances of all of the above species except Fe II, K I, and Na I using our lower BCs (green) and matching BCs (blue) of  $R_{\min} = 1.24$  and  $\rho(R_{\min}) = 1.39 \times 10^{-11} \text{ g cm}^{-3}$ . Both have the same input stellar spectrum as black.

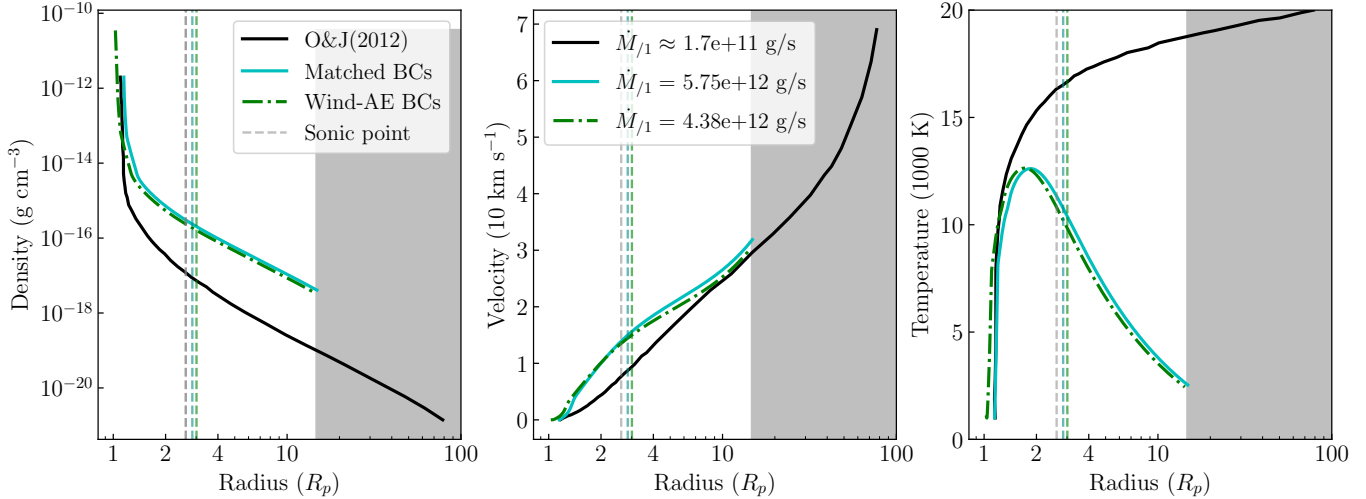


**Figure 16. Profiles for Planets in the High X-ray Flux Limit** - Reproduction of [Owen & Jackson \(2012\)](#) Fig. 4 (black), a model that does not contain PdV or Ly- $\alpha$  cooling. Density, velocity, and temperature results are given for a  $1 M_J$ ,  $1.73 R_J$  (dark) and  $5 R_J$  (light) planet at  $0.1 \text{ au}$  irradiated by a  $1 M_\odot$  star with X-ray luminosity  $L_X = 10^{30} \text{ ergs s}^{-1} \text{ cm}^{-2}$ . Wind-AE profiles are plotted for planets with physical BCs (green) and BCs that match those of the black (cyan). To match  $L_X = 10^{30} \text{ ergs cm}^{-2}$ , our planets are irradiated by a scaled solar spectrum of total flux 13.6-2000 eV of  $3.57 \times 10^5 \text{ ergs s}^{-1} \text{ cm}^{-2}$ . Sonic points are plotted as dashed vertical lines.

cooling, the planet is significantly inflated, generating a very different outflow structure. Relative to results that do not employ lower atmosphere models, our boundary condition implementation finds significantly higher  $R_{\text{XUV}}$  for low-escape-velocity planets (Fig. 18). Notably, Wind-AE consistently finds the sonic point outside of the hill radius for low escape velocity planet such as this one, the physicality of which is still being investigated (Fig. 18).

The lower atmospheric model included in [Huang et al. \(2023\)](#) is more sophisticated than that used by default in Wind-AE. The fact that Wind-AE provides an excellent match to this work's outflow structure if and only if the lower boundary conditions are matched (Fig. 15) indicates that modeling the region below the wind as a simple energetic balance between bolometric heating and cooling with a fixed mean molecular weight has the potential to underestimate the microbar radius and thereby the wind launch radius ( $R_{\text{XUV}}$ ). Fortunately, Wind-AE can be easily coupled to lower atmosphere models whose outputs of radius, density, temperature, metal abundances, ionization fractions, mean

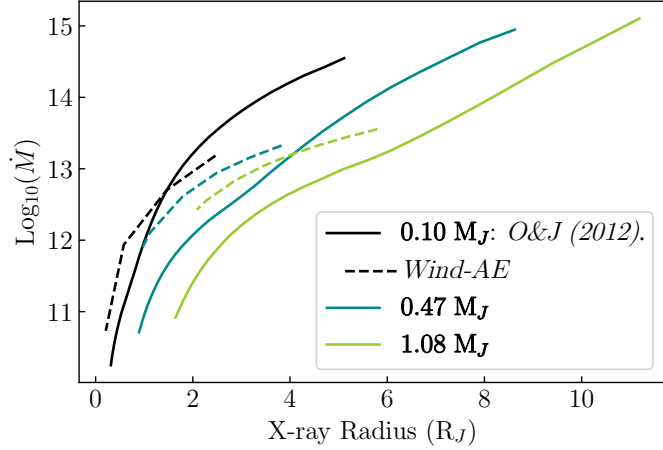


**Figure 17.** Owen & Jackson (2012) Mass Loss Grid - Solid lines are slices at  $0.1 M_J$  (black),  $0.47 M_J$  (dark cyan), and  $1.08 M_J$  (green) through the mass loss grid for planets at  $0.1 \text{ au}$  irradiated by a  $1 M_\odot$  star with  $X\text{-ray luminosity } L_X = 10^{30} \text{ ergs cm}^{-2}$  from Owen & Jackson (2012) Figure 5. Note that the radii in that figure are not optical transit radii, but the approximate  $\tau(1 \text{ keV})= 1$  radius. So we plot the log of geometrically-averaged  $\dot{M}_{/3}$  in  $\text{g s}^{-1}$  as a function of  $\tau(1 \text{ keV})= 1$  for planets of the same masses (dashed). The dashed solutions do not extend to higher  $X\text{-ray radii}$  because planets with higher  $R_P$ 's enter the low escape velocity regime in which the relaxation code is currently not well characterized (see §5.2).

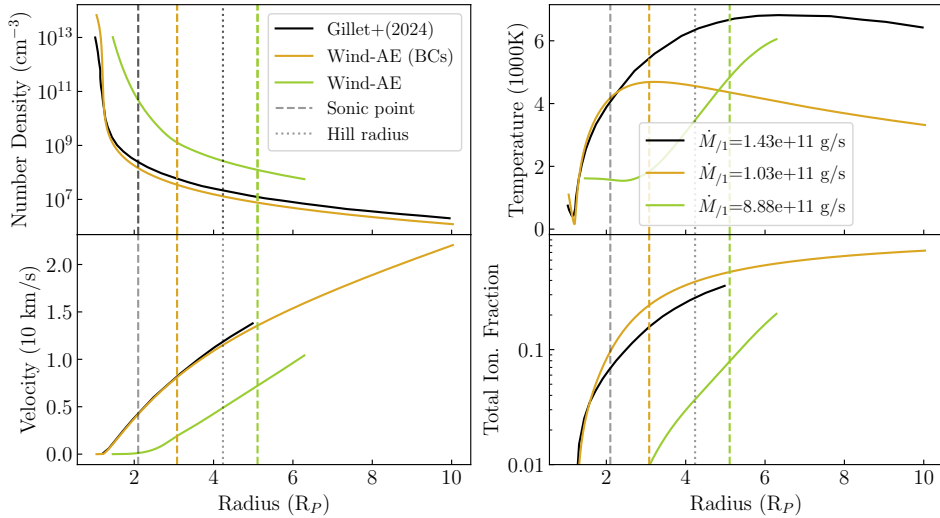


**Figure 18.** Gillet et al. (2024) Secondary Ionization Profiles - We reproduce profiles from Gillet et al. (2023) Fig. 7 for a  $0.05 M_J$ ,  $0.55 R_J$  planet at  $0.045 \text{ au}$  around a solar-type star for a pure-H outflow modeled using PLUTO with secondary ionizations enabled (blue). Wind-AE profile for the same planet with the same solar spectrum, but with bolometric heating and cooling and  $\mu = 2.3 m_H$  for  $r < R_{\text{XUV}}$  enabled (green) and without (yellow). Gray boundary conditions at  $R_{\min}=1.1 R_P$  are matched to blue ( $T=1100\text{K}$ ,  $\rho=1.326 \times 10^{-10} \text{ g/s}$ ,  $P=12 \mu\text{bar}$ ).

2003 molecular weight, etc., can be easily fed as inputs into Wind-AE. The default lower-atmosphere model in Wind-AE is  
2004 nevertheless an improvement over setting boundary conditions at a fixed multiple of the optical transit radius and is  
2005 valuable for increasing accuracy of  $R_{\text{XUV}}$  when more sophisticated lower-atmospheric modeling is not available.

2006

## B. BOUNDARY CONDITIONS

2007 The upper boundary condition, the sonic point,  $R_{\text{sp}}$ , is where  $v(R_{\text{sp}}) = c_s(R_{\text{sp}})$ . This is a natural critical point  
2008 that emerges from the transonic Parker Wind solution (see Murray-Clay et al. (2009) Equations 15-16). Though the  
2009 molecular layer below  $\sim 10^{-9}$  bar is optically thick to most XUV radiation, it can still be heated by the bolometric  
2010 flux from the star, which peaks in the optical. The bolometric heating and cooling naturally enforce an isotherm at the

skin temperature below the wind (we do not model molecular line cooling by, e.g.,  $H_{3+}$ ). The balance of bolometric heating and cooling allows us to analytically estimate more physical lower boundary condition values at  $R_{\min}$ .

We select the lower boundary condition such that the majority of the flux is captured in the wind. For computational efficiency, we choose this to be the 1-microbar radius, but the pressure is customizable. The  $\tau(\nu) = 1$  surface for the highest energy photons ( $\gtrsim 1$  keV) is below 1 microbar; however, we find that the contributions of these highest energy photons to the mass loss rates in typical systems to be negligible. If concerned with modeling more precise ionization fractions of a species as a function of radius one may set the base of the simulation to a higher pressure.

This isothermal, molecular region below the photoionization region is in radiative equilibrium. The balance between thermal emission and incident stellar bolometric radiation sets the skin temperature,  $T_{\text{skin}}$ , in the region below the wind and above the  $\tau_{\text{IR}} = 1$  surface. Above nanobar pressures, the molecules are photodissociated and become atomic in the wind for most planets (though super-Earths may be the exception (see Frelikh et al., submitted)). Within the wind, photoionization heating, Lyman- $\alpha$  cooling, and  $PdV$  cooling dominate, setting the temperature of the wind throughout the flow.

The addition of bolometric heating and cooling to this investigation allows the relaxation code to physically solve for where the photoionization heating begins to dominate and the wind launches. Since the  $\tau(\nu) = 1$  surfaces will be different for photons of different frequencies,  $\nu$ , and will depend on the metallicity and metals present (via the ionization cross section,  $\sigma_s(\nu)$ ), estimating the radius of the wind base is non-trivial. Additionally, the mass loss rate and wind structure are sensitive to the pressure where the wind is launched, because deeper penetration tends to lead to cooler, slower winds with lower mass loss rates (see Fig. 4).

To set the  $T_{\text{skin}}$  isotherm below the wind, the bolometric flux,  $F_* = \frac{L_*}{4\pi a^2}$  is computed from the bolometric luminosity,  $L_*$ , and semi-major axis,  $a$ . Then, the skin temperature, becomes

$$T_{\text{skin}} = \left[ \frac{F_*(\kappa_{\text{opt}} + \kappa_{\text{IR}}/4)}{2\sigma_{SB}\kappa_{\text{IR}}} \right]^{1/4}. \quad (\text{B1})$$

The exact prefactors in this equation are dependent on geometry and various Eddington coefficients, but the impact of their exact choice is small, thanks to the quartic root. In Equation B1,  $\kappa_{\text{opt}}=0.004$  and  $\kappa_{\text{IR}}=0.01$  are the defaults for optical and infrared opacity, respectively. These values are no longer valid in the atomic, optically-thin wind, so we multiply by an error function to drop  $\kappa_{\text{opt}}$  and  $\kappa_{\text{IR}}$  to zero in the wind. Between the base of the wind and the  $\tau_{\text{IR}} = 1$  radius the atmosphere is an isotherm at the skin temperature. Equation B1 is obtained by setting the optically thin bolometric heating,  $\Gamma_{\text{bolo}}$  (taken as the sum of direct and indirect bolometric heating), and bolometric cooling,  $\Lambda_{\text{bolo}}$ , equal

$$\Gamma_{\text{bolo}} = F_{in,\text{opt}}\kappa_{\text{opt}}\rho(r) + F_{in,\text{IR}}\kappa_{\text{IR}}\rho(r) \quad (\text{B2})$$

$$= F_*\rho(r) \left( \kappa_{\text{opt}} + \frac{1}{4}\kappa_{\text{IR}} \right) \quad (\text{B3})$$

$$\Lambda_{\text{bolo}} = 2\sigma_{SB}T_{\text{skin}}^4\rho(r)\kappa_{\text{IR}}. \quad (\text{B4})$$

where  $F_{in,\text{opt}} = F_*$  captures the direct bolometric heating from the star and  $F_{in,\text{IR}} = \sigma_{SB}T_{eq}^{1/4} = \frac{1}{4}F_*$  is via the gray slab approximation for re-emission of IR radiation. Then, using the fact that  $R_P$  for most planets given is the *slant path* optical surface, we can solve geometrically using  $\tau_{\text{slant,opt}} = \kappa_{\text{opt}}l\rho(R_P) = 1$  where  $l$  is the slant path length of stellar optical photons through the transiting planet's atmosphere. To first order,  $l = \sqrt{8H_{sc}R_P}$ , where the scale height  $H_{sc}$  is computed using the skin temperature and mean *molecular* weight (as opposed to atomic, as is usually the case in the wind). The default adjustment for the mean molecular weight is a factor of 2.3 to account for molecular hydrogen, but users have the ability to customize this value and are recommended to do so for more metal rich atmospheres.

Density at  $R_P$  is then

$$\rho(R_P) = \sqrt{\frac{\mu_{\text{mol}}GM_P}{8R_P^3k_B T_{\text{skin}}}}. \quad (\text{B5})$$

For most planets, the pressure at  $R_P$  is of order 10 millibars. However, to ease the computational burden, we place the bottom of the simulation either at 1 microbar or, if the  $\tau_{\text{IR}} = 1$  surface to vertically-incident photons,  $R_{\text{IR}}$  is above  $R_P$  we take the base of the simulation to be  $R_{\text{IR}}$ . Most XUV rays are absorbed between micro- and nanobar pressures, with winds launching approximately around the 10 nanobar radius. At higher pressures than microbar pressures, the balance of bolometric heating and cooling enforces an isotherm at the skin temperature.

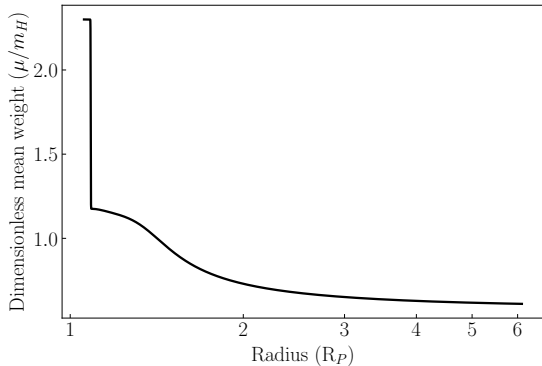


**Figure 19. Mean Weight Complimentary Error Function Transition** - The transition from mean molecular weight  $\mu(r < R_{\text{XUV}}) = 2.3m_H$  to mean atomic weight as governed by Equation 6 for HD 209458b. Here the erfc decays over 1 scale height at  $R_{\text{XUV}}$ .

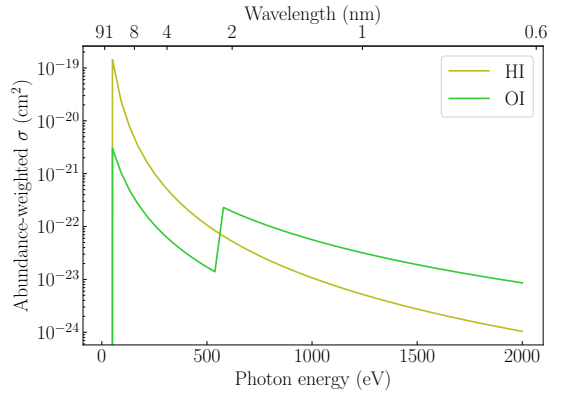


**Figure 20. Abundance-weighted Ionization Cross-Sections** - Photoionization cross-sections for HI (olive) and OI (lime green) weighted by their fractional abundance (0.79332 and 0.00669, respectively) at  $1 \times$  solar metallicity as a function of photon energy (bottom axis) and wavelength (top axis). Frequency-dependent cross sections are derived from coefficients and analytic equations in Verner & Ferland (1996); Band et al. (1990).

Because the  $\kappa_{\text{opt}}$  and  $\kappa_{\text{IR}}$  should drop off as the molecules are thermally- and photodissociated and the mean molecular weight should transition to the atomic, we need a way to enforce this transition occurring before the wind launches at  $R_{\text{XUV}}$ . To do so, we use a complementary error function, because it allows us to modify the rate and location of the drop off as appropriate for a given profile:

$$\text{erfc}[r] = \text{erfc} \left[ \frac{v(r) - v_{R_{\text{XUV}}}}{xH_{sc,0} \frac{\Delta v}{\Delta r}|_{R_{\text{XUV}}}} \right], \quad (\text{B6})$$

where  $v$  is the local comoving velocity as a function of  $r$ ,  $v_{R_{\text{XUV}}}$  is the velocity at  $R_{\text{XUV}}$ , and  $\Delta v/\Delta r$  is the slope of the velocity in the vicinity of  $R_{\text{XUV}}$ . Then,  $xH_{sc,0} = x \frac{k_B T(R_{\text{XUV}}) R_{\text{XUV}}^2}{\mu_{\text{mol}} G M_P}$  is some multiple  $x$  of the scale height at  $R_{\text{XUV}}$ , where  $R_{\text{XUV}}$  is computed as the radius at which photoionization heating begins to dominate over  $PdV$  cooling. This creates an error function that drops from 1 to 0 over  $x$  scale heights at  $R_{\text{XUV}}$ . The default value of  $x$  is 1. The altitude in the atmosphere at which these high energy photons are absorbed (where  $\tau(\nu) = 1$ ) depends on the frequency  $\nu$  of the incident photon. We compute  $R_{\text{XUV}}$  and radial extent of the complementary error function postfacto as part of the process of polishing the relaxation solution to self consistency. As such,  $R_{\text{XUV}}$  is not affected by our choices for Equation B6.

To compute the simulation lower boundary radius,  $R_{\min}$ , and density,  $\rho(r = R_{\min})$ , we use the hydrostatic equilibrium equation and the assumption of isothermality of the region between  $R_{\text{IR}}$  and the wind base to derive

$$R_{\min}(P_{R_{\min}}) = \left[ \frac{c_s^2}{G M_P} \ln \left( \frac{P_{R_{\min}}}{P(R_P)} \right) + \frac{1}{R_P} \right]^{-1} \quad (\text{B7})$$

$$\rho(R_{\min}) = P_{R_{\min}} \frac{\mu_{\text{mol}}}{k_B T_{\text{skin}}}, \quad (\text{B8})$$

where  $P(R_P)$  is the pressure at  $R_P$  and  $P_{R_{\min}}$  is the pressure at the base of the simulation, both in barye ( $10^{-6}$  bars). This value should always be between 1 microbar and 1 millibar to capture the contributions from the highest energy photons and to stay in the isothermal portion of the atmosphere.

By default, we take  $P_{R_{\min}} = 10^{-6}$  bar = 1  $\mu$ bar. Ideally, though, for our assumption of isothermality we should take  $R_{\min}$  to be the  $\tau_{\text{IR}} = 1$  radius to vertically-incident IR photons,  $R_{\text{IR}}$ . However,  $R_{\text{IR}}$  is typically below  $R_P$ , the optical slant path radius of the planet in transit. As such, Wind-AE has a rarely activated condition that, should  $R_{\text{IR}} > R_P$ ,  $R_{\min} = R_{\text{IR}}$  and we can similarly solve from hydrostatic equilibrium to obtain

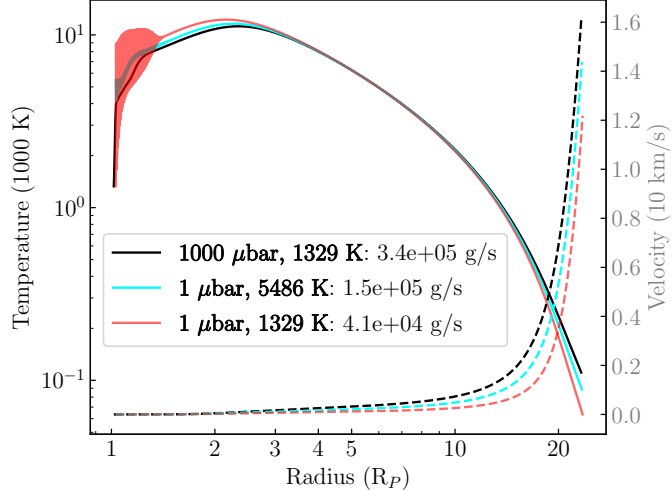


**Figure 21. Smoothing high-escape-velocity planet lower BC temperature oscillations** -  $55 M_{\oplus}$ ,  $1.85 R_{\oplus}$  at 0.05 au with  $F_{\text{tot}}=1095 \text{ ergs s}^{-1} \text{ cm}^{-2}$  temperature (right y axis, solid) and velocity profiles (left y axis, dashed). For a lower boundary pressure of 1 microbar,  $R_{\min} = 1.028 R_P$  which does not capture the bolometrically heated/cooled region, so  $T(R_{\min}(1\mu\text{bar})) \neq T_{\text{skin}} = 1324 \text{ K}$  (red) and results in an order of magnitude higher mass loss than the ground truth (black). Averaging the temperature oscillations tells us the  $T(R_{\min}(1\mu\text{bar})) = 5486 \text{ K}$  (cyan) which puts the mass loss rate within a factor of 2. Because neither of these solutions capture the molecular region, there is no higher mean molecular weight or bolometric heating/cooling included. To confirm the validity of this approximation, we lower (black) the base pressure to 1000 microbar ( $R_{\min} = 1.016 R_P$ ) to capture the photoionization base and molecular region, thus making  $T(R_{\min}(1000\mu\text{bar})) = T_{\text{skin}} = 1324 \text{ K}$ .

$$R_{\text{IR}} = \frac{R_P^2}{H_{sc} \ln \left( \frac{\rho(R_{\text{IR}})}{\rho(R_P)} e^{R_P/H_{sc}} \right)}, \quad (\text{B9})$$

where we approximate the scale height at  $R_{\text{IR}}$  to be the scale height at  $R_P$  and  $\rho(r = R_{\text{IR}})$  follows from  $\tau_{\text{IR}} = \rho(R_{\text{IR}}) \kappa_{\text{IR}} H_{sc} = 1$ .

In cases such as those discussed in §5.1 high escape velocity and low flux cases, where setting the base at  $R_{\min}(1\mu\text{bar})$  does not capture  $R_{\text{XUV}}$ , the photoionization base / wind launch radius, our model turns off the bolometric heating/cooling and other molecular layer assumptions, because that layer is not captured at  $R_{\min}(1\mu\text{bar})$ . Indeed, the assumptions we make to derive our lower boundary conditions are no longer valid and holding  $T(R_{\min}) = T_{\text{skin}}$  results in numerical temperature oscillations with radius. Instead, because  $R_{\min}$  does not capture the true base of the wind,  $T(R_{\min})$  should be several thousand degrees kelvin higher than  $T_{\text{skin}}$ . Taking the average of these numerical temperature oscillations near the simulation base gives us a decent estimate of the what the  $T(R_{\min})$  should be for this  $R_{\min}$  located in the middle of the wind.

We confirm that this approximation is adequate by lowering the simulation base to, e.g.,  $R_{\min}(100\mu\text{bar})$ , so that we accurately capture the molecular region and  $R_{\text{XUV}}$  and compare our oscillation-averaged temperature at  $1\mu\text{bar}$  in the shallow solution to the actual temperature at  $R(1\mu\text{bar})$  in the deeper solution (Fig. 21). The density should also slightly change in this case, but we find that the effects of changing  $\rho(R_{\min})$  to a more physically accurate value are secondary. In the highest escape velocity limits, setting  $R_{\min}(1\mu\text{bar})$  and using the above method to find  $T(R_{\min})$  is no longer sufficient as the planets' scale heights are so small that the region below  $R_{\min}(1\mu\text{bar})$  is dense enough to absorb higher energy X-rays that contribute to heating and ionizing, thus we may be underestimating temperature and ionization fraction at  $R_{\min}(1\mu\text{bar})$ , as well as the total mass loss rate.

In low-escape-velocity limit the inclusion of bolometric heating and cooling and the higher mean molecular weight result in the behavior we entitle “bolometric puffing” (§5.2). Bolometric puffing increases the density and thereby optical depth of the atmosphere at higher altitudes and results in a higher altitude  $R_{\text{XUV}}$ . The result is a wind that launches higher in the potential well than predicted by models that do not treat the region below the wind (e.g., Fig. 18).

2105

C. ESCAPE OF LYMAN- $\alpha$  PHOTONS

2106 The planetary winds modeled here are optically thick to Lyman- $\alpha$  radiation since, at line center, the cross-section  
 2107 for Lyman- $\alpha$  absorption by a neutral hydrogen atom is larger than the cross-section for photoionization. Nevertheless,  
 2108 as illustrated in Murray-Clay et al. (2009, their Appendix C), the wind is low enough density that the majority of  
 2109 Lyman- $\alpha$  photons emitted in the wind ultimately scatter into the line wings and escape before their energy can be  
 2110 returned to the thermal bath. A Lyman- $\alpha$  photon's energy is thermalized if it excites an atom and the atom then  
 2111 experiences a collision, resulting in collisional de-excitation, before the atom has the chance to spontaneously de-excite  
 2112 and re-emit another Lyman- $\alpha$  photon.

2113 To validate the order-of-magnitude calculation in Murray-Clay et al. (2009), we run a Monte-Carlo calculation of  
 2114 Lyman- $\alpha$  photon escape. We use the hot Jupiter profile for a H-He HD 209458b provided in Figure 8 and assume  
 2115 spherical symmetry. We run 1000 photons, each beginning at radius  $r = 1.18R_p$ , where the Lyman- $\alpha$  cooling rate  
 2116 peaks for this outflow. At each step in the calculation, we draw a Lyman- $\alpha$  frequency,  $\nu$ , from a Voigt profile at the  
 2117 local temperature and density and draw a random direction. We use the integrated optical depth along that direction,

$$2118 \quad \int n_{0,H}(r) \sigma_{\text{abs}}(\nu, r) dl \quad (\text{C10})$$

2119 to draw a random distance at which the photon is absorbed. The number density of neutral hydrogen,  $n_{0,H}$ , and the  
 2120 cross-section for absorption at frequency  $\nu$ ,  $\sigma_{\text{abs}}(\nu)$ —which depends through the Voigt profile on temperature and  
 2121 density—are both functions of the radial coordinate  $r$ . We note that given the chosen direction, the variation of  $r$   
 2122 along the path is determined by geometry.

2123 Once the photon is absorbed we calculate, using gas conditions at its new radial distance, the timescale,  $t_{\text{col}}$  on  
 2124 which it is expected to be de-excited by collision with an electron (cross-section  $2 \times 10^{-15} \text{ cm}^2$ ; Brackmann et al.  
 2125 1958), a proton (cross-section  $2 \times 10^{-14} \text{ cm}^2$  including charge-exchange; Hunter & Kuriyan 1977) or other species. For  
 2126 other species, we use the electron cross-section which is a reasonable approximation for typical collisions with a neutral  
 2127 hydrogen atom. More detailed treatment of individual species is not merited because electron collisions dominate.  
 2128 Given a spontaneous decay rate of  $A_{21} = 6.265 \times 10^8 \text{ s}^{-1}$  for hydrogen Lyman- $\alpha$ , the probability that the photon is  
 2129 thermalized before re-emission is  $1 - e^{-1/(A_{21}t_{\text{col}})} \approx (A_{21}t_{\text{col}})^{-1}$ . We draw a random number to determine whether  
 2130 the photon is thermalized at this step. Because our example wind profile transitions to the bolometrically-heating  
 2131 regime below  $1.1R_p$  and we do not trust detailed model conditions below this radius, we automatically thermalize any  
 2132 photon that reaches a radius smaller than  $1.1R_p$ . This choice is conservative, as the energy from these photons may  
 2133 be radiated away by bolometric or molecular radiation at depth rather than heating the gas. We consider a photon to  
 2134 have escaped the wind if it reaches a radius of  $10R_p$ .

2135 We find that 73% of our modeled photons escaped the wind, demonstrating that a majority of the photons indeed  
 2136 escape. We re-ran the calculation starting photons at  $1.11R_p$ , near the base of the wind simulation where Lyman- $\alpha$   
 2137 excitation via secondary electrons is most important. Though this starting point is very near to our auto-thermalization  
 2138 distance, 51% of the 1000 modeled photons escaped.

2139 In examples with higher incident flux, Lyman- $\alpha$  cooling is typically more important. We therefore repeated this  
 2140 calculation for a planet with the same mass and radius but an incident flux 100 times larger. We found that photons  
 2141 emitted from the peak of the Lyman-alpha cooling region escaped 67% of the time. For this example, no bolometric  
 2142 heating region is modeled, and photons started just above the lower boundary of the simulation escaped 40% of the  
 2143 time.

2144 In both cases, a majority of the Lyman- $\alpha$  cooling radiation indeed escapes from the outflow. For secondary electron  
 2145 energy that goes into Lyman- $\alpha$  excitation, the ultimate escape fraction depends on the true fate of photon energy that  
 2146 diffuses below the base of our simulation. As discussed in Section 2.4.3, our choice to treat this energy as escaping  
 2147 does not make a substantial difference to our results.

## 2148 D. MULTISPECIES &amp; MULTI-FREQUENCY VERSIONS OF FINITE DIFFERENCE EQUATIONS

2149 To solve for Equations 1 - 5, we update equations (9)-(13) of Murray-Clay et al. (2009) to include our multispecies  
 2150 and multi-frequency assumptions.

$$2151 \quad E_{1,j} \equiv \Delta_j \rho - \frac{d\rho}{dr} \Delta_j r$$

$$2152 \quad = \Delta_j \rho + \rho \left( \frac{2}{r} + \frac{1}{v} \frac{dv}{dr} \right) \Delta_j r = 0 \quad (D11)$$

$$2153 \quad E_{2,j} \equiv \Delta_j v - \frac{dv}{dr} \Delta_j r \\ 2154 \quad = \Delta_j v - \frac{v}{v^2 - \gamma \lambda k T / \mu} \left[ \frac{2\gamma \lambda k T}{\mu r} - \frac{(\gamma - 1)Q}{\rho v} - \frac{GM_P}{r^2} + \frac{GM_*}{(a - r)^2} + \frac{1}{2} \frac{GM_*(a - r(1 + M_P/M_*))}{a^3} \right] \Delta_j r = 0 \quad (D12)$$

$$2155 \quad E_{3,j} \equiv \Delta_j T - \frac{dT}{dr} \Delta_j r \\ 2156 \quad = \Delta_j T - \left[ (\gamma - 1) \left( \frac{Q}{\rho v} \frac{\mu}{k} + \frac{T}{\rho} \frac{d\rho}{dr} \right) + \frac{T}{\mu} \frac{d\mu}{dr} \right] = 0 \quad (D13)$$

$$2157 \quad E_{4+s,j} \equiv \Delta_j \Psi_s + \frac{d\Psi_s}{dr} \Delta_j r \\ 2158 \quad = \Delta_j \Psi_s - \frac{m_s}{Z_s \rho v} (\mathcal{R}_s - \mathcal{I}_s) \Delta_j r = 0 \quad (D14)$$

$$2159 \quad E_{(4+N_{sp})+s,j} \equiv \Delta_j N_{\text{col}} - \frac{dN_{\text{col}}}{dr} \Delta_j r \\ 2160 \quad = \Delta_j N_{\text{col}} + \Psi_s \frac{Z_s \rho}{m_s} \Delta_j r = 0 \quad (D15)$$

2161 where  $j$  is the point along the radial grid,  $Q = \Gamma + \Lambda$ , and  $Z_s$  is the mass fraction of species  $s$ . We write  $N_{sp}$  as  
2162 short-hand for  $N_{\text{species}}$  the number of species,  $s$ , in the wind, where  $s$  ranges from  $[0, N_{\text{species}} - 1]$ . Therefore, the  
2163 number of equations in the system of equations becomes  $3 + 2N_{\text{species}}$ , hence the computational expense of modeling  
2164 more metals.

2165 The final equation is given in terms of  $N_{\text{col},s}$ , rather than  $\tau$  as in Murray-Clay et al. (2009), because  $\tau_\nu = \sum_s \sigma_{\nu,s} N_{\text{col},s}$   
2166 and individual species may ionize at different rates as a function of radius, so we must track the column density of  
2167 each species individually in order to calculate  $\tau$ .

2168 The most important changes are summarized here. For a more detailed discussion of numerical and analytic changes,  
2169 see McCann (2021).

## 2170 E. SPECTRUM

2171 We avoid the cost of running a high resolution spectrum by fitting a polynomial to the input stellar spectrum. Any  
2172 observed spectrum—such as the FISM2 solar spectrum from the LISIRD database we use for this paper—or realistic  
2173 simulated XUV spectrum will vary widely in flux and shape across the spectral range, as well as be high resolution,  
2174 making fitting polynomials difficult. If the the spectral qualities can be well approximated by low degree polynomial(s),  
2175 though, it is inexpensive to accurate perform numerical integrations using Gauss-Legendre quadrature. Thus, we use  
2176 the smoothing and binning algorithm (discussed in more detail in McCann 2021, §2.3.5).

2177 Logarithmic fits and/or the least squares method would not locally (or, potentially, even globally) conserve energy  
2178 along the spectrum, thus we employ a Savitzky-Golay filter, which smooths evenly-spaced noisy data with a rolling  
2179 polynomial. First we smooth the peaks the troughs of the spectrum by multi-passing the spectrum through the  
2180 Savitzky-Golay filter. The effect of running a Savitzky-Golay filter on small segment is similar to running a single pass  
2181 filter on a larger wavelength range, but it distorts the data less than a standard, larger single pass filter and better  
2182 preserves the area under the smoothed spectrum. The filtered spectrum is then renormalized to conserve total energy  
2183 in each bin. Next a 5th degree polynomial is fit to the filtered spectrum, again rescaling to preserve energy in each  
2184 bin. The polynomial is calculated by used a spline with with an infinite smoothing factor, which relaxes the spline to  
2185 a single bin interval.

2186 Binning the spectrum allows us to run the multipass filtering in fewer smoothing passes and allows us to more  
2187 accurately preserve the spectrum shape, especially at the ionization wavelengths of species present in the model.  
2188 Subbinning, in particular, allows us to fit the spectrum with more low order polynomials, as opposed to fewer poly-  
2189 nomials that would have to be higher order and would be more difficulty to accurately and cheaply integrate using  
2190 Gauss-Legendre quadrature. For our bins, we choose bin width  $2r$  centered at wavelength  $\lambda_0$  such that the error over  
2191  $\lambda \in [\lambda_0 - r, \lambda_0 + r]$  is less than  $\epsilon$ . Using the analytic Verner & Ferland (1996) cross section relations, we can take the  
2192 logarithmic derivatives of the Verner cross sections,  $\sigma_{\lambda,s}$  for species  $s$  and use the chain rule to derive the bin halfwidth,

2193

$$r \leq \left( \frac{6\epsilon}{\|\sigma_{\lambda,s}^{(3)}\|_\infty} \right)^{1/3}. \quad (\text{E16})$$

2194 Bin edges are also placed at the ionization energies and K-shell ionization energies of the species present, unless one  
 2195 of the ionization energies of an existing species is within 2 nm of an existing species' ionization energy.

2196 The physical effects of smoothing a spectrum are also mitigated by using the above method. Ionizing energy is  
 2197 conserved since the peaks of the spectrum are smoothed and distributed locally—meaning there will be an equal  
 2198 amount of higher and lower than the peak ionization energy photons in the wind. That being said, at the edges  
 2199 of the spectrum, where there are not necessarily symmetric peaks over which to smooth, this method may over or  
 2200 underestimate the number of higher or lower energy photons. However, we take this smoothed approximation for a  
 2201 high resolution spectrum to be sufficient for our work.

2202

## F. METAL LINE-COOLING

2203 The metal line cooling rates for CII, CIII, OII, and OIII are computed via the emmisivity equation (Eq. 9). Where  
 2204  $A'$  in that equation is the correctly scaled version of  $A$  such that  $\Lambda$  is the cooling rate per unit volume. CLOUDY (Ferland  
 2205 et al. 2017) is then used to compute the coefficients  $A$ ,  $T_{line}$  (line transition temperature), and  $n_c$  (critical number  
 2206 density).

2207 We use CHIANTI (Dere et al. 1997; Del Zanna et al. 2015) to identify all the relevant lines and extract the values  
 2208 which are listed below. These fits are typically good to 10-20% and at worst a factor of two in extreme regions of the  
 2209 parameter space.

Line	$A'$	$T_{line}$	$n_c$
157μm	1.783E-20	91.2	1.388E+01
2326Å	1.215E-10	61853.9	1.210e+09
1334Å	2.413E-03	107718.1	3.740E+15

**Table 1.** Properties for the cooling functions of CII - all values in cgs units.

Line	$A'$	$T_{line}$	$n_c$
1910Å	3.84E-10	75460.8	1.314E+9
977Å	1.791E-03	147263.9	7.172E+14

**Table 2.** Properties for the cooling functions of CIII - all values in cgs units.

Line	$A'$	$T_{line}$	$n_c$
834Å	5.786E-4	172421.6	1.322E15
2741Å	3.812E-13	58225.3	4.488E7
3727Å	4.299E-16	38575.0	5.365E3
7320Å	3.769E-13	53063.6	3.110E7

**Table 3.** Properties for the cooling functions of OII - all values in cgs units.

Line	$A'$	$T_{line}$	$n_c$
52μm	3.138E-18	277.682	2.549E3
5000Å	3.387E-14	28728.6	9.667E5
166Å	6.560E-10	86632.4	1.476E10
83.5Å	1.752E3	172569.7	5.406E21

**Table 4.** Properties for the cooling functions of OIII - all values in cgs units.